CFD modelling of an airfoil section equipped with Vortex generators

Master of Science Thesis

For obtaining the degree of Master of Science in Engineering Wind Energy at
Technical University of Denmark and in Aerospace Engineering at
Delft University of Technology

Thawatchai Wanthanadamkerng

31 July 2017

Wind Energy Research Group, Faculty of Aerospace Engineering,
Delft University of Technology

Dr.ir. A.H. van Zuijlen/ Professor N. S. Sørensen/ Dr. N. Troldborg/ L. Broersma

Abstract

The use of vortex generators (VGs) is a prevailing technology in large modern wind turbines due to its potential to increase wind turbine annual energy production [39] by re-energizing the momentum energy in the boundary layer and, as a consequence, delay the flow separation. Many researchers have been extensively studying the effects of VGs on airfoil sections but none have included the VGs' baseplate into their studies. This research aims to fill this gap and hopes to contribute toward the current body of work in VG research by studying the effect of the baseplate on the airfoil aerodynamics.

The main goal of this thesis is to identify the effect of the baseplate of the vortex generators. The effect of VG positions, VGs with baseplate, Reynolds number, baseplate height and roughness model were studied in order to achieve the goal. Five baseplate shapes were studied in this research in order to cover all possible geometries in the real applications.

Airfoil section with VGs were shown to be effective in delaying flow separation for both FFA W3-301 and DU 91 W2-250 airfoils. From the results of the simulations of airfoil sections with baseplate and VGs, baseplate shape no.2 (sharp bevel) shows an early flow separation and has the worst performance. The baseplate shape no.5 (”S” shaped bevel) shows results that were close to the airfoil without baseplate.

In studying the airfoils with roughness, it was seen that by adding VGs, the loss in lift was restored. A reference wind turbine model was used in order to compute the wind turbine's annual energy production. The rough airfoil had an annual energy production approximately 18% less than the clean airfoil for FFA W3-301 and approximately 13% for DU 91-W2-250. By adding VGs to the rough airfoil section, the AEP increased by around 10% for FFA W3-301 airfoil with VGs at 0.20c and approximately 5% for DU 91-W2-250 airfoil with VGs at 0.20c. Taking the baseplate (except baseplate shape no.2) into consideration, both the maximum lift and aerodynamic efficiency saw slight improvements in both airfoils. This could be a consequence of the baseplate which allowed the flow to pass resulting in accelerating flow being able to be energized by the VGs.

From the studies, the baseplate shape no.2 (sharp bevel) had performed poorly in simulations with both airfoils, although the flow separation was seen to be delayed at high Reynolds numbers. However, due to the simplicity in manufacturing, this shape may still be used in practice and as such, it is highly recommended that the baseplate configuration is taken into accounted during the design process. This research has shown that it is advantageous to have baseplates with a smooth bevel likes baseplate shape no.1 (beveled edge) and 5 (”S” shaped bevel) in order to avoid unexpected flow separation. The effect of the baseplate could also be more important to account for in simulations as the height of the baseplate might increase in the future, if a larger VG is needed.

Acknowledgements

I would like to express my gratitude to my supervisors Niels N. Sørensen and Niels Troldborg from DTU, Alexander van Zuijlen from TU-Delft, Liekele Broersma and Robert Kommer from SUZLON for the useful comments, remarks and engagement throughout the learning process of this master thesis. I would like to extend my sincerest thanks to Niels N. Sørensen and Niels Troldborg for helping me set-up this research. Furthermore I would like to thank Garry Kwan and Ang Li for giving me advice and help during the research. Finally, I would like to thank my late grandmother, who had supported me ever since I was born. You are in my thoughts forever.

Thawatchai Wanthanadamkerng
RISØ DTU, Denmark
2017, July 30th

Nomenclature

Acronyms

AEP	Annual Energy Production
BAY	Bender, Anderson and Jagle Vortex Generator Modeling
BP	Baseplate
CDS	Central Differencing Scheme
CFD	Computational Fluid Dynamics
exp	Experimental Result
$QUICK$	Quadratic Upstream Interpolation for Convective Kinematics
SST	Shear-Stress Transport
$SUDS$	Second-order Upwind Differencing Scheme
UDS	Upwind Differencing Scheme
$VG(s)$	Vortex Geenerator(s)

Symbol

β	VG's Angle of Attack	[degree]
C_f	Friction Coefficient	[-]
C_P	Power Coefficient	[-]
C_{VG}	Vortex Generator Calibration Coefficient	[-]
d_1	Distance between Individual VG	[-]
d_2	Distance between Each VG Pair	[-]
d_3	Distance between VG's Leading-edge to the Bevel	[-]
d_4	Baseplate's Length	[-]
h	VG's Height	[-]
l	VG's Length	[-]
L_{VG}	VGs' Location	[-]
t	Baseplate's Thickness	[-]

Contents

List of Figures

List of Tables

CHAPTER 1 Introduction

1.1 Background

One of the most challenging issues in the world today is sufficient energy resources. Most developed countries pursue affordable, reliable and clean energy. This is because other forms of energy such as coal, oil and natural gas have shown that they do more harm than good. Besides, during the extraction and transformation processes, they generate water pollution and air emissions, especially CO_2 which contributes to the global warming and as a consequence gives rise to climate change. Nuclear is yet another form of energy, but it is not without its issues. Some examples are uncertainty in terms of national security and also health issues arising from waste management. Radioactive byproducts from generating electricity at a nuclear plant need special waste management which is costly.

The issues that arise from the aforementioned forms of energy show why renewable energy is a better choice. Aside from the fact that renewable energy is cleaner and does not generate any waste or byproduct from the electricity production which could lead to a much lower adverse environmental impact, it must also be economically competitive.

Wind is one such renewable energy resource. Electricity can be generated by wind turbines given that there is the presence of wind. Recently, the European Union (EU) has set a legally binding target by 2030 of at least 27% renewable energy [13]. For wind energy, the amount of energy that will be installed by 2030 is 320 GW, which consists of 254 GW onshore and 66 GW offshore wind turbines. These figures reveal the marginal growth in the demand for wind turbines which is more than twice compared to 117.9 GW of wind power that was installed in 2014 [12]. In order to meet the target set by the EU, there is a demand to increase the number of wind turbines. To be economically competitive, the power production capability of wind turbines must be improved. Recently DONG ENERGY has successfully installed the world's largest wind turbine Vestas V164 [49], which is a three blades wind turbine with a capability to produce electricity up to 8 MW.

Although larger wind turbines can generate more power, it also carries more loads. To cope with these issues, blade root section needs to be thicker and large enough to withstand the loads. Therefore, the thicker airfoil is preferable for the blade root section. However, thick airfoils are prone to flow separation. This consequently leads to a loss in blade performance as well as power production. In order to restore losing lift, a device for flow separation control is needed. Before, a method to control the flow separation is introduced, the flow separation mechanism is detailed in the next section.

1.2 Flow Separation

Understanding the physics of flow separation is essential, as it would give a clear picture of what it is and why it needs to be controlled. Leading edge and trailing edge separation are examples of flow separation over an airfoil. Several explanations of the flow separation were detailed in the works of Maskell [25], Lighthill [21] and Schlichting [31].

Considering a flow passing over a surface or airfoil as seen in figure 1.1, there are mainly two flow regions: laminar and turbulent. The flow is rather uniform and the boundary layer thickness is small in the laminar region. The point, where the laminar flow becomes turbulent is called the transition location. Airfoil's transition location varies and depends on the shape of the airfoil and Reynolds number. Once the flow is turbulent the boundary layer is growing toward the trailing edge of the airfoil and eventually separates from the airfoil surface. The flow separation mechanism is illustrated in figure 1.1.

From figure 1.1, the boundary layer is thickening toward the trailing edge of the airfoil as the flow is expanded. At some point the flow cannot remain attached to the wall, the velocity gradient as well

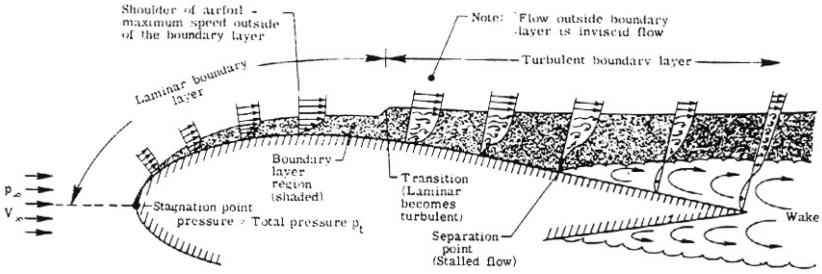

Figure 1.1: Real flow over the top surface of an airfoil [28]

as the wall shear stress (τ_w) at that point vanishes [31], which can be shown in the following equation:

$$\tau_w = \mu(du/dy)_w = 0 \tag{1.1}$$

where μ is the dynamic viscosity of the fluid and has the unit of $[N \cdot s/m^2]$. Behind the separation point, some of the flow will reverse as the result of negative velocity gradient as depicted in figure 1.2. The negative velocity gradient is caused by an increase in pressure after the flow reaches the minimum pressure. This effect is severe for a thick airfoil, which has high adverse pressure gradient due to the curvature of the airfoil.

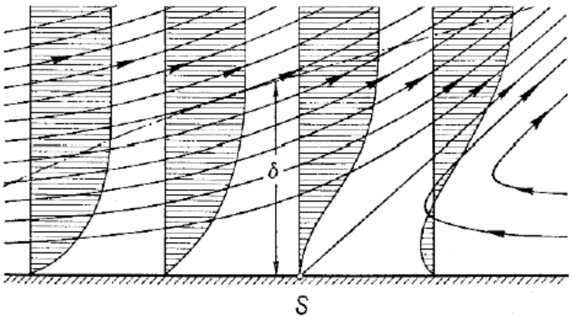

Figure 1.2: Flow separation over a surface [31]

1.3 Flow Separation Control

As mentioned, flow separation results in a loss in lift. Therefore, it would be beneficial, if some technique can be employed to delay flow separation. Various approaches to control flow separation have been reviewed by Ashill [2], John [22], and Gad-el-Hak [14]. Early development of flow separation techniques emphasized aircraft applications. One of the techniques that was used to control flow separation over the wing is to manipulate the airfoil's camber or leading edge radius by using a pneumatic mechanism [2]. The devices do not obstructing the flow until they are used, hence they do not contribute to the parasitic drag. Such a technique is categorized as active control, as its system consist of a flow measurement device and an actuator. The actuator is heavy and add additional airfoil mass. Another successful application was to use an embedded injection in a multistage compressor [7]. The device had proven to lessen flow separation on vanes. Although, the method showed numerous successes, it requires mechanisms which could be heavy and not suitable for wind turbine application.

Passive flow separation control is a device, that is pre-installed or attached on the airfoil before operation. One of the passive flow separation control devices is the vortex generator (VG), which is popular in the modern aerospace and wind turbine industry. The device was first introduced by Taylor [40]. The vortex generators comprise of a row of thin flat or airfoil shaped plates facing toward an incoming flow at an angle of attack. VGs will create longitudinal vortices and more turbulence that mixes high momentum air from the outer flow down into the boundary layer near the surface, making the flow more resistance to separation in an adverse pressure gradient [15].

Early VGs are used in aerospace applications for the purpose of flow-separation control. In a review of flow control using VGs [22], it was stated that VGs have been used for improving airfoil/wing performance, decreasing aircraft interior noise during the transonic cruise and also reducing flow distortion within compact ducts. They have also been applied in the aircraft engine sections such as turbine ducts, diffuser, and intakes [2]. One of the success application of VGs was on the Voyage canard. VGs had shown an improve in the aircraft longitudinal quantities (pitch motion control) during a harsh environment [5].

VGs have also been used extensively for wind turbine applications in order to control the flow separation at the blade root region. An example of a wind turbine benefits from VGs is a MOD-2 wind turbine which has shown a rising in the annual energy production by 11 percent [39]. VGs also proved to prevent roughness-induced separation on a thick airfoil [42].This has shown that VGs are an effective flow separation controller and could enhance wind turbine performances. Besides, with a given amount of load on the wind turbine rotor blade, using VGs could also achieve the same load with smaller chord or slender blade [15]. There are also many study cases where VGs are mounted on the rotor blade and have shown an improvement in annual energy production (AEP). A study on Suzlon S88 turbines has been done by Upwind Solutions, showed that the turbines with VGs have an increase of 2.5% in AEP [46].

Therefore, it is very important to integrate VGs into the blade design process. Conventionally, effect of VGs on the wind turbine can be obtained from the wind tunnel experiment. However, the experiments are costly and might be time consuming. Hence, with modern computers, Navier-Strokes code CFD simulation is preferred.

1.4 Research Questions

The effect of VGs on an airfoil's performance has been studied [36] using a fully-resolved VG model. The results show that the VGs can effectively delay stall and adverse pressure gradient on an airfoil. Two airfoils, a thick (FFA-W3-360) and a thin (FFA-W3-301) are investigated. In the thin airfoil case, there is an agreement for both experimental and computational results for the lift curve in the linear region up to where separation starts. However, the computational results predicted a lower drag than the experimental results. Although subtracting the experimental results by one-third of the drag, which is a hypothetical contribution by the VGs base plates, the computational results still under-predict. In the same reference, an effect of the VGs on the thick airfoil (FFA-W3-360) was also studied. For the VG at x/c=0.15, the lift curves of the numerical and experimental results are not well matched. This issue was assumed causing by the absence of the baseplate in the simulation [36]. This hypothesis has been tested with a variation of the VGs location. By moving the VG toward the trailing edge (x/c=0.2), the effect of the baseplate is diminished, due to the larger boundary layer compared to the base plate height. The authors also mentioned that there is a need to study the effect of the base plate in details and the simulation can be achieved in a simpler BAY model instead of using a fully-resolved VG model.

The drag force disagreement between experimental and computational results in literatures ([36] and [24]) are assumed to be caused by the presence of the baseplate in the experiments. The VGs are often installed on a very thin plate before attached to the blade surface as seen in figure 1.3. This base plate has never been included in the simulations in previous research. The simulation models only take into account VGs. The actual effect of the baseplate is unknown. It could trigger the flow separation like a trip strip. In that case, VGs might fail to restore the flow separation. Besides, the baseplate configuration could also play a vital role. A nicely smooth beveled baseplate might have no effect to the flow. However, a sharp beveled baseplate could obstruct and trigger flow separation. Hence, this thesis hopes to contribute toward the body of research by adding in baseplate into the VGs model.

Figure 1.3: Smart Blade® Vortex Generators [33]

The main objective of this research project is ***"To identify the effect of the baseplate of the vortex generators by performing an analysis on selected airfoils and comparing the results against existing experimental data".*** In order to accomplish this objective, the following sub-objectives are needed.

- Sub-Objective 1: Adding baseplate into the computational airfoil model
- Sub-Objective 2: Investigate different baseplate shapes and their effect (turbulence model, roughness model, Reynolds numbers, and baseplate height) to the airfoil characteristics (lift and drag coefficients)

The questions that are needed to be answered in this research are given below. Main question 1: ***"What are the effects of the baseplate when it is included into the simulation model ?"*** This main research question can also be divided into the following sub-questions:

- Sub-Question 1.1: What are the numerical requirements needed in order to produce consistent results?
- Sub-Question 1.2: How does the baseplate effect the flow field? and airfoil characteristics such as lift and drag coefficients?
- Sub-Question 1.3: Does the VGs with baseplate model accurately predict the results (lift, drag or pressure distribution) when comparing against existing experimental data?
- Sub-Question 1.4: What is the effect of Reynolds numbers on the airfoil with baseplate configuration in terms of lift and drag coefficients?
- Sub-Question 1.5: What is the effect of the baseplate heights on the airfoil characteristics such as lift and drag coefficients?
- Sub-Question 1.6: What is the effect of surface roughness applied on the airfoil with and without baseplate in terms of lift, drag, power production and thrust?

Main question 2: ***"Should the baseplate relevance to be included in the wind turbine blade design process?"*** This main research question can also be divided into the following sub-questions:

- Sub-Question 2.1: What is the amount of drag difference between the airfoil with and without baseplate?
- Sub-Question 2.2: How does the baseplate effect wind turbine loads?

1.5 Report Outline

This report consists of four main chapters: Introduction, Vortex Generator, Numerical Modelling, Results, and Conclusion. Preliminary tasks were done at the beginning of the research and involved with literatures review, which mainly contributed to the introduction part of this report. Detail of each chapter is described in as follow:

- **Introduction**: In introduction, background and development of wind turbine industry is explained. Flow separation is also described and followed by the section describing how to control it. Research objectives and questions were also stated in this chapter.
- **Vortex Generator**: In this chapter, one of the flow separation control devices, vortex generator is explained. The mechanism of the vortex generator is given in detail in this chapter. The implementation of this vortex generator into the simulation is described in the next chapter.
- **Numerical Modelling**: This chapter details all necessary components for the airfoil with VGs and baseplate simulation. The chapter began with the description of the airfoil. Next, VGs' baseplate shapes is explained in detail and given the procedure of how to generate one. BAY model and its implementation is also explained in this chapter. Mesh strategy and flow solver set-up for prepare the simulation. In studies, detail of the studies that were performed in this research. Lastly, post-processing detailed how to perform results post-processing.
- **Results**: Results were split into two main sections: FFA W3-301 and DU 91 W2-250 airfoils. For each airfoil, series of studies were performed and discussed.
- **Conclusion**: Summary and conclusion of this research is detailed in this chapter.

CHAPTER 2 Vortex Generators

Vortex generators (VGs) were first introduced by Taylor [40]. Early applications were improving airfoil/wing performance [22] by controlling flow separation. One of the applications of VGs in aerospace industry was that, it can improve flow separation over the wing and result in increasing lift [17]. As mentioned in the introduction, size of the wind turbine rotor is increasing and thicker blades are prone to flow separation. Therefore a flow separation control device is needed. VGs were adopted into wind turbine industry in order to control unwanted flow separation at the blade root section. The device has proved to be beneficial to the wind turbine industry by improving the annual energy production (AEP) of a MOD-2 wind turbine [39] by 11%. The function of the vortex generator is to add the momentum into the flow in order to increase the turbulent mixing between the outer and inner regions of the boundary layer. Such a passive control system can be easily installed on a wind turbine blade.

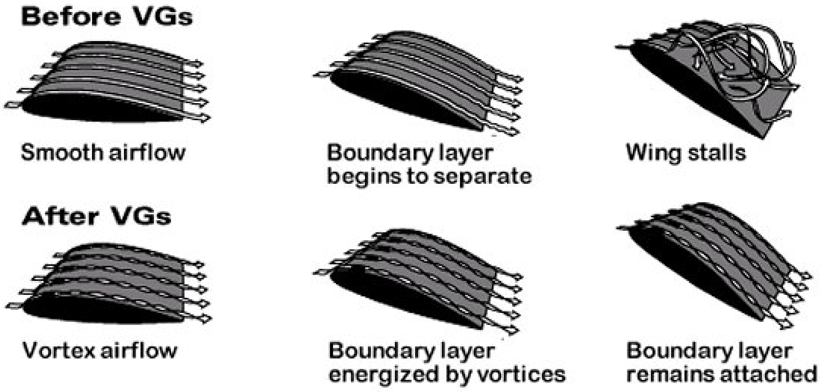

Figure 2.1: Vortex generator effect on an airfoil section [42]

Figure 2.1 illustrates how the VGs control the flow separation over an airfoil section with moderate thickness. The airfoil section without VGs is shown in the first row. At low incidence, flow over the airfoil is smooth. Boundary layer still attaches to the surface of the airfoil as it shown in the first figure in the first row. By increasing the incidence angle, the boundary layer is thickening and eventually separates at an incidence. From the last figure in the first row, it is seen that the wing is stalled at an incidence angle and the flow is fully separated which results an abrupt loss in lift. Flow for the airfoil with VGs is shown in the second row of figure 2.1. Boundary layer on the airfoil still attaches by inserting momentum into the flow using VGs, hence flow separation is delayed. This mechanism is shown in the second row of figure 2.1. Although, VGs can prolong the lift polar of the airfoil section, it also introduces additional parasitic drag.

2.0.1 VG modeling

Airfoil characteristic, such as lift and drag forces, is an essential input for a wind turbine blade design. Using experimental data is expensive and time-consuming. Therefore, it is necessary to be able to acquire accurate numerical results for an airfoil with VGs.

Fully modelling the whole VGs on a wind turbine blade is computationally expensive. A comparison between the EllipSys Fully-Resolved and EllipSys BAY models have been done recently by Troldborg et al. [44] and Manolesos et al [24]. In the first paper, both models predicted accurately the lift results until before separation occurs. However, for drag polar, both models agreed with each other but underpredicted when compared to the experimental results. The detail of the experimental results used in the first paper was reported in [51]. The actual thickness of the baseplate was not detailed in the report, although the baseplate actually existed. The obvious difference between numerical and experimental results was the presence of the VGs' baseplate in the experiment. The more recent publication by Manolesos et al. [24] also showed comparisons between various types of numerical methods for VG simulation, including the one with EllipSys Fully-Resolved and EllipSys BAY model. Both lift force results, were in good agreement with each other. This study also showed that the lift curve has a good agreement between all RANS simulations and experimental results where the separations were imminent. Therefore, it is more practical to use the BAY model to simulate the airfoil section with VGs instead of using Fully-Resolved models.

CHAPTER 3 Numerical Modelling

This chapter detail the set-up of the critical elements used in the numerical solutions performed in this thesis; 1) Airfoils 2) VGs' Baseplate 3) BAY Model 4) Mesh strategy 5) Flow-Solver Set-Up 6) Studies 7) Post-processing

3.1 Airfoils

Two airfoils namely FFA W3-301 and DU 91 W2-250 are studied in this research. Airfoil experimental data for this research is acquired from University Stuttgart [51] and TU-Delft [42]. The airfoil profiles are illustrated in figure 3.1.

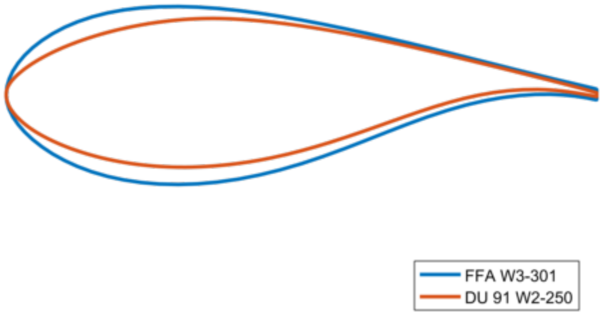

Figure 3.1: Airfoil profiles for FFA W3-301 and DU 91 W2-250

- FFA W3-301 is a relatively thick airfoil with a maximum thickness of 30%c. The airfoil has been used for the inboard section of wind turbine blades. The airfoil coordinate was developed by Björck [3]. The description of the experiment on this airfoil section and the wind-tunnel description can be found in table 3.1. The airfoil section has chord of 0.6 m in the experiment. The VGs are triangular with the counter-rotating configuration as seen in figure 3.2. A description of the VGs can also be found in the same table.
- DU 91 W2-250 airfoil was designed in Delft University of Technology [42]. The airfoil has 25%c thickness. The detail of the experiment on the airfoil section and the wind-tunnel description can be found in table 3.1. The VGs are in counter-rotating configuration as shown in figure 3.2. .

A small distance ($0.01d_4$) is needed between VGs leading-/trailing- edge and the baseplate in order to ensure that the VGs located on the right position.

In order to perform the simulation, the airfoil is normalized with chord. Thus, the Reynolds numbers are changed to 5×10^6 for FFA W3-301 airfoil and 3.333×10^6 for DU 91-W2-250 airfoil.

3.2 VGs' Baseplate

VGs' baseplate has not been included in any prior research. The novel contribution that this study brings in the area of VG research is to add the VGs' baseplate into the airfoil's profile. The thickness and length of the baseplate can be found in table 3.1. In the experiment at TU-Delft, the bevel was smoothened out the step by sticky tape, which is similar to one of the baseplate shapes no.1 in figure 3.3. The exact geometry of the baseplate beveled is unknown in the experiments performed by University

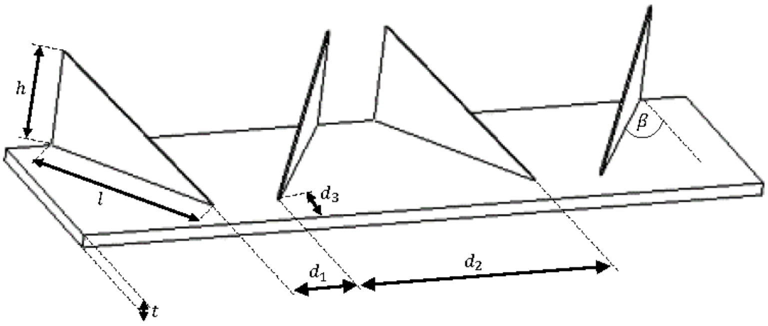

Figure 3.2: VGs and VGs' Baseplate Configuration

Wind-Tunnel		
	FFA W3-301	**DU 91 W2-250**
Configuration	Closed-return type	Closed-return type
Section [m^2]	-	1.25 × 1.8
Wall Type	Solid	Solid
Turbulence Intensity	<0.07%	<0.07%
Airfoil Section (as the in experiments)		
Chord [m]	0.6	0.6
Span [m]	-	1.25
Reynolds number	3×10^6	2×10^6
Aspect Ratio	-	2.08
Vortex Generator		
Configuration	Counter rotating	Counter rotating
Shape	Triangular	Triangular
VGs locations (L_{VG})	0.25c, 0.30c	0.20c, 0.30c
VG's height (h)	0.01c	0.0083c
VG's length (l)	0.04c	0.0283c
VG's AoA (β) **[deg]**	15.5	16.4
Distance between individual VG (d_1)	0.05c	0.0167c
Distance between each pair (d_2)	0.04c	0.0417c
Distance between VG's leading edge to the bevelled (d_3)	0	0.015c
Baseplate's length (d_4)	0.04c	0.0433c
Baseplate's thickness (t)	$6.67c \times 10^{-4}$	$6.67c \times 10^{-4}$

Table 3.1: FFA W3-301 and DU 91 W2-250 airfoils Description

Stuttgart. Therefore, various baseplate beveled shapes are studied. Five baseplate shapes are studied as show in figure 3.3-3.7. The detail of how each baseplate is modelled, is in the following sub-sections. The baseplate leading edge and trailing edge are symmetrical.

3.2.1 BP1 (beveled edge)

In the experiment at TU-Delft, baseplate bevel is smoothened with a sticky tape. This could be similar to the beveled shape in fig 3.3. The baseplate bevel is constructed with two points and are described

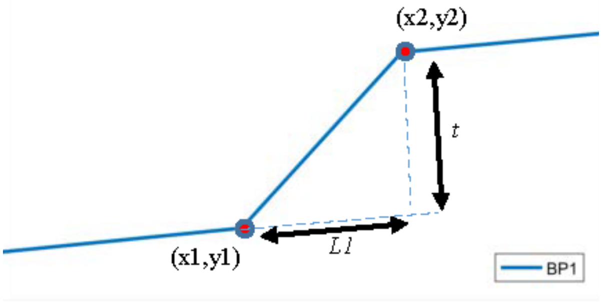

Figure 3.3: BP1 Configuration

as follow:

$$x1 = L_{vg} - offset - L1 \tag{3.1}$$

where L1 is equal to the baseplate thickness and L_{VG} is VGs location. Offset is 1% of the baseplate length as seen in table 3.1. y1 is the airfoil coordinate corresponding to x1.

$$x2 = L_{vg} - offset \tag{3.2}$$

y2 is the airfoil coordinate at x2 and added by the baseplate thickness.

3.2.2 BP2 (sharp bevel)

Baseplate shape no.2 represents what is expected when the bevel of the baseplate is not treated and is shown in figure 3.4. The detail of the coordinates are as follow:

$$x1 = L_{vg} - offset \tag{3.3}$$

y1 is the airfoil coordinate corresponding to x1.

$$x2 = x1 \tag{3.4}$$

and

$$y2 = y1 + t \tag{3.5}$$

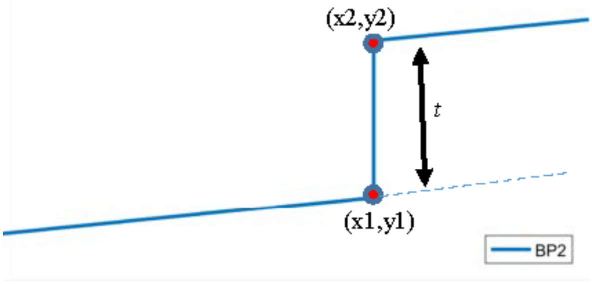

Figure 3.4: BP2 Configuration

3.2.3 BP3

Baseplate shape no.3 is a modification of previous shape. The bevel of the baseplate is chamfered with the radius of half of the baseplate thickness (t) as shown in figure 3.5. The detail of the coordinates are as follow: The chamfered radius is half of the baseplate thickness as follow:

$$r = t/2 \tag{3.6}$$

$$x1 = L_{vg} - offset - L1 \tag{3.7}$$

where *L1* is half of the baseplate thickness. y1 is the airfoil coordinate corresponding to x1.

$$x2 = x1 \tag{3.8}$$

and

$$y2 = y1 + L1 \tag{3.9}$$

x3 is at the baseplate location subtract by offset.

$$x3 = L_{vg} - offset \tag{3.10}$$

And y3 is the airfoil original coordinate corresponding to x3 and added by the baseplate thickness.

At least five points are generated between point 2 and 3 using the following equations:

$$x_i = L_{vg} - offset - (rcos(\theta)) \tag{3.11}$$

$$y_i = y_{i-temp} + (t/2) + (rsin(\theta)) \tag{3.12}$$

where y_{i-temp} is the y coordinate corresponding to x_i and r is equal to half of the thickness.

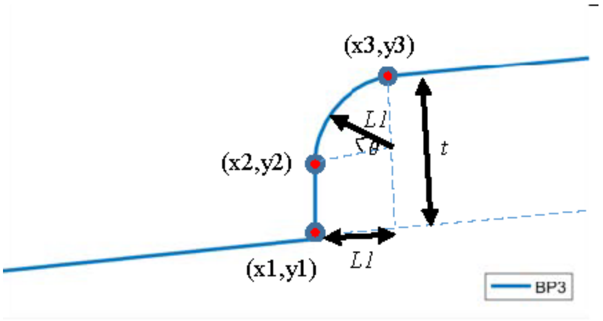

Figure 3.5: BP3 Configuration

3.2.4 BP4

Baseplate shape no. 4 is similar to previous shape but the bevel is chamfered with the radius of the baseplate thickness. The detail of the shape is as follow:

$$x1 = L_{vg} - offset - L1 \tag{3.13}$$

where *L1* is the baseplate thickness. y1 is the airfoil coordinate corresponding to x1. x2 is the baseplate location subtract by offset as shown in following equation:

$$x2 = L_{vg} - offset \tag{3.14}$$

y2 is the airfoil original coordinate corresponding to x2 and add by the baseplate thickness.

At least five points are generated between point 1 and 2 using the following equations:

$$x_i = L_{vg} - offset - (L1cos(\theta)) \tag{3.15}$$

$$y_i = y_{i-temp} + (L1sin(\theta)) \tag{3.16}$$

where y_{i-temp} is the y coordinate corresponding to x_i.

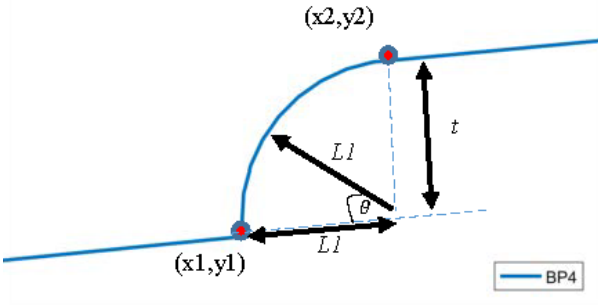

Figure 3.6: BP4 Configuration

3.2.5 BP5 ("S" shaped bevel)

Baseplate shape no.5 is similar to baseplate shape no.3 except that the bottom part of the baseplate is also smoothen with a curve. The geometry detail is as follow:

$$x1 = L_{vg} - offset - L1 \tag{3.17}$$

where *L1* is the baseplate thickness y1 is the airfoil coordinate corresponding to x1. x2 is the baseplate location subtract by offset.

$$x2 = L_{vg} - offset - L1/2 \tag{3.18}$$

And y2 is the airfoil original coordinate corresponding to x2 and added by half of the baseplate thickness.

$$x3 = L_{vg} - offset \tag{3.19}$$

y3 is the airfoil original coordinate corresponding to x3 and added by the baseplate thickness. At least five points are generated between point 1 and 2 using the following equations:

$$x_i = L_{vg} - offset - r(2 - cos(\theta)) \tag{3.20}$$

$$y_i = y_{i-temp} + r(1 - sin(\theta)) \tag{3.21}$$

where y_{i-temp} is the y coordinate corresponding to x_i and r is equal to half of the thickness. Between point 2 and 3, number of points are also generated as follow:

$$x_i = L_{vg} - offset - rcos(\theta) \tag{3.22}$$

$$y_i = y_{i-temp} + r(1 + sin(\theta)) \tag{3.23}$$

3.3 BAY Model

A more efficient method is needed to replace the fully-resolved gridded model. One such method to utilize the BAY model [10] where the VGs are modeled as a force which is applied perpendicular to the flow direction parallel to the surfaces where the VG is located. This method allows us to numerically insert a VG without actually having model one. Figure 3.8 illustrates the definition of each parameter that has been described in the BAY model.

Though the method saves a vast amount of computational cost, it has some drawbacks. In the early model from Bender et al [10], the solution for the original BAY model depends on the VG calibration coefficient (C_{VG}) and total volume of cells (V_M) which the source term is applied. Calibration is required in order to achieve accurate and reasonable results without modification on the original BAY model. Many studies have been done in order to tackle the problem as illustrated in figure 3.9.

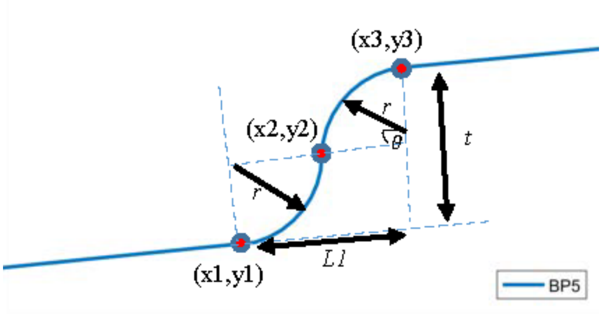

Figure 3.7: BP5 Configuration

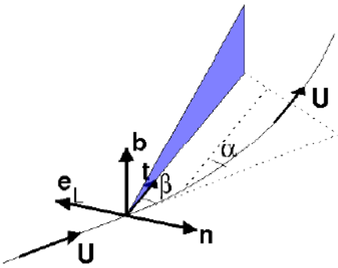

Figure 3.8: Sketch of VG definition according to BAY model [45])

Figure 3.9 illustrates various cell selection method, which has been proposed to tackle the original BAY model limitation. First row of the figure, shows how cells were selected in the original BAY model. Number of rows were selected and the results were validated against experimental or fully-resolved gridded model results.

On the second row of the figure 3.9 depicted oblique row selection method [18]. Only one row of cells is selected in this method. This method showed that calibration can be neglected when the VG calibration coefficient is over 10. Besides, this method can reduce the mesh size.

Brunet et al. [6] had proposed a method used for selecting cells where VG is located. The same method is used for immersed boundary conditions. Schematic of the cells selection method is shown in the third row of figure 3.9.

A new source term model was proposed by Wallin & Eriksson [48]. Forces that insert into the fluid by VGs, are in term of rate of change of the local normal body-force, the model constant and the velocity vector. The method for force allocation is similar to the one that was proposed earlier by Jirasek [19].

One of the successful approaches was introduced by Jirasek [19] (jBAY model). The VG is treated as thin airfoil (zero thickness). Instead of selecting the number of rows of cells as in the original model, two closest cells that the VG intersects are selected (see figure 3.9). The flow parameters are linearly interpolated from the grid nodes to these cells. The side force is calculated from equation 3.24 and redistributed back to the grid nodes. This technique has improved the original BAY model such that the model is no longer dependent on calibration coefficient and total volume of cells. The VG source term modelling that used in this research is similar to jBAY model.

$$L_i = C_{VG}\rho A_i|U|^2\alpha e_L \tag{3.24}$$

where $e_L = (U \times b)/|U|$, with small angle approximation: $\alpha = (Ut)/|U|(Un)/|U|$
A previous study [43] has shown that the result is insensitive to an increase in the model constant ($C_{VG} > 1$).

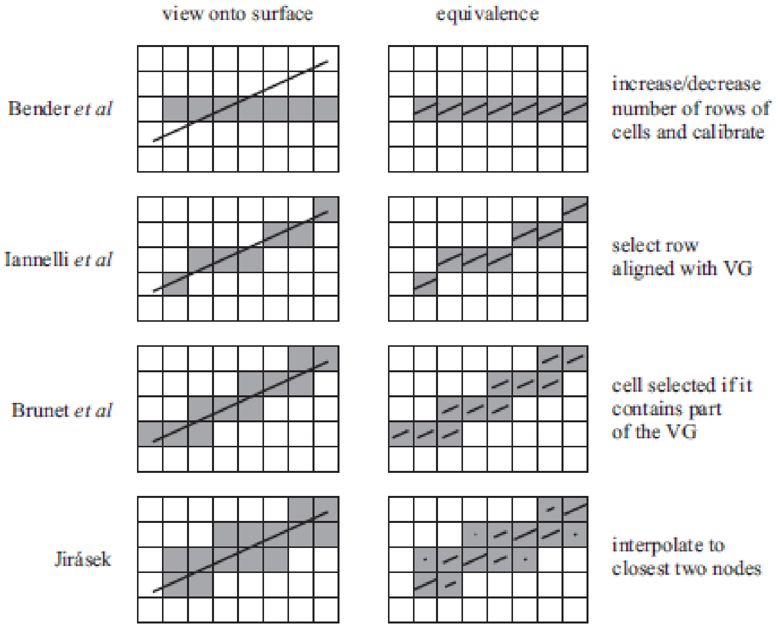

Figure 3.9: VG modeling techniques [4]

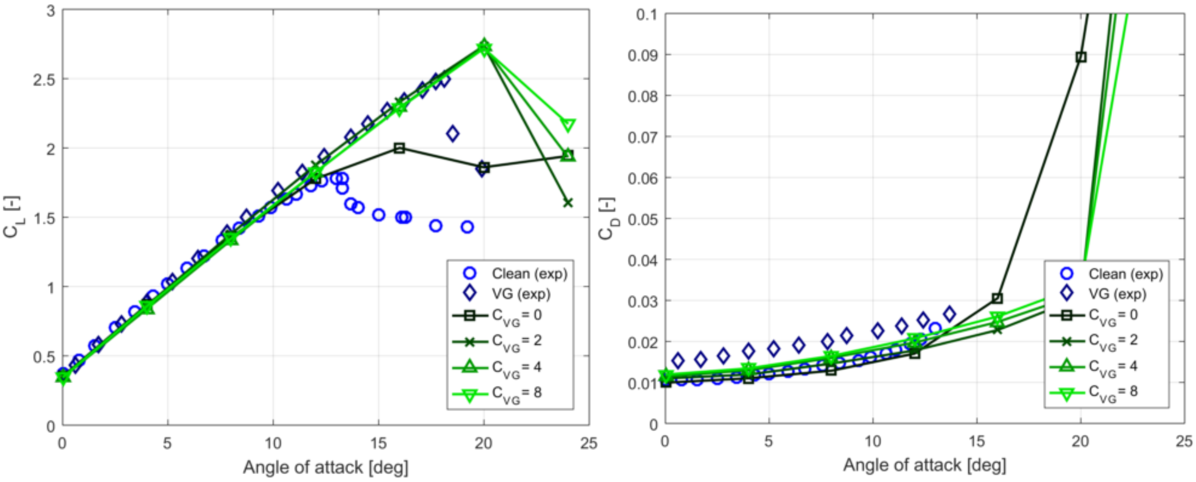

Figure 3.10: Comparison of lift and drag curves for the FFA-W3-301 airfoil calculated using different model constant (C_{VG})

The model constant is studied on the FFA W3-301 airfoil with e^N transition model and $k-\omega$ SST turbulence model. Figure 3.10 showed lift and drag coefficients against angle of attacks. The results show that they are insensitive for ($C_{VG} > 2$) which is in agreement with previous work by Troldborg et al. [44]. However, there is a slight difference for drag coefficients at high angle of attacks (> 12 degrees) but the curves follow the same trend. Further study on the effect of the forces from the BAY model will be shown in the results chapter. To ensure that the model constant does not influence the results, $C_{VG} = 4$ will be used throughout the research.

3.4 Mesh Strategy

After airfoil profiles with baseplate are generated, 2D and 3D mesh generation can be performed. Mesh generation is another crucial part of this research. In order to be able to simulate an airfoil, one must generate a neatly distributed computational grid around the airfoil.

The 2D computational grid will be generated using HypGrid2D [35]. The airfoils that will be studied in this literature have a blunt trailing edge, hence an O-mesh type is suitable for this research. The goal of the mesh generation is to create a neatly distributed of mesh around an airfoil avoiding unnecessarily distorted mesh elements. The grid size at the wall should be small enough in order to be able to resolve the boundary layer, hence the first non-dimensional distance from the wall (y^+) must less than 2. The grid is stretching in the normal direction using a hyperbolic tangent function.

A previous study by Sørensen et al. [36]; showed that 2D airfoil simulation results done on the clean airfoil in fully turbulent condition with the far-field located at 16 and 32 chords were identical. The appropriate size of the flow field should not be too large as the far-field cells could have bad aspect ratio compared to the one close to the airfoil and as well as cells in the spain-wise direction for 3D simulation. Too much stretching to the far-field with high number of grid size in the normal direction (N_C) could introduce simulation instability. Similar study is performed on FFA W3-301 airfoil with VGs. Figure 3.11 shows the FFA W3-301 airfoil with difference grid size in the normal direction of 16 and 32 chords. The simulations of both grid sizes are performed with e^N transition model and $k-\omega$ SST turbulence model. The VGs are also included in the simulations. The number of cells in the span-wise direction is 32 with the span of 0.36. The aspect ratio of the span-wise distance to the number of cells (S/N_c) is 0.01125. The number of cells in the normal direction is 128. The cells distribution in the normal direction is stretching using hyperbolic-tangent function, therefore exact aspect ratio cannot be calculated. The average aspect ratio of the far-field distance to the number of cells in the normal direction is 0.128 (for 16 chords) and 0.25 (for 32 chords). From figure 3.11, it is seen that both configurations are congruent in both lift and drag coefficients. A small differences can be noticed after the stall in the lift curve, and it is negligible. In order to keep the aspect ratio of the far-field grid at minimum, grid size in the normal direction of 16 chords is chosen for further study.

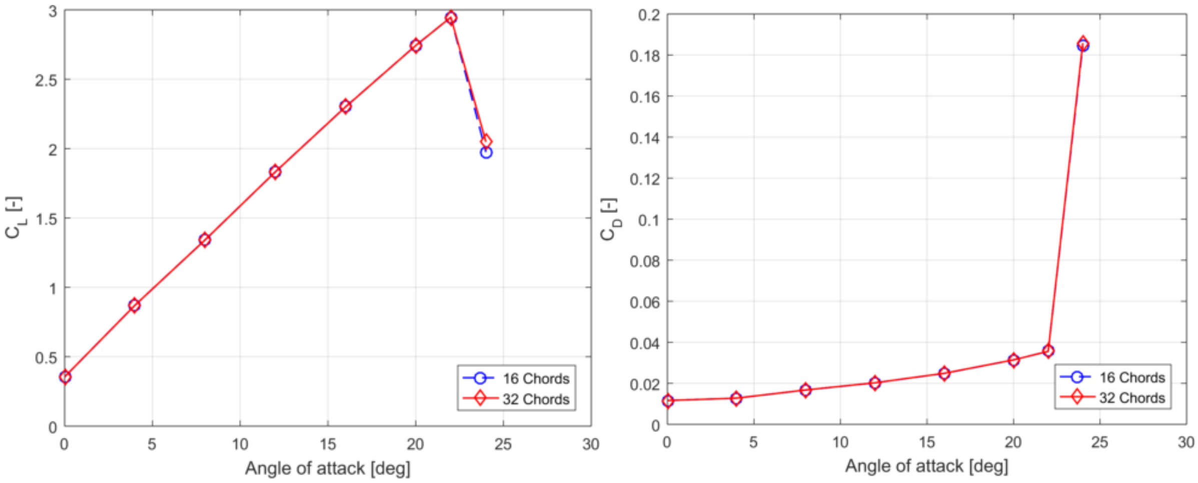

Figure 3.11: Comparison of lift and drag curves for the FFA-W3-301 airfoil with different grid size in the normal direction (N_C) 16 and 32 chords

The number of cells around the airfoil depends on the shape of the airfoil. Cells are clustered around the leading edge of the airfoil in order to conform the curvature of the airfoil as illustrated in figure 3.12 and 3.13.

An airfoil section with a baseplate needs more cells in order to conform to the shape of the baseplate. In some cases a minimum of 10 cells are required at the edge of the baseplate. This depends on the

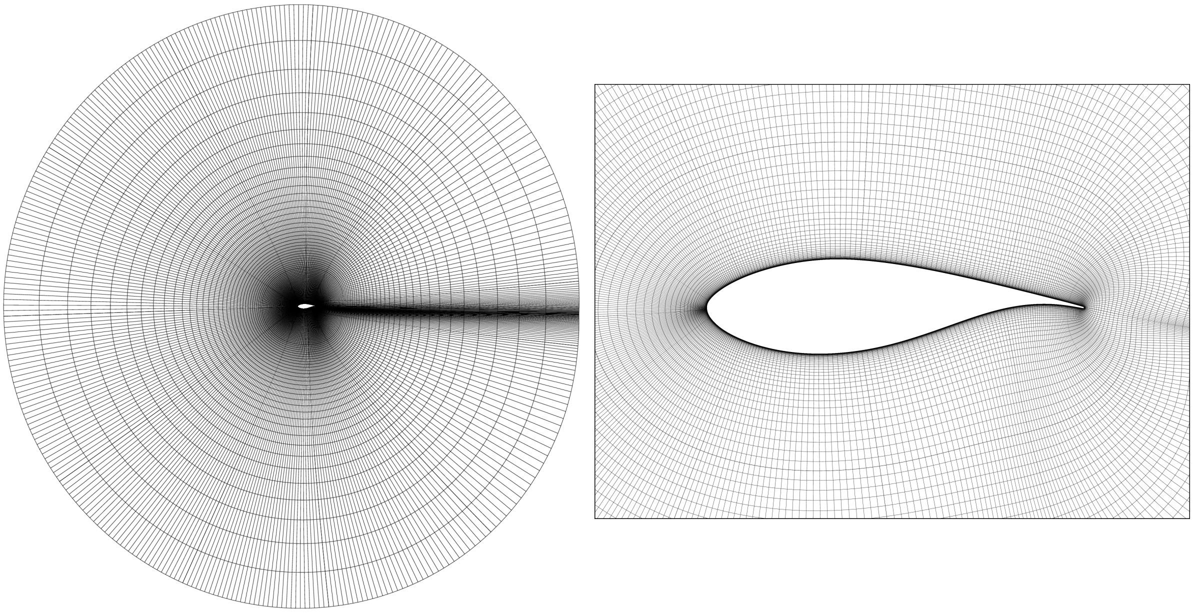

Figure 3.12: Airfoil O-mesh for FFA-W3-301

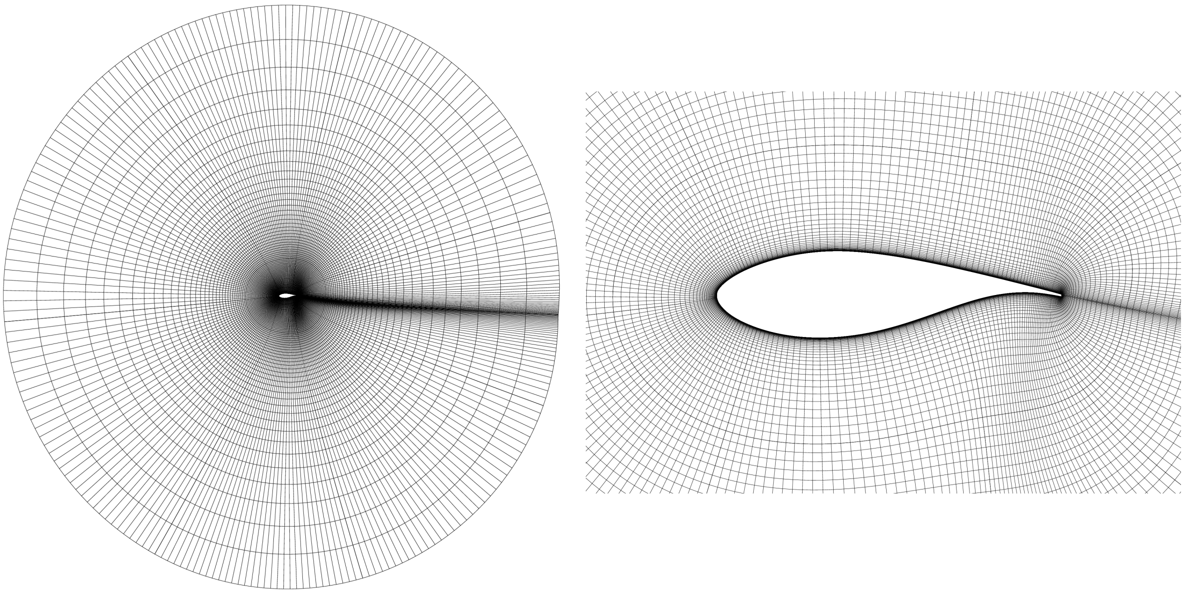

Figure 3.13: Airfoil O-mesh for DU-91-W2-250

geometry of the bevel of the baseplate. Also, cells at the bevel of the baseplate are clustered. The airfoil with the baseplate shape no.2 is meshed and shown in figure 3.14.

After the 2D grid generation is done, the mesh is then extruded into the 3rd dimension using inhouse pre-process tool. This 3D-extrusion method has one limitation. The baseplate is also extruded continuously along the span, whereas in practical at Suzlon, there is a space between each pair of VGs with an individual baseplate. Block size is specified in this step. A block should have a proper size so that the information transfer between each block is numerically stable. The block size of 32 is used for the whole research. The number of vertices in the span-wise direction should be divisible by the size of

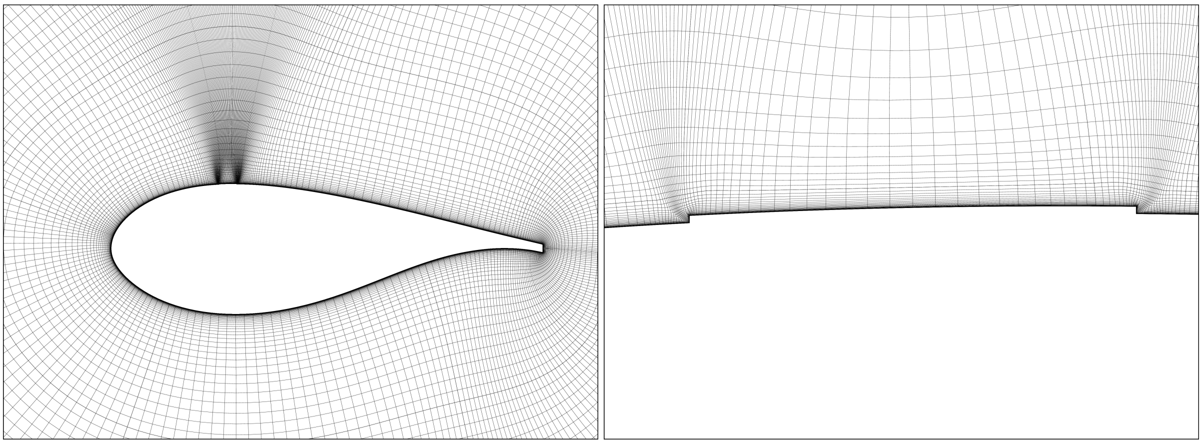

Figure 3.14: Mesh generation of FFA-W3-301 airfoil with the baseplate shape no.2

the block. A proper number of vertices in the span-wise direction are defined in the resolution study.

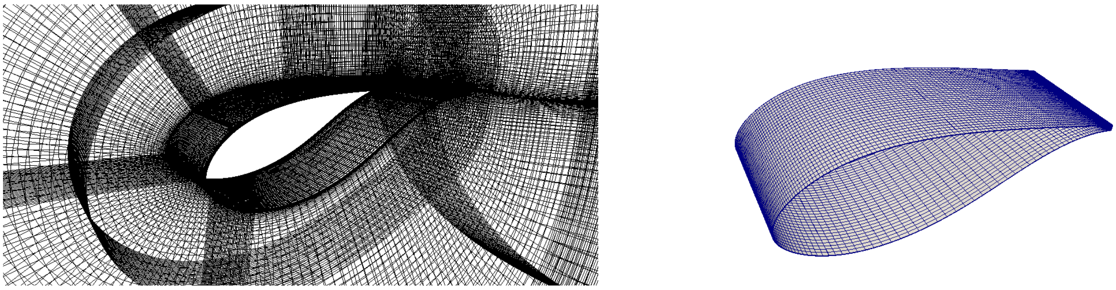

Figure 3.15: 3D grid around FFA W3-301 airfoil

3.5 Flow-Solver Set-Up

In order to perform the simulation, an input is needed for the flow solver. The summary of the input that is used in this research can be found in table 3.2.

The simulations are done from the coarsest grid (grid level 3) to the finest grid (grid level 1) in order to enhance the computational speed. In the case of the airfoil with VGs, the simulation is performed at grid level 1. This is because if the simulation starts at the coarsest grid, the presence of the VGs might be omitted as the grid size is much larger than the VGs configuration. The results from the coarsest grid without taken VGs into accounted will transfer to the finer grid and result in error accumulation. Figure 3.16 shows vorticity (left hand-side) and contours plots (right hand-side). From row 1 to 3 of figure 3.16, the simulations are run at grid level 3 to 1 respectively. It is seen that the flow is not energized (in (a) and (c)) and formed vortexes as in (e). Far wake is also large as the simulation is done in the coarse grid level (b and d). To avoid the large far wake, grid level 1 is chosen for the airfoil with VGs.

An additional computational speed enhancing tool, Multigrid is implemented in sub-iterations. The convergence criteria of this simulation is 1E-5 or when it fluctuates about a value. The e^N transition model (A.2.2) is used for the simulation. The $k-\omega$ SST turbulence model (A.2.1.4) is used in this research, as the model can accurately predict adverse pressure gradient and has no far-field parameters dependency. The QUICK scheme (A.3.4) is used at grid level 1 in order to ensure the accuracy and Reynolds stresses transportiveness. The SUDS (A.3.3) is used on other grid levels for numerical stability and avoiding nonphysical oscillatory behavior. The SIMPLE method (A.4) is used for pressure correlation. In this research, cyclic boundary condition is used instead of symmetric boundary condition as it gives a better numerical stability for the airfoil section with VGs. The simulation of the airfoil section with VGs has a repeated pattern in flow, hence symmetric boundary condition is not satisfied. With cyclic boundary condition, one end of the airfoil section will have the same result as the another end. However, the drawback to using such a boundary condition is that this boundary condition could influence 3D stall behavior or stall cell over the airfoil section. In the experiment wall boundary layer might have an effect to the airfoil flow field, which is not considered in this simulation.

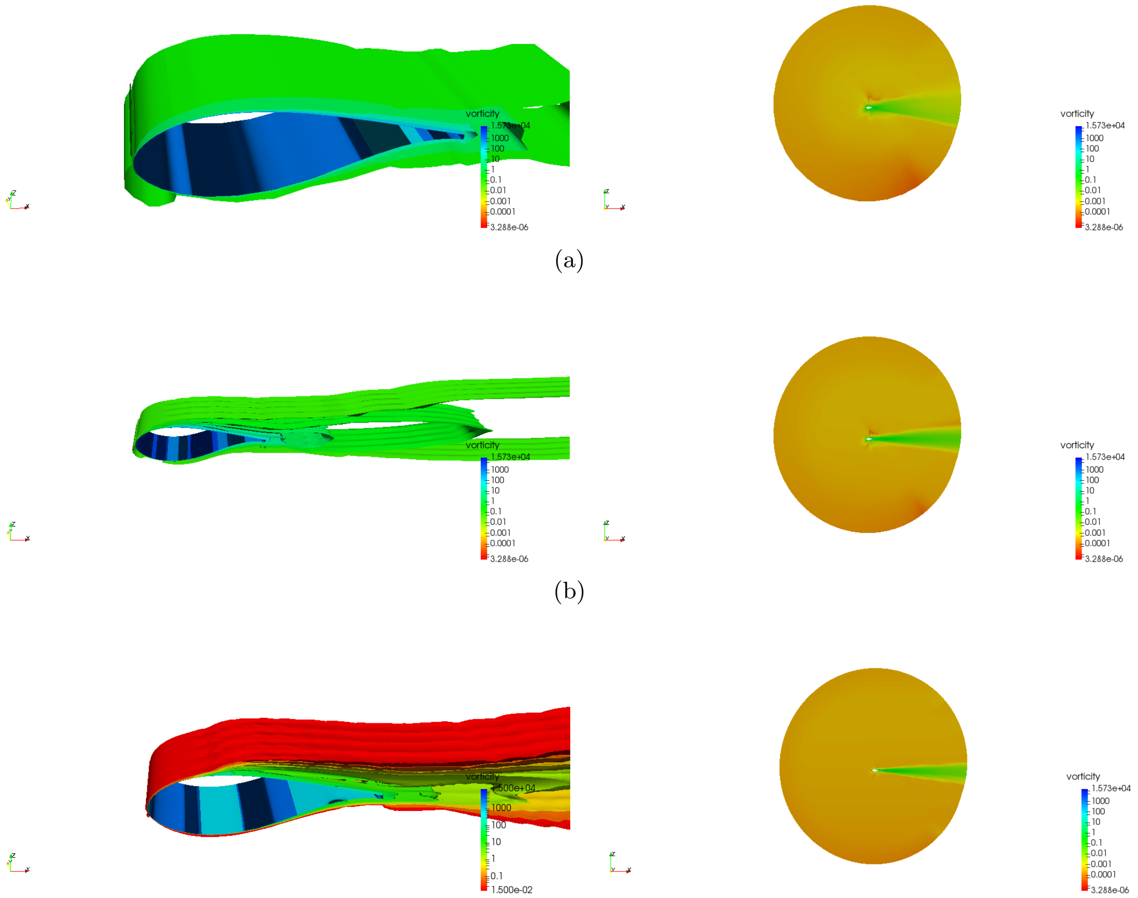

(a)

(b)

(c)

Figure 3.16: FFA W3-301 airfoil at different grid level a) 3, b) 2, c) 1

3.6 Studies

The following series of studies are performed in order to analyze the effect of the VGs' baseplate.

3.6.1 Resolution Study

Grid study will be done in order to ensure that the computational grid is span-wise directional independent. An airfoil with baseplate will be meshed. A baseplate beveled edge would be the first approach

$Parameter$	$Value$
No. of outer iterations	3 [15000 5000 3000]
No. of inner iterations	8
Convergence criteria	1E-5
Differencing scheme	QUICK SUDS SUDS
Pressure correction	SIMPLE
Grid level	3
Turbulence model	$k - \omega \ SST$
Transition model	Drelaś $e^N method$

Table 3.2: Flow-solver input

to relax the limitation of the grid generation. Later on the more realistic sharp edge could be studied based on the knowledge and experience gained from the previous configuration. Based on the grid study, the necessary grid parameters will be chosen and used in the remaining study.

3.6.2 Transition Study

Transition study need to be done in order to select an appropriate N value for the e^N transition model (A.2.2). Validation of an appropriate N value will be done on the clean airfoil. The N value that gives the closest lift and drag force to the experimental results will be used in the further study portion of this research.

3.6.3 Effect of VGs' baseplate

Airfoil profiles with baseplate are simulated with and without VGs. This study aims to investigate the effect of the baseplate on the airfoil characteristics such as lift and drag coefficients. Besides, pressure and friction coefficients of the airfoil with and without baseplate are also studied. This section comprises of following sub-sections: Only VGs, VGs' Baseplate, and VGs & Baseplate. All results will be compared and discussed in this section.

3.6.4 VGs' Position

VGs' position is studied in order to investigate whether the VGs location affect the flow separation. It is known that there is no benefit if VGs install behind the separation location. That is because after the flow is separated, the boundary layer increases and as a consequence the VGs are submerged in the boundary layer. Various VGs' position are studied according to available experimental data.

3.6.5 Reynolds Number Study

Reynolds number study is performed on FFA W3-301 and DU 91-W2-250 airfoils. It is expected that as the Reynolds number increases, the effect of the baseplate could be demised as the boundary layer thickness shrink. The simulations are performed with e^N transition model and $k - \omega$ SST turbulence model.

The airfoils with VGs, VGs & Baseplate are studied in order to analyze the effect of baseplate. Selected baseplate shape no. 1, 2 and 5 are studied. FFA W3-301 airfoil is simulated with the Reynolds numbers of 5×10^6 and 8×10^6. DU 91-W2-250 airfoil is simulated with the Reynolds numbers of 3.33×10^6 and 5×10^6.

3.6.6 Baseplate height Study

Baseplate's height study is performed. The baseplate height of 0.667c$\times 10^{-3}$ and 1.000c$\times 10^{-3}$ are studied. The baseplate shape no.1, 2 and 5 are simulated in this study. The VGs are located at 0.25c.

This study will illustrate the effect of the baseplate height to the flow field. It is expected that if the height increases, the airfoil performance will be worse.

3.6.7 Roughness Study

In a real world application, a wind turbine might encounter gust or swarm of insects. Such occurrences damage the wind turbine blades especially at the leading-edge. Therefore, it is worthwhile to investigate this effect in this thesis. The roughness model that used in this thesis is described in A.2.3. For the airfoil with roughness, the transition model is not applied. An equivalent sand grain roughness height (k_s/c) of 0.549$\times 10^{-3}$ is used in this thesis. This roughness height was measured by Kevin et al. [38], and is representatives of a 3M™ Safety-walk Type C tape. The roughness is applied to the airfoil leading edge up to 0.08c as in the experiment done by Abbott [1].

The 2.5 MW wind turbine model from 46300 Wind Turbine Technology and Aerodynamics course at DTU (C) is used as a reference wind turbine. Power and thrust for rough airfoil with VGs, VGs & Baseplate are calculated and compared to each others. The annual energy production is also computed using following equation:

$$AEP = \sum_{i=1}^{N-1} 1/2(P_i + P_{i+1} \times 8760 \times [exp(-(V_i/A)^k - exp(V_{i+1}/A)^k)][GWhr] \tag{3.25}$$

where N is the total number of the wind speed. The wind distribution is controlled by weibull parameters (A and k). These weibull parameters were computed using WAsP and data taken from a mast at FINO-2 wind farm in Baltic sea [16]. The scale weibull parameter (A) is 9 and shape parameter (k) is 2.31. The probability density function according to this weibull parameters is shown in figure C.1. The VGs are installed at the inboard part (<40% span) of the blade. The hydraulically smooth roughness height is identified by reducing the roughness height until there is no change in the forces.

3.7 Post-processing

After obtaining the results, raw data such as forces are averaged. Figure 3.17 shows an example of the logarithmic residual error between the FFA W3-301 airfoil with VGs at 4 degrees (a) and 12 degrees (b). As it is seen in sub-figure (a), the results are fluctuating about a value, whereas in sub-figure (b) the results are converged according to the convergence criteria (10^{-5}).

In order to obtain the final results, outputs are averaged in the tail end of the data. An appropriate range is selected by analyzing the numerical results qualitatively using the standard deviation (σ) which can be calculated from the following equation 3.26.

$$\sigma = \sqrt{\frac{1}{N}\sum_{i=1}^{N}(x-\mu)^2} \tag{3.26}$$

where N is the total number of data and μ is the mean of the data. Figure 3.18 shows the standard deviation of the FFA W3-301 airfoil with VGs at each angle of attack for the last 100 (a) and 1000 results (b). The standard deviations of the results are very small especially when looking at the drag coefficient. This means that the results are dispersed within a very small magnitude. The standard deviation rises as the range increased. This is because at 12 degrees the simulation has already converged. Hence, for converged simulation the results are averaged using the last 10 results. For the fluctuating raw data, the averaging is performed over the range of the data period. This range is not fixed for the whole research but rather changes on a case by case basis.

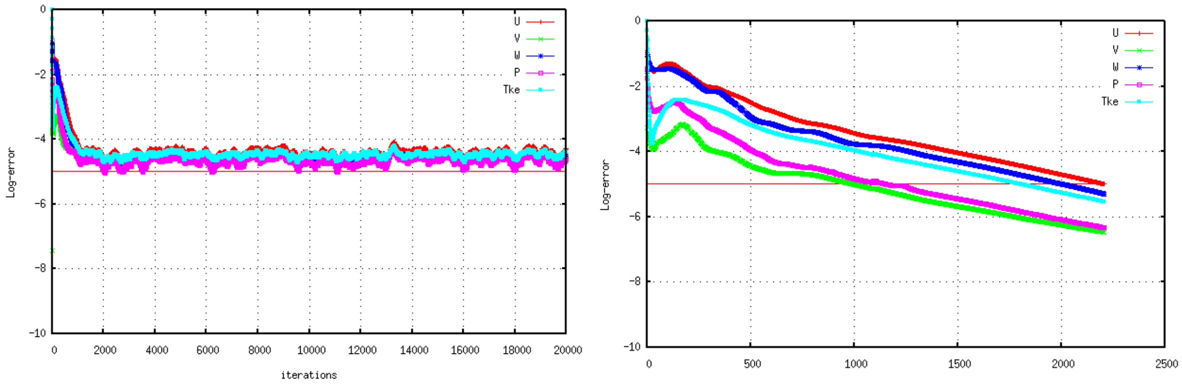

(a) (b)

Figure 3.17: Log-error vs no. iterations: a) 4 degrees b) 12 degrees

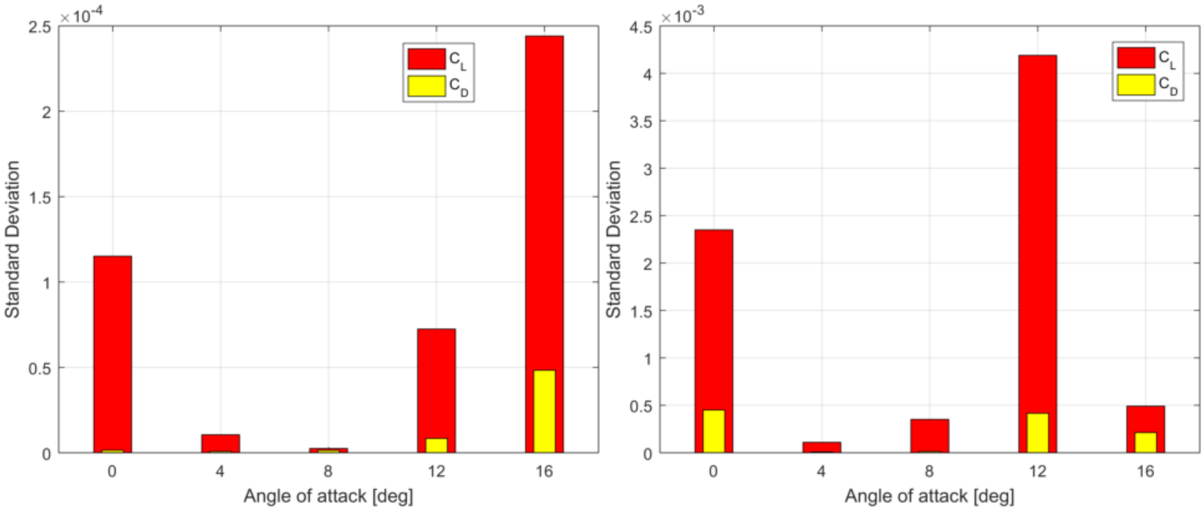

(a) (b)

Figure 3.18: Standard deviation of CFD results of FFA W3-301 airfoil with VGs a) 100 b) 1000

After which obtained the simulation results, the data is exported into VTK file format and visualizes in ParaView software. This software allows us to inspect the flow behavior in 3D.

Figure 3.19 illustrates the flow visualization of the FFA W3-301 airfoil with baseplate and VGs at angle attack of 0 degree. The figure on the left-hand side depicts stream lines over the airfoil. The figure on the right-hand side shows the vorticity contour.

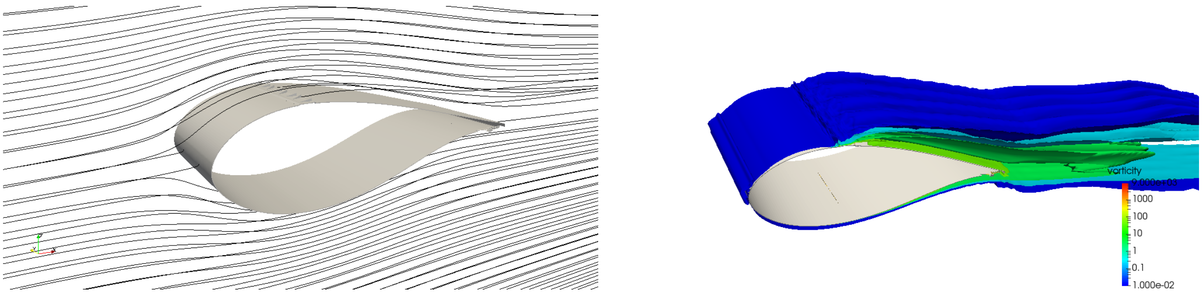

(a) (b)

Figure 3.19: Flow visualization of the FFA W3-301 airfoil with baseplate and VGs at angle attack of 0 degree

CHAPTER 4 Results

4.1 FFA W3-301

4.1.1 Resolution Study

Grid sensitivity along the span-wise direction of the airfoil section is studied. The grid study is performed on the airfoil at difference span over chord ratio ($L_{S\backslash C}$). The grid is meshed with 256 cells along the chord-wise direction (N_C), 128 cells in normal direction (N_N), and 32 cells in span-wise direction (N_S). The number of VGs (N_{VG}) vary according to the span. Table 4.1 summarizes the set-up for each grid in this study. Grid 1 has the highest span-wise resolution and resolve only one VG, whereas the grid 4 has the coarsest span-wise resolution. The simulations are performed using $k-\omega$ SST turbulence model and with e^N transition model. The N value, is defined later in the next section, is presumed to be 12. In this case, forces from the BAY model are not yet taken into account.

Grid	N_c	N_N	N_S	$L_{S\backslash C}$	N_{VG}
1	256	128	32	0.045	1
2	256	128	32	0.090	2
3	256	128	32	0.180	3
4	256	128	32	0.360	4

Table 4.1: Resolution study set-up

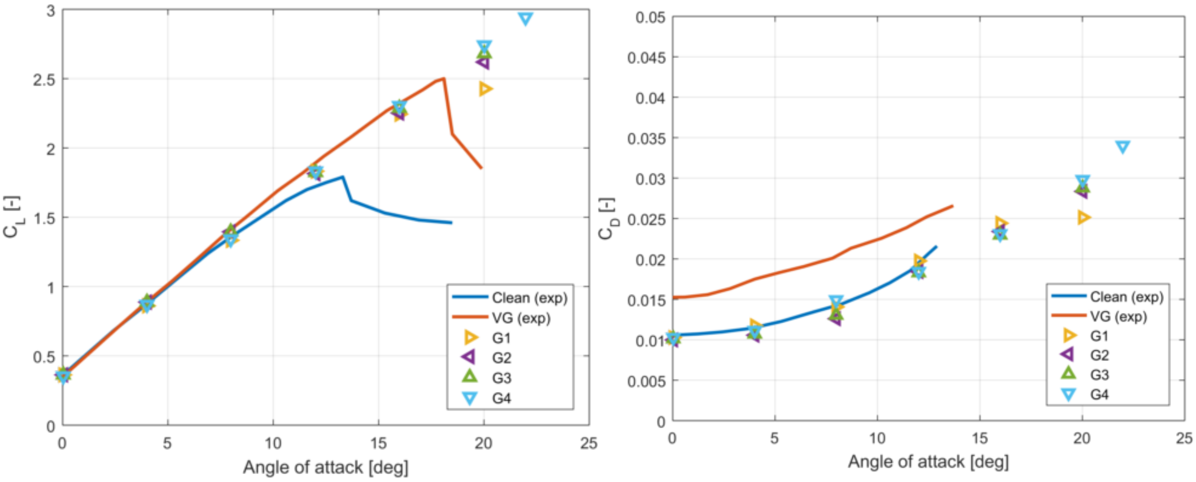

Figure 4.1: Comparison of lift and drag coefficient curves for FFA W3-301 airfoil with VGs calculated using different grid

From figure 4.1, the results show no difference between each grid for the angle of attack between 0 to 16 degrees. The numerical results agrees well with the experimental results of the airfoil section with VGs for the linear part of the lift curve. The result from grid one shows a slight disagreement at the angle of attack of 20 degrees. This could be a result of numerical issue. In order to capture the flow behavior of an airfoil with VGs accurately, one needs at least a pair of VG in the simulation (G2). This one side of VG has failed to predict lift coefficient at 20 degrees accurately. However, linear part of the lift curves are maintained, where the VGs shows that they can delay flow separation. From this study, it could be concluded that there is no difference between grid 2 to 4 and the model is shown to be span-wise insensitive. Although, all grid levels are in good agreement, some of the simulations in grid 1 to grid 3 are not fully-converged with most of them are fluctuating about a value. Therefore, for further study in this research, the grid 4 configuration is used as it gives the best numerical stability.

4.1.2 Transition Study

Transition study is performed in order to define the best N value for the airfoil simulation with the e^N transition model. An accurate N value, would give an accurate result closes to the experimental result.

Figure 4.2 illustrates the airfoil's lift and drag polar for different N values. The lift results show that there is no difference between each transition model and experimental data for the angle of attack range between 0 to 10 degrees. However, drag forces are under-predicted in the simulation. Stall angle is at the angle attack of around 13 degrees in the experiment, where it is over-predicted to around 16 to 20 degrees in the simulation.

Figure 4.3 shows the lift coefficient against drag coefficient for different N values. The results from the simulations have the same trend to the one from the experiment. However, the simulation results are seen to have a higher lift to drag ratio which caused the curve to shift towards the left hand-side of the figure by approximately 1.376×10^{-3} or 13.9% difference.

It can be concluded that there is no difference, for difference N value to the numerical results. The N value can be computed using equation A.14. The N value corresponding to turbulence intensity of 0.07% is approximately 9. For further study, $N = 12$ is chosen as all simulation results from difference N values are congruent.

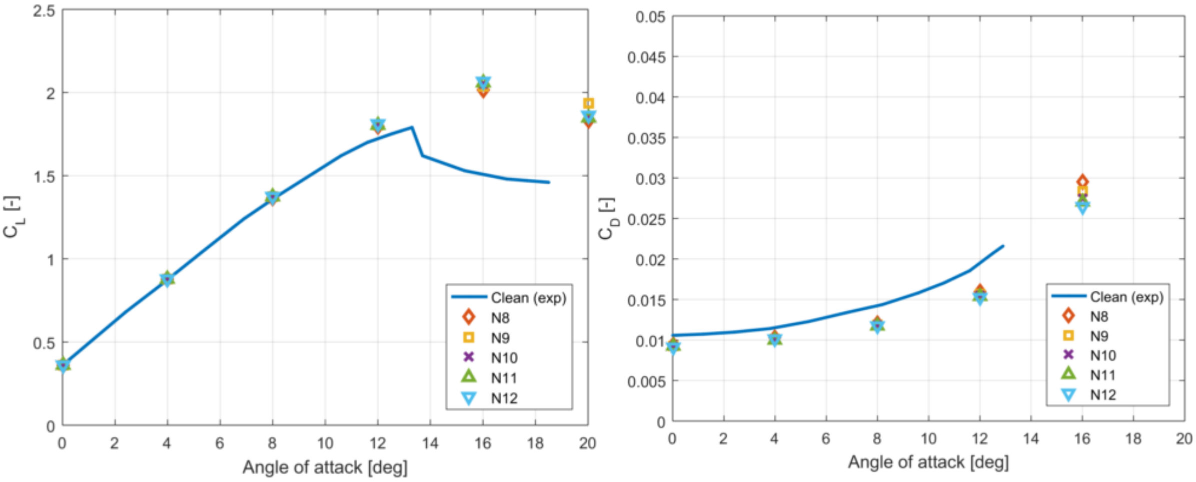

Figure 4.2: Comparison of lift and drag coefficient curves for the FFA W3-301 calculated using different N value

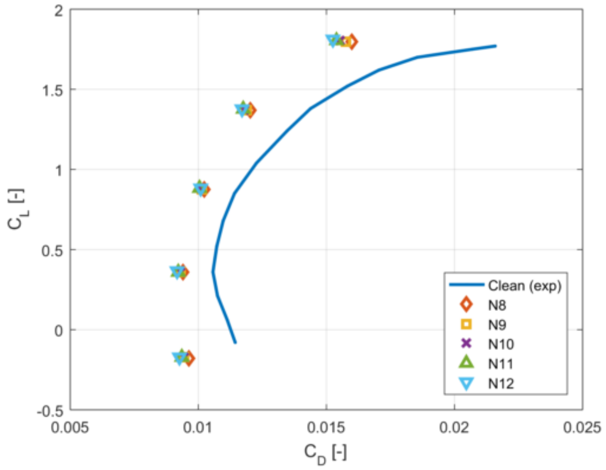

Figure 4.3: Lift vs drag coefficient curves for the FFA W3-301 with VGs calculated using different N value

4.1.3 Effect of VGs' baseplate

The results for the airfoil with VGs, VGs' baseplate, and with both VGs and baseplate are presented in this section. The simulations are performed using the N value of 12 for the e^N transition model and $k-\omega$ SST for the turbulence model. The VGs are located at 0.25c for studies in this section.

4.1.3.1 Only VGs

The study of the airfoil section with only VGs is performed. From figure 4.4, it is seen that the lift curve for airfoil with VGs from the simulation agreed well with the experimental results up to the separation point. The stall angle of attack is over-predicted in the simulation. From the lift curve, it is evident that VGs can extend the linear part of the lift curve or delay flow separation.

The drag coefficient for each case is shown on the right hand-side of figure 4.4. The numerical drag results for the airfoil with VGs without additional forces from BAY model are under-predicted when compare with experimental results. Additional drag forces from the BAY model are added into the numerical results showed in the dark red curve. The drag curve is elevated and got closer to the experimental results. The amount of increase in drag when including forces from BAY model is shown in table 4.2. It is seen that the difference is higher at low angles of attack. From the table, the maximum difference is found at 4 degrees, whereas at 24 degrees it has the lowest variation. This could be a result of the boundary layer thickness growing as the angle of incidence increases, partially be submerging in the VGs. As a result, the effect of the VGs forces is limited.

Although additional drag from BAY model had been taken into account, there is still a gap between experimental drag forces and VGs with BAY model forces. From figure 4.5, it is seen that the simulation results of the airfoil with VGs have higher lift to drag ratio compared with experimental results. This result in the curve to shift toward the left hand-side as it could be seen in the clean airfoil case. The airfoil without forces from BAY model is shifted to the left hand-side by approximately 5×10^{-3} or 32% difference compared with the experimental results of the airfoil with VGs. By including additional forces from BAY model the curve shift toward the experimental results curve. Both curves are apart by approximately 3.6×10^{-3} or 23%. The difference is approximately 10% higher than the difference in the clean airfoil case. This evidence of a disagreement between the simulation model and actual VG configuration in the experiment.

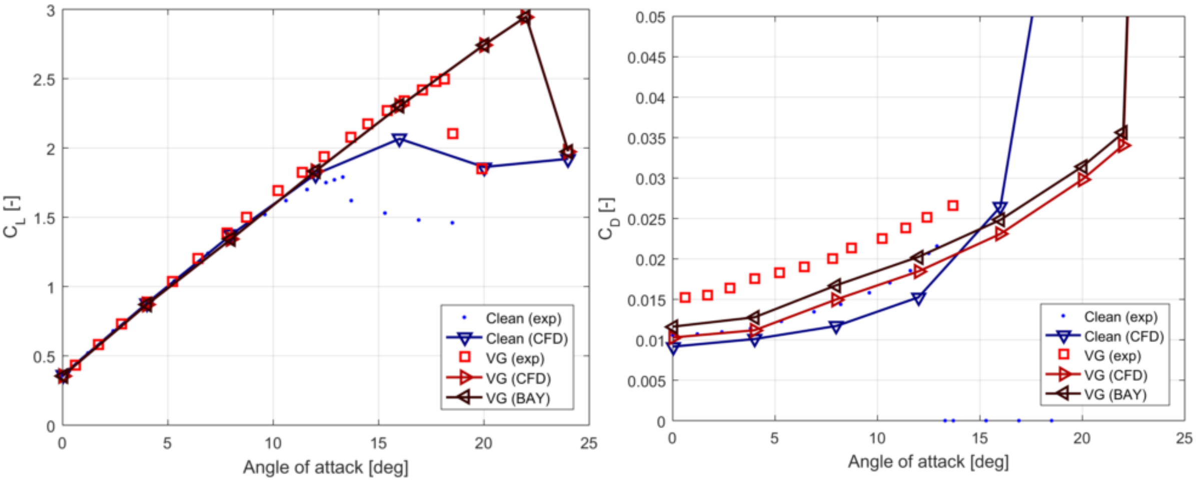

Figure 4.4: Comparison of lift and drag coefficient curves for the FFA-W3-301 airfoil with VGs

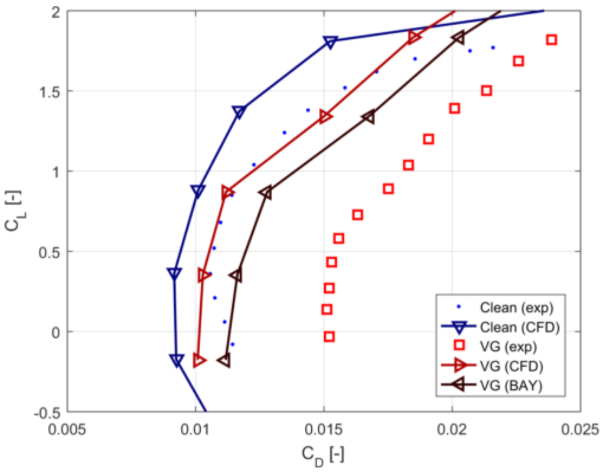

Figure 4.5: Lift vs drag coefficient curve for the FFA-W3-301 airfoil with VGs

AoA [degree]	0	4	8	12	16	20	22	24
%Difference	13.08	14.33	11.68	9.70	7.50	5.36	4.45	0.41

Table 4.2: Percentage increase in drag coefficient when including forces from BAY model

4.1.3.2 Only VGs' Baseplate

VGs' baseplate as shown in figure 3.3 to 3.7 are simulated without VGs. Figure 4.7 illustrates the lift curves for different baseplate shapes on the airfoil.

The simulation results of the airfoil with baseplate are congruent with experimental results in the range between 0 to 12 degrees. The airfoil with baseplate configurations except shape no.2 have a slightly lower maximum lift approximately 7% in comparison with the simulation results of the clean airfoil. This could be as a result of the sharp bevel of the baseplate, which could easily trigger flow separation.

The drag curves in figure 4.7 illustrates the comparison of the drag coefficient of the airfoil with different baseplate shapes. The airfoils with baseplate has higher drag than the simulated clean airfoil results. The baseplate shape no.2 has the highest drag among other shapes and simulated clean airfoil.

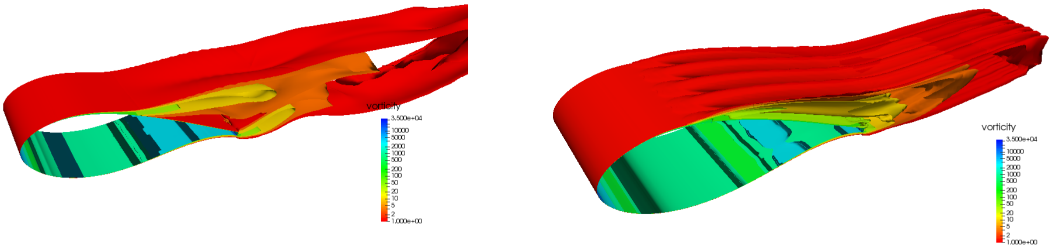

Figure 4.6: 3D visualization of FFA W3-301 airfoil without (left) and with (right) VGs

The baseplate shape no.4 and 5 show good agreement with the simulation result on a clean airfoil. Baseplate shape no.1 shows good agreement with the experimental drag results for the angle of attack between 0 to 4 degrees.

From this study, it can be concluded that the airfoil section with baseplate would have lower lift and higher drag force in comparison with the clean airfoil section. The smoothest shape would be the baseplate shape no. 4 and 5, which have the lowest drag among other shapes. The beveled baseplate shape has an influence on flow separation.

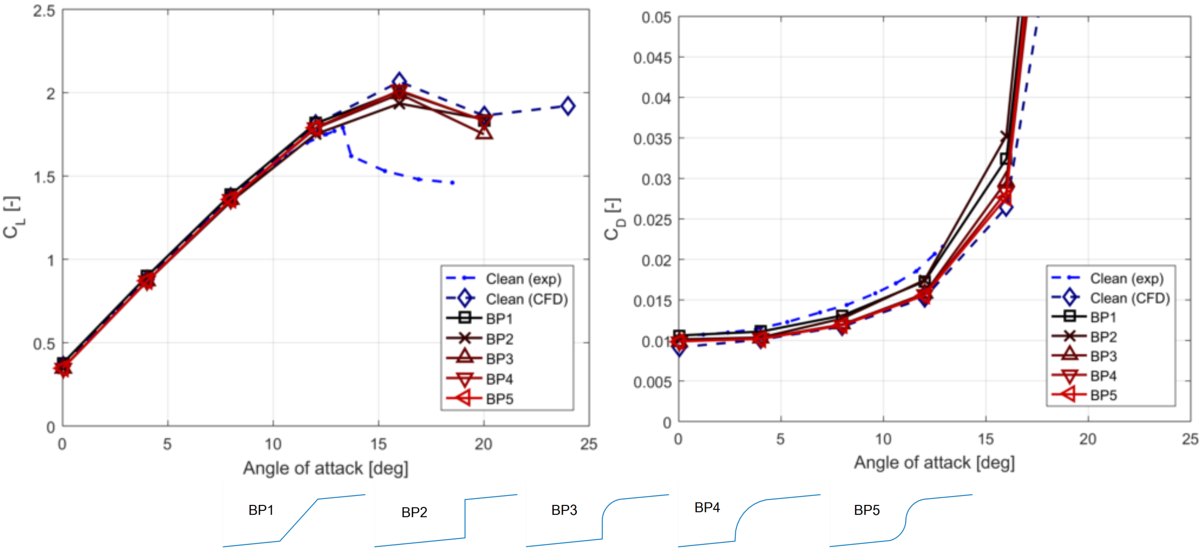

Figure 4.7: Comparison of lift and drag coefficient curves with different baseplate shapes at different angle of attacks

4.1.3.3 VGs & Baseplate

The airfoil with VGs and baseplate are simulated. Figure 4.8 shows the airfoil with various baseplate shapes with VGs. It is seen that the bevel of the baseplate causes a variation on the lift curves. Baseplate shape no.5 has the highest lift compared with the other baseplate shapes, and is congruent with the results from the simulated airfoil with VGs and without baseplate. The baseplate shape no.2 has the highest lift and the separation occurs at between 14 and 16 degrees. Baseplate shapes no. 3 also shows early separation at between 18 and 20 degrees. Baseplate shape no.1 and 4 shows very similar behavior over the lift curve. Flow in both cases is separated at between 20 and 22 degrees. From the lift curve it is obvious that the baseplate shapes have strong influence to the flow separation behavior of FFA

W3-301 airfoil. The worst case is found on the airfoil with baseplate shape no.2, which separated earlier than the clean airfoil.

The drag coefficient of the airfoil with baseplate and VGs can be seen on the right hand-side of figure 4.8. It is seen that drag coefficients at low angle of attack of the airfoil with VGs & baseplates are underpredicted comparison with the experimental results of the airfoil with VGs. The drag coefficient of the airfoil with VGs & baseplate shape no. 1 and 3 are lower than the simulation results of the airfoil with VGs in the range between 4 and 12 degrees. The drag force of the baseplate shape no.4 and 5 are slightly higher than all simulation results in the range between 0 and 12 degrees and then the drag coefficient of baseplate shape no.4 sees a jump due to flow separation at around 20 degrees. The drag coefficient of the airfoil with baseplate shape no.5 suddenly increases at around 24 degrees, similar to the simulated airfoil with only VGs. The baseplate shape no.2 shows a sudden increase in drag coefficient at around 14 degrees due to flow separation.

In conclusion, it seen that all simulation drag coefficient results underpredicted the drag coefficient in the experiment of the airfoil with VGs. Lift and drag curves of the airfoil with VGs and baseplate shape no.5 are congruent with the simulation results from the airfoil with only VGs.

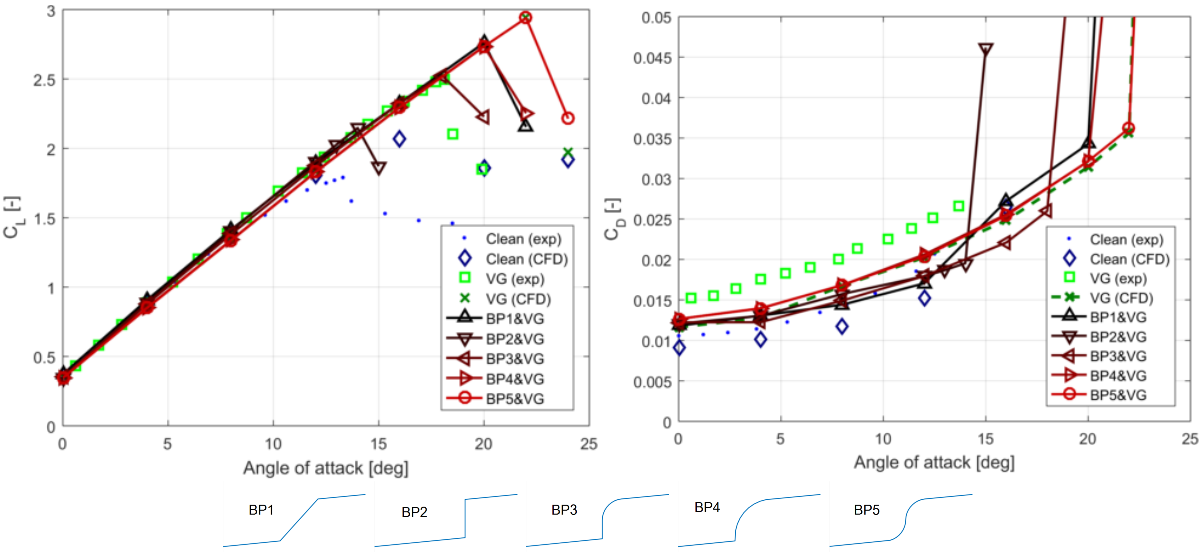

Figure 4.8: Comparison of lift and drag coefficient curves for the FFA-W3-301 aerofoil with VGs and different baseplate shapes at different angle of attacks

4.1.4 VGs' Position

Various VGs' postions are studied. The VGs are located at 0.20c, 0.25c and 0.30c. Figure 4.9 shows lift and drag polar of FFA W3-301 airfoil with VGs at various positions. From the figure, it could be seen from the lift curve that the simulation results for the airfoil with various VGs' positions show a good agreement to the experimental results for the angle of attack between 0 and 16 degrees. By moving VGs toward the airfoil leading edge, a higher maximum lift is reached. This effect can be observed from both experimental and numerical results. This means that the flow separation is delayed as the VGs are moving toward the leading edge.

The drag coefficient is shown in figure 4.9. There is no difference between the simulation of the airfoil with VGs for drag coefficients in the range between 0 and 8 degrees. Similar trend is also noticed from the experimental results of the airfoil with VGs at 0.25c and 0.30c. Both results are good agreement between 0 and 2 degrees. For higher angle of attack, it is seen that the airfoil with VGs at 0.25c has slightly higher drag. The simulation results shows that, the drag coefficient, for the airfoil with VGs at 0.20c at angle of attack greater than 10 degrees, steadily increases and is the highest among the simulation results. The drag coefficient for the airfoil with VGs at 0.25c is slightly less than the one at 0.20c at the angle of attack greater than 10 degrees before a jump. The drag coefficient for the airfoil with VGs at 0.30c has the lowest drag among other VGs' configuration but it sees early jump at around 20 degrees.

This can be conclude that moving the VGs toward the leading edge could delay flow separation but also increase drag coefficient at high angle of attack. A possible explanation is that at high angle of attack, the VGs closer to the leading edge are effectively injecting momentum into the flow. This momentum on one hand delays flow separation but on the other hand also increases the parasitic drag as seen on the right hand side of figure 4.10. From figure 4.10 (a), it is seen that the pressure distribution are remained the same as the VGs are moving toward the leading edge. After the stagnation point, the friction coefficient for the airfoil with VGs (0.20c) at 4 degrees sees an early jump at around 0.20c, whereas it suddenly increases at around 0.25c for other airfoil configurations. Although, the curves in this figure seem to be difference, the drag coefficients are in good agreement at this angle of attack. At angle attack of 16, the pressure distribution still remains the same for all airfoil with VGs configurations as seen in 4.10 (b). The friction coefficients for all configuration rise after the stagnation point at around 0.10c. After that, the airfoil with VGs at 0.20c has the highest friction coefficient followed by VGs at 0.25c and 0.30c respectively. All curves are congruent at around 0.45c. This indicates that the airfoil with VGs at 0.20c has the highest friction coefficient or parasitic drag.

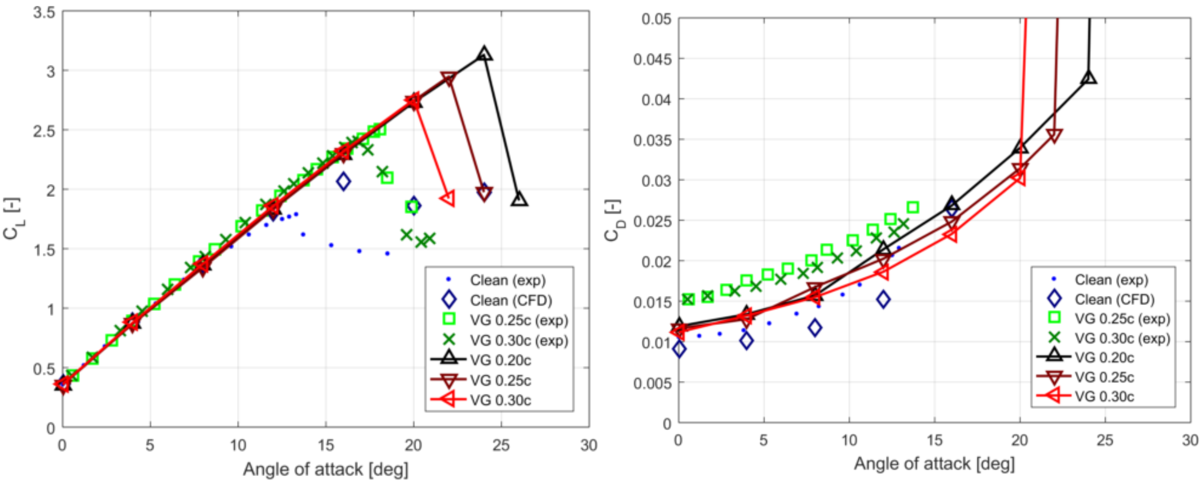

Figure 4.9: Comparison of lift and drag coefficient curves for the FFA-W3-301 airfoil with VGs at different VGs' position

4.1.5 Reynolds Number Study

The Reynolds number study is performed on FFA W3-301 airfoil. The airfoil with the Reynolds number of 5×10^6 and 8×10^6 are simulated. The baseplate shape no. 1 and 2 and 5 are investigated in this study. Baseplate shape no.1 is selected, as it is the simplest shape and practically used. Baseplate shape no.2 is selected as it shows the worst performance in previous studies. On the other hands, baseplate shape no.5 is selected as it shows the best performance.

4.1.5.1 Only VGs

Figure 4.11 shows lift and drag coefficients of the FFA W3-301 airfoil with VGs at difference Reynolds numbers. The clean airfoil with higher Reynolds number is seen to have slightly higher maximum lift (approximately 2.5%) and less drag coefficients (approximately 8%) compared with the experimental

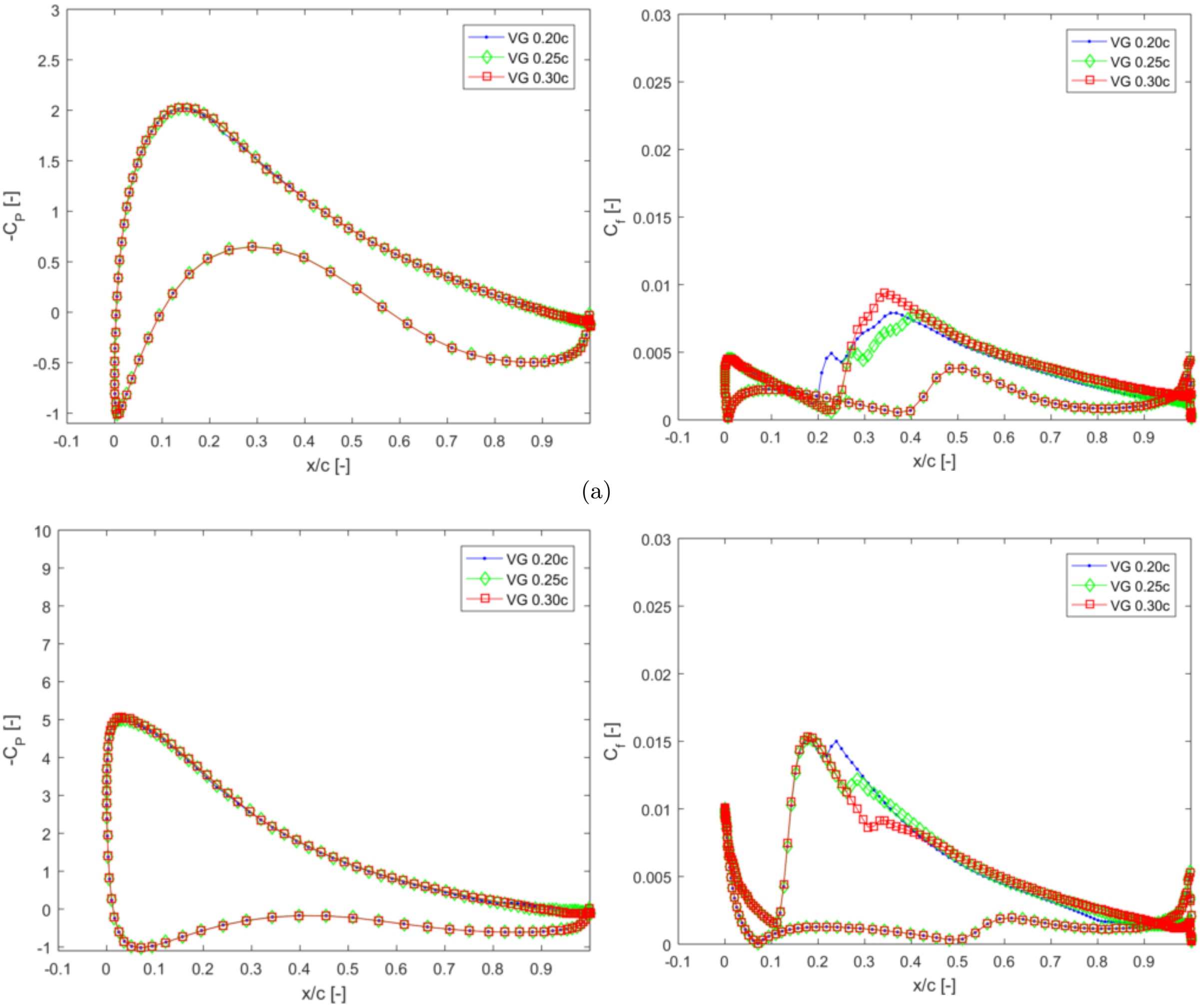

(a)

(b)

Figure 4.10: Comparison of pressure and friction coefficients for the FFA-W3-301 airfoil with VGs at different VGs' positions a) 4 degrees b) 16 degrees

results. The airfoil with VGs with Reynolds number of 5×10^6 and 8×10^6 separates between 22 and 24 degrees. The maximum lift coefficient of both airfoil with VGs at different Reynolds numbers are the same. The drag curve of the airfoil with VGs at Reynolds number of 8×10^6 is slightly less than the other one by approximately 5%.

4.1.5.2 VGs' Baseplate

The airfoil with baseplate shape no.1, 2 and 5 are simulated at difference Reynolds numbers as seen in figure 4.12 . The airfoil with baseplate shape no.2 at the Reynolds number of 5×10^6 has the lowest lift curve when compared with other cases. However, as the Reynolds number increases, the airfoil with baseplates are congruent. The airfoil with baseplate shows lower maximum lift compared to the clean airfoil.

The drag coefficient curve of the clean airfoil at Reynolds number of 8×10^6 is the lowest. The drag coefficient curve for the airfoil with baseplate shape no.2 at Reynolds number of 5×10^6 is the highest. The drag curve is shifted down with an increase of the Reynolds number. Similarly, the airfoil with

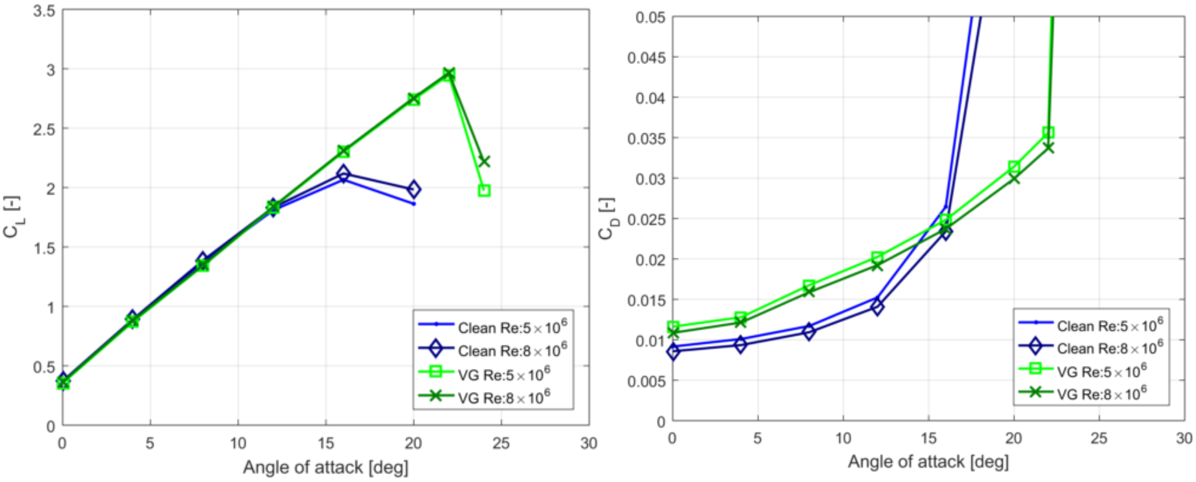

Figure 4.11: Comparison of lift and drag coefficient curves of the FFA W3-301 airfoil at different Reynolds numbers

baseplate shape no.1 and 5 at Reynolds number of 8×10^6 show lower drag coefficients than the one at Reynolds number of 5×10^6. The airfoil with baseplate shape no.5 at Reynolds number of 8×10^6 has the lowest drag curve among other baseplate configurations and is congruent with the clean airfoil at the same Reynolds number.

This can be concluded that as the Reynolds number increase, lift coefficient increases and drag coefficient decreases.

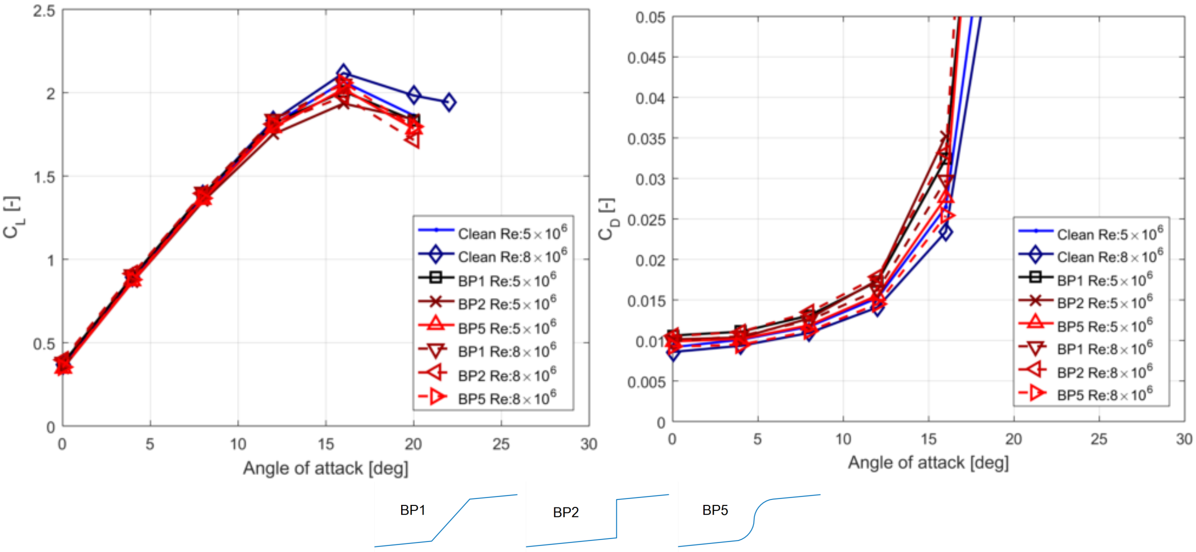

Figure 4.12: Comparison of lift and drag coefficient curves of the FFA W3-301 airfoil with baseplate at different Reynolds numbers

4.1.5.3 VGs & Baseplate

The airfoil with baseplate and VGs at difference Reynolds numbers are simulated and shown in figure 4.13. For Reynolds number of 5×10^6, the airfoil with baseplate shape no.2 shows a drop in lift coefficient at around 14 to 15 degrees. Other airfoil with baseplate shapes show separation between 20 and 22 degrees. The increase of the Reynolds number result in a better flow separation control for the airfoil with baseplate shape no.2. At Reynolds number of 8×10^6, the maximum lift coefficient of the airfoil with baseplate shape no.2 increases from around 14 degrees at Reynolds number of 5×10^6 to around 20 degrees at Reynolds number of 8×10^6. The maximum lift for the airfoil with baseplate shape no.5 is decreased from around 22 degrees to 20 degrees at higher Reynolds number. This could be as a result of higher parasitic drag. The lift curve of the airfoil with baseplate shape no.1 has no significance changed.

From figure 4.13, the drag coefficient curve of the clean airfoil at Reynolds number of 8×10^6 is the lowest. The drag coefficient of the airfoil with VGs at Reynolds number of 8×10^6 is slightly less than the one at higher Reynolds number. The airfoil with baseplate shape no.2 at Reynolds number of 8×10^6 has the highest drag curve. It is seen that for the same baseplate shape as the Reynolds number increases, drag coefficient rises.

The increase of the Reynolds number results in better flow separation control as seen in the airfoil with baseplate shape no.2 where the stall angle is delayed from around 14 degrees to 20 degrees. However, there is a drag penalty at higher Reynolds number due to the increase of the parasitic drag.

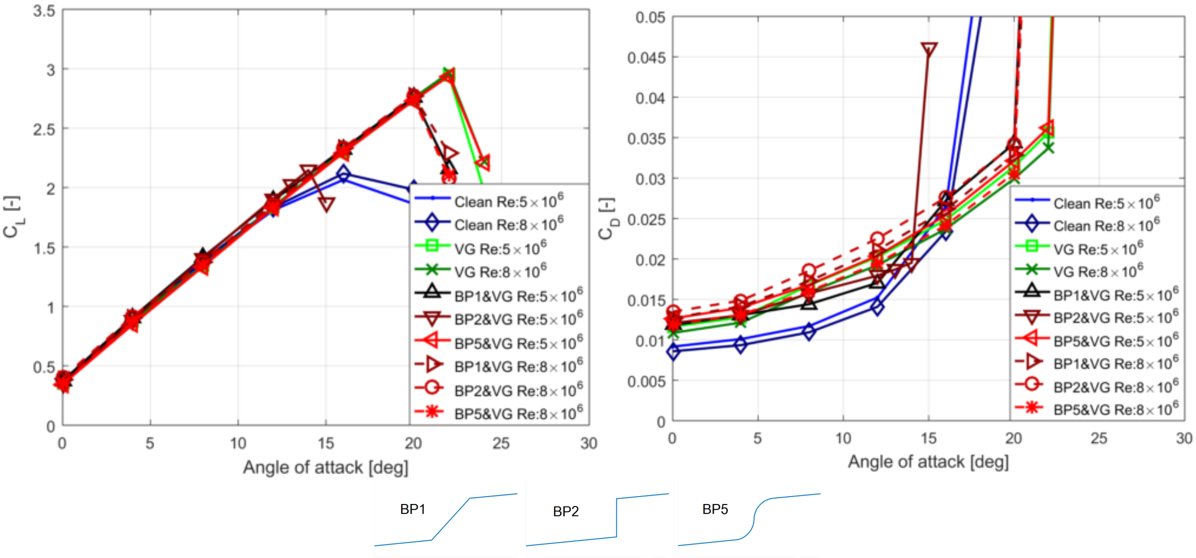

Figure 4.13: Comparison of lift and drag coefficient curves of the FFA W3-301 airfoil at different Reynolds numbers

4.1.6 Baseplate's Height Study

Baseplate's height study is performed. The baseplate height of $0.667c\times10^{-3}$ and $1.000c\times10^{-3}$ are investigated. The baseplate shape no.1, 2 and 5 are simulated in this study. The VGs are located at 0.25c.

4.1.6.1 Only VGs' Baseplate

From figure 4.14, it is seen that the airfoil with the baseplate's height of $0.667c\times10^{-3}$ has higher maximum lift coefficient compared with thicker baseplate configurations. The baseplate shape no.5 with the height of $1.000c\times10^{-3}$ shows the lowest maximum lift coefficient among other baseplate configuration. For the baseplate height of $1.000c\times10^{-3}$, the baseplate shape no.1 has the highest maximum lift, whereas the baseplate shape no.5 has the lowest maximum lift. In comparison as the height of the baseplate increases the maximum lift reduces by approximately 3%, 7% and 13% for baseplate shape no. 1 2 and 5 respectively. The baseplate shape no.5 has shown an early flow separation at the angle of attack between 12 and 16 degrees, whereas other airfoil configurations stall at around 16 degrees.

In the same figure, it is seen that the drag coefficient slightly increases as the baseplate's is elevated. The airfoil with baseplate shape no.1 with the height of $1.000c\times10^{-3}$ has the highest drag coefficients compared with other baseplate configurations. Besides, it has higher drag coefficients than the experimental results from clean airfoil in the range between 0 to 4 degrees. The baseplate shape no.5 with the height of $0.667c\times10^{-3}$ has the lowest drag coefficients. At the angle of attack between 0 and 8 degrees, the amount of drag for each baseplate configurations increases as the height increases by approximately 3%, 5% and 0.2% for baseplate shape no. 1, 2 and 5 respectively.

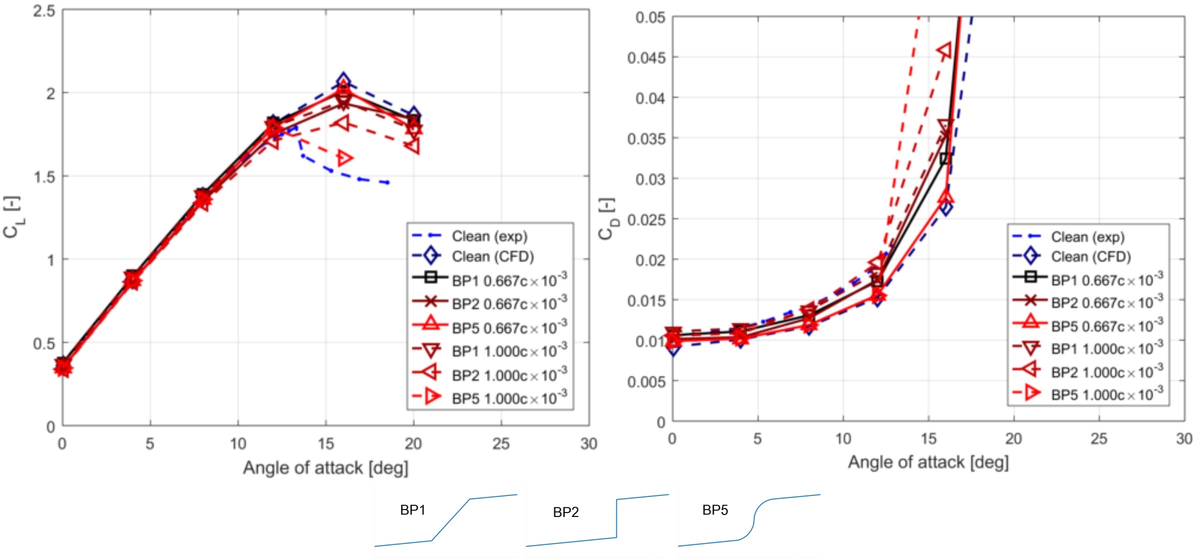

Figure 4.14: Comparison of lift and drag coefficient curves of the FFA W3-301 airfoil with different baseplate heights

4.1.6.2 VGs & Baseplate

From figure 4.15, the lift curves are congruent at the angle of attack between 0 and 12 degrees. It is seen that although the baseplate's height increases, the lift results for each baseplate configurations remain the same until the stall angle of attack. Both airfoil with baseplate shape no.5 with the height of $0.667c\times10^{-3}$ and $1.000c\times10^{-3}$ are congruent to each others and also in good agreement with the one without baseplate.

On the right hand-side of the figure 4.15 illustrates drag coefficients curve of the FFA W3-301 airfoil with VGs at difference baseplate heights. It is seen that as the height of the baseplate increases, the drag coefficients also rise. The amount of drag increase is vary accordingly to the baseplate configurations. For the airfoil with baseplate shape no.1, 2 and 5 at the angle of attack between 0 and 8 degrees, the amount of drag increases by approximately 14%, 5% and 5% respectively. All drag coefficient curves are still under-predict the experimental results of the airfoil with only VGs. The airfoil with the baseplate shape no.1 with the height of $1.000c\times10^{-3}$ has the highest drag coefficients in the range of 0 to 12 degrees. It has the closest curve to the experimental results.

It can be concluded that the increase of the baseplate height yield to higher drag coefficient. The amount of drag increase depends on the baseplate configurations. The airfoil with VGs & baseplate shape no.5 shows the least drag magnitude, when its height increases. There is no effect of the baseplate height to the lift coefficients in the airfoil with VGs cases, whereas the maximum lift coefficient reduces as the height increases in the airfoil without VGs cases.

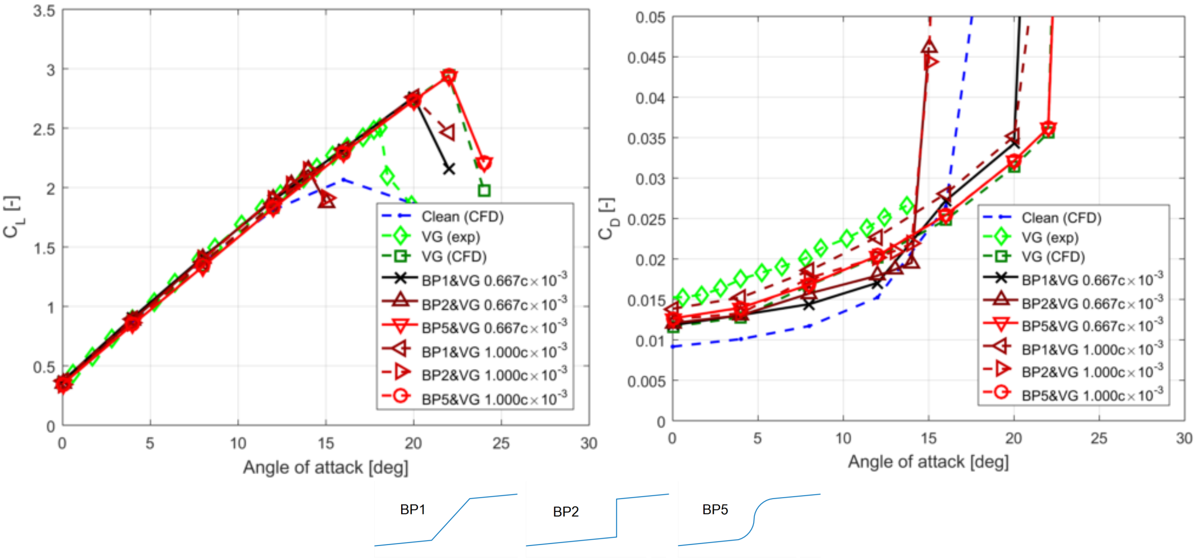

Figure 4.15: Comparison of lift and drag coefficient curves of the FFA W3-301 airfoil with VGs at different baseplate heights

4.1.7 Roughness Study

Roughness sensitivity on FFA W3-301 airfoil is studied. The airfoil is covered by the equivalent sand roughness from its leading-edge to 0.08c as same as in the experiment done on NACA airfoil by Abbott [1]. For the roughness study, the transition model is not applicable as the sand roughness has already tripped the flow at the leading-edge. Three roughness cases are studied in this section as detailed in table 4.3.

Cases	k_s/c [-]
Hydraulically Smooth 1	0.004×10^{-3}
Hydraulically Smooth 2	0.02745×10^{-3}
Roughness	0.549×10^{-3}

Table 4.3: Roughness study set-up

The airfoil with roughness on the leading-edge has the lowest curve in figure 4.16 and has an early separation (around 8 degrees). The maximum lift coefficient reduces from approximately 2 in simulated results of clean airfoil to around 1.1. The rough and clean airfoil lift curves exhibit similar slopes in the range of the angle of attack of 0 to 4 degrees. The rough airfoil lift curve shifts downward due to the lack of the transition model. This caused the flow to turn into fully turbulent from laminar without transition. The flow in the rough airfoil is tripped at the leading-edge, as a consequence the boundary layer is turbulent. The clean airfoil simulation without transition model (fully turbulent ($k-\omega$ SST turbulence model) and hydraulically smooth condition (roughness model) are also simulated. From figure 4.16, it could be seen that the roughness model with hydraulically smooth 2 configurations has lower maximum lift coefficient (approximately 4%) compared with the fully turbulent model. Besides, it also has slightly higher drag coefficient around 4%. The results from the fully turbulent model and hydraulically smooth 1 are congruent with each other.

The drag coefficient of the airfoil with roughness, illustrates on the right hand-side of figure 4.16. The rough airfoil is seen to be the highest among the cases. The drag coefficient of the rough airfoil exponentially increases. By analyzing the drag coefficient curve, it could be noticed that flow separation likely occurs at around 8 degrees in the rough airfoil case. The airfoil simulation without transition model and hydraulically smooth showed exactly the same drag coefficients results and lower than the rough airfoil case. A jump is seen at around 12 degrees in both cases.

From this study it is seen that the airfoil with roughness has a dramatic loss in lift. This could mean that FFA W3-301 airfoil is quite sensitive to the roughness.

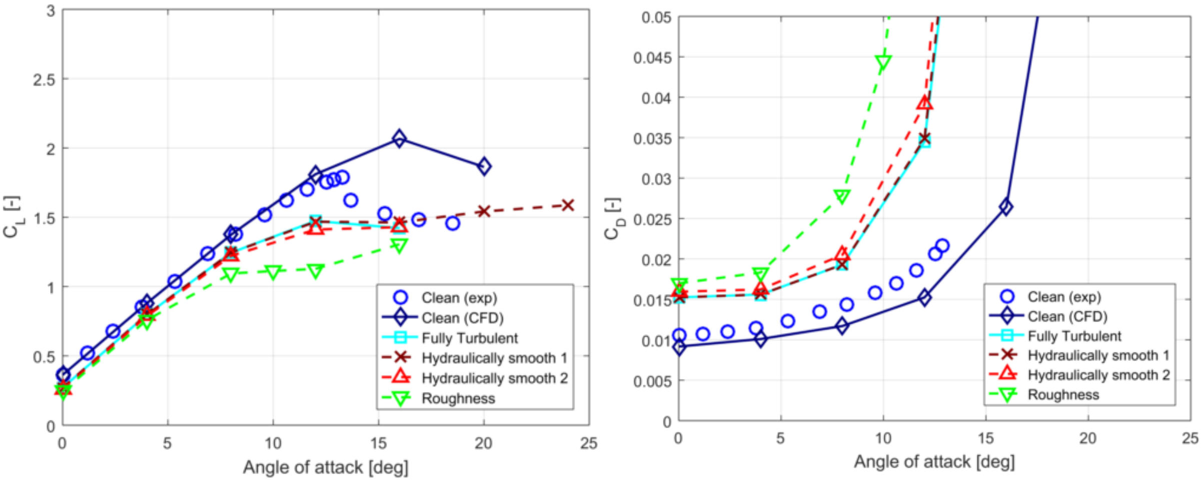

Figure 4.16: Comparison of lift and drag coefficient curves of the FFA-W3-301 airfoil with different surface treatments

4.1.7.1 VGs' Position

It is seen that by adding VGs on the clean airfoil, flow separation is delayed as seen in figure 4.4. Similar effects could be done by adding VGs on a rough airfoil. The flow separation of the airfoil with surface roughness is improved as seen in 4.17. VGs show that they could restore a loss in lift due to the presence of roughness on the airfoil. Besides, the rough airfoil with VGs has a higher maximum lift and a higher stall angle of attack than the rough airfoil without VGs. The maximum lift of the airfoil with roughness and VGs at 0.30c is approximately 1.8 at the angle of attack of 14 degrees, which is around 62% increase compared with the rough airfoil case at 8 degrees with the maximum lift coefficient of approximately 1.1.

VGs positions could also affect the flow separation on the rough airfoil as well as on the clean airfoil in the previous study. By moving VGs toward the leading edge, flow separation is delayed similar to what is seen on the clean airfoil in figure 4.9. Moving VGs further toward the leading edge (<0.25c), could not further improve flow separation better than VGs at 0.25c. This could be a consequence of the VGs location being close to the separated boundary layer from the rough surface. The boundary layer separation from the rough surface has been effectively controlled with VGs at 0.25c. At angle of attack of around 16-17 degrees, both VGs location at 0.25c and 0.20c are separated due to the large flow separation due to the airfoil incidence and rough leading-edge.

4.1.7.2 VGs' Baseplate

From the previous section, the airfoil with VGs has shown to improve the rough blade performance. It is expected that airfoil with baseplate and roughness could also be improved with VGs as well. In this study, the airfoil with roughness, baseplates and VGs at 0.25c are investigated.

Figure 4.18 shows the lift and drag curves for the airfoil with roughness, baseplates and VGs at 0.25c. Rough airfoil with VGs and baseplate shape no. 1, 3, 4 and 5 show similar lift curves. They exhibit flow separation around 16-20 degrees, whereas the baseplate shape no.2 shows early separation between 12 to 16 degrees. Baseplate shape no.1 and 3 show slightly higher maximum lift compared to

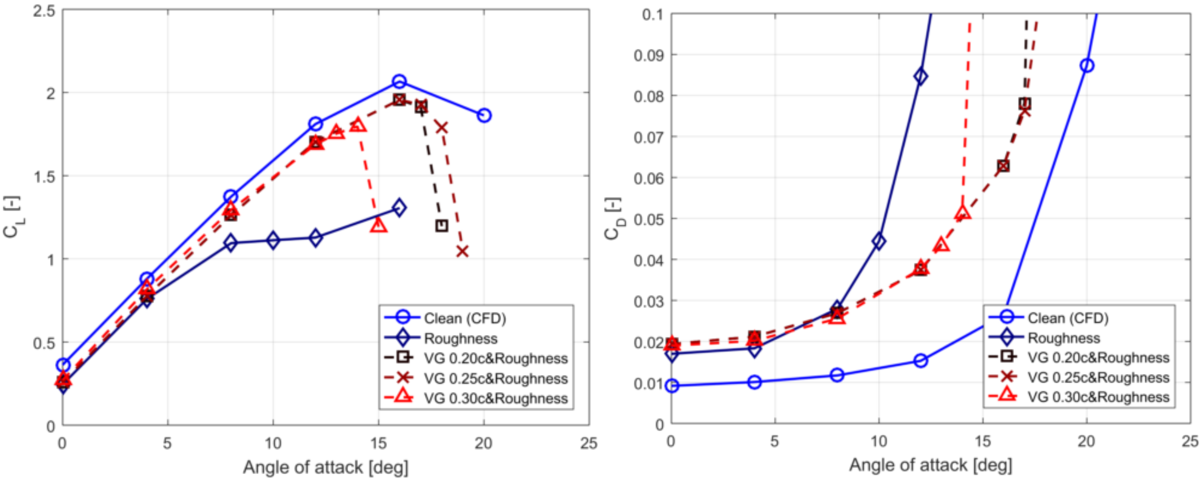

Figure 4.17: Comparison of lift and drag coefficient curves of the FFA-W3-301 airfoil with different surface treatments and VGs' position

other baseplate shapes and the airfoil with VGs without baseplate. This variation is very small and could be a consequence of the stall cell, which could be larger than the span. In order to improve these results, one could use a larger span or at least one with the same size as the chord.

The drag coefficient is shown on the right hand-side of the figure 4.18. For the airfoil with roughness, drag coefficients are higher than the clean airfoil. A good agreement between all baseplate shapes and rough airfoil with VGs could be found in the range of 0 to 12 degrees. The drag coefficient of the most of the rough airfoil cases are jumped at around 16 degrees due to flow separation. However, for the baseplate shape no.2, the separation occurs earlier between 12 to 16 degrees.

Baseplate shape no.2 has strongly affected to the lift and drag forces on the rough airfoil with VGs. With baseplate shape no. 1, 3, 4 and 5, flow separation could be controlled as well as in the clean airfoil case. The lift loss in rough airfoil is improved by installing VGs, however it cannot gain a better performance than the clean airfoil case.

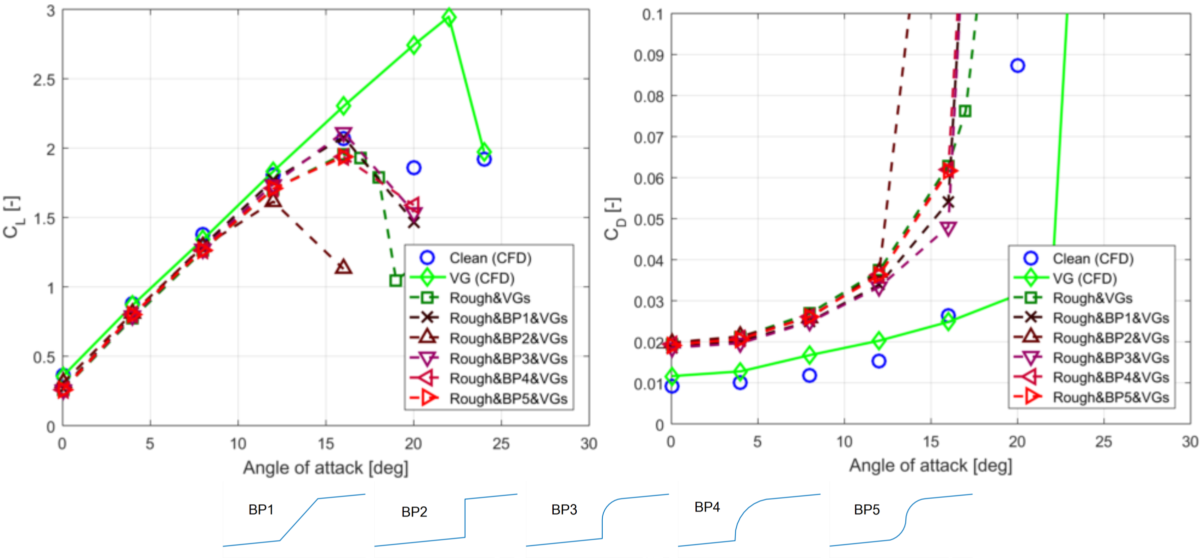

Figure 4.18: Comparison of lift and drag coefficient curves of the FFA-W3-301 airfoil with surface roughness for different baseplate shape

4.1.7.3 Annual Energy Production (AEP)

Further study is done using a wind turbine from 46300 Wind Turbine Technology and Aerodynamics course at DTU Lyngby (Appendix C). The blade has the same airfoil profile over its entire span. In the case study of the airfoil with VGs, VGs are installed up to 40% of the blade span (inboard part).

Figure 4.19 illustrates the power production from the reference wind turbine with the airfoil with different surface treatments. The power curve of the clean airfoil is the highest at wind speed between 5 to 10 m/s. The power curve for the rough airfoil with different VGs positions are very similar to each other. The blade with surface roughness shows the least power production and yields the least AEP as seen in table 4.4. The annual energy production reduces from around 10.2 GWhr for clean blade to around 8.36 GWhr (reduces by approximately 18%) for the blade with surface roughness. The annual energy production is regained by approximately 10% compared to the clean airfoil when VGs are attached on the inboard part (<0.40 span) of the blade. The maximum annual energy production of 9.41 GWhr is found when the VGs are installed at 0.20c. However, placing the VGs at 0.20c result in a higher thrust from around 0.2 to 1.5 % when compared to placing the VGs at other positions.

The thrust curves are shown on the right hand-side of figure 4.19. An increase in thrust by approximately 3% is found on the rough blade. Annual energy production is increased by installing VGs, however, this would lead to higher thrust as well. The maximum thrusts of the blade with roughness and VGs (at 0.20c, 0.25c and 0.30c) are approximately 0.258, 0.257 and 0.255 MN respectively. The wind turbine blade with VGs at 0.20c has a higher maximum thrust compared to the clean blade by around 4.24%. The lowest maximum thrust is found when VGs are installed further away from the leading edge (0.30c) with the value of 0.255 MN or approximately 2.72 % difference compared to the clean blade.

This study has shown that by installing VGs on the existing contaminated wind turbine blade, the energy production could be increased, however with the cost of increasing thrust on the blade. This additional thrust might in turn contribute to more severe fatigue loads on the blades. For the rough blade, the blade with VGs could boost the annual energy production by approximately 10%. This means that wind turbine blades with VGs installed could potentially be very beneficial for wind turbines operating in harsh environments.

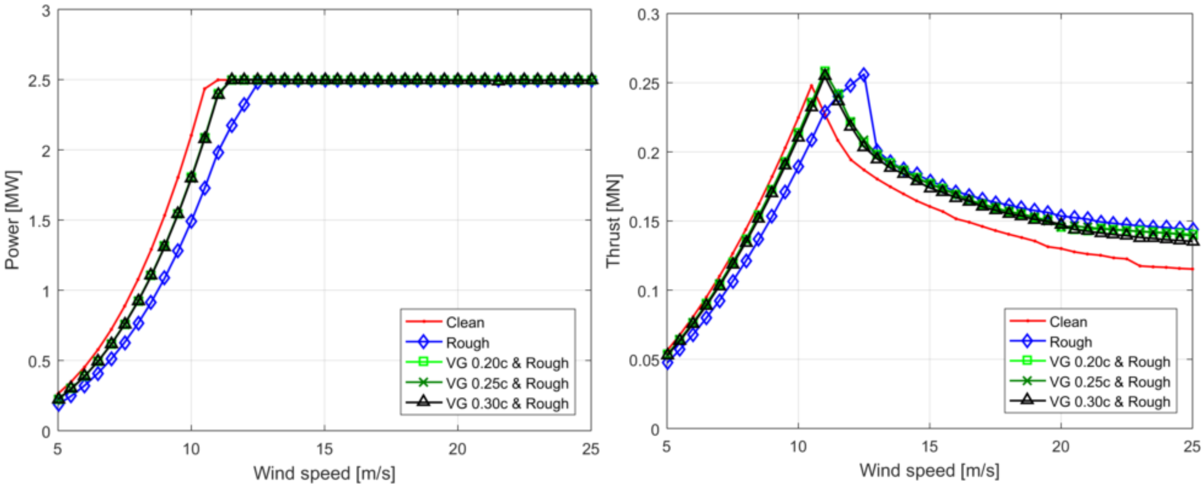

Figure 4.19: Comparison of power [MW] and thrust [MN] of the FFA W3-301 airfoil with roughness at different VGs' position

The effect of the baseplate on the rough airfoil with VGs is studied and is shown in figure 4.20. From figure 4.20, clean airfoil has the highest annual energy production. The effect of the baseplate on the rough airfoil with VGs could not be clearly seen from the power curve. After calculating the annual energy production, the best performance was found to be from the rough airfoil with VGs and baseplate shape no.1 follow by no. 3 , 5, 4 and 2. The difference in energy production for baseplate shape no. 1 , 3, 5 and 4 are very small and with a difference of about 0.5% in magnitude.

The highest energy production also yield to the highest maximum thrust, which can be found on the baseplate shape no.1. In comparison, baseplate shape no. 3, 4 and 5 have a lower maximum thrust. The least maximum thrust was found on the rough airfoil with baseplate shape no.2.

Baseplate shape no.1 seems to produce the highest annual energy, however it also has the highest maximum thrust. The rough airfoil with baseplates and VGs seem to perform better than the one without baseplate. This could be a result of inaccuracies in flow separation prediction, which is referred as a classical issue of flow simulation [37]. Besides, resolution in the results (4 degrees) might be too low, hence accurate annual energy production and thrust calculations are not achievable.

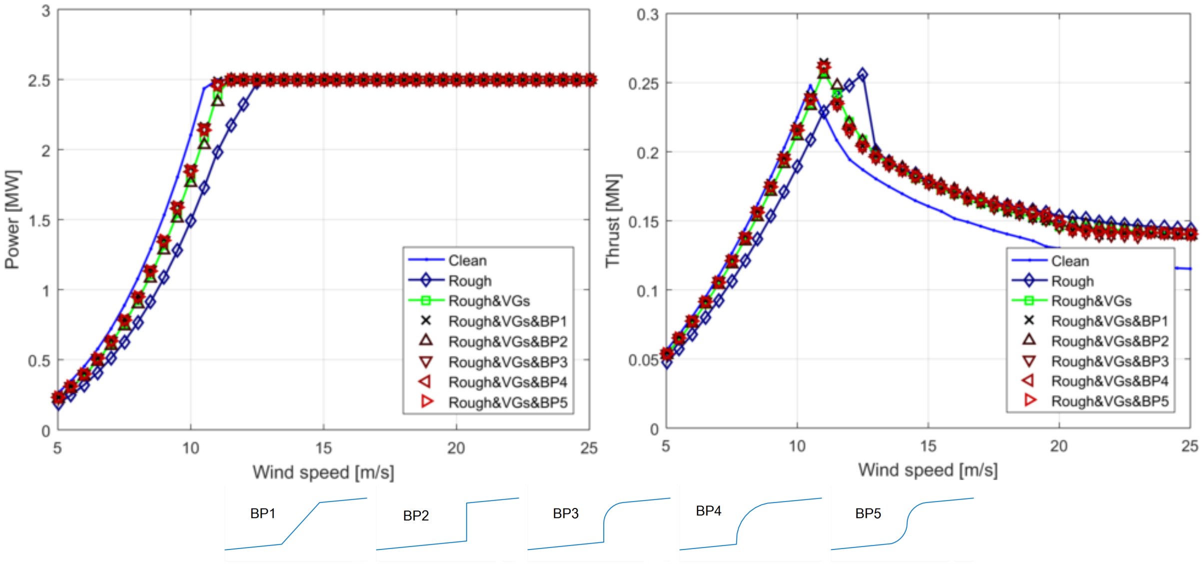

Figure 4.20: Comparison of power [MW] and thrust [MN] of the FFA W3-301 airfoil with different baseplate shapes

Cases	$AEP[GWhr]$	%Difference	Max. Thrust [MN]	%Difference
Clean	10.20	-	0.248	-
Rough	8.36	-18.05	0.256	3.32
Rough & VGs 0.20c& Roughness	9.41	-7.76	0.258	4.24
Rough & VGs 0.25c& Roughness	9.40	-7.86	0.257	3.98
Rough & VGs 0.30c& Roughness	9.39	-7.96	0.255	2.72
Rough & VGs & BP1& Roughness	9.60	-5.88	0.264	6.68
Rough & VGs & BP2& Roughness	9.28	-9.02	0.256	3.13
Rough & VGs & BP3& Roughness	9.57	-6.14	0.262	5.84
Rough & VGs & BP4& Roughness	9.53	-6.55	0.261	5.27
Rough & VGs & BP5& Roughness	9.54	-6.46	0.261	5.32

Table 4.4: Wind turbine annual energy production (AEP) [GWhr] and Max. Thrust [MN]

4.1.8 Pressure & Friction

In order to understand the flow separation by analyzing pressure plots, the following study is performed. Consider the airfoil moving through a fluid at a low angle of incidence. The flow will stagnate at the leading edge of the airfoil. The pressure reaches a peak at this position. This pressure is the highest as seen in figure 4.21.

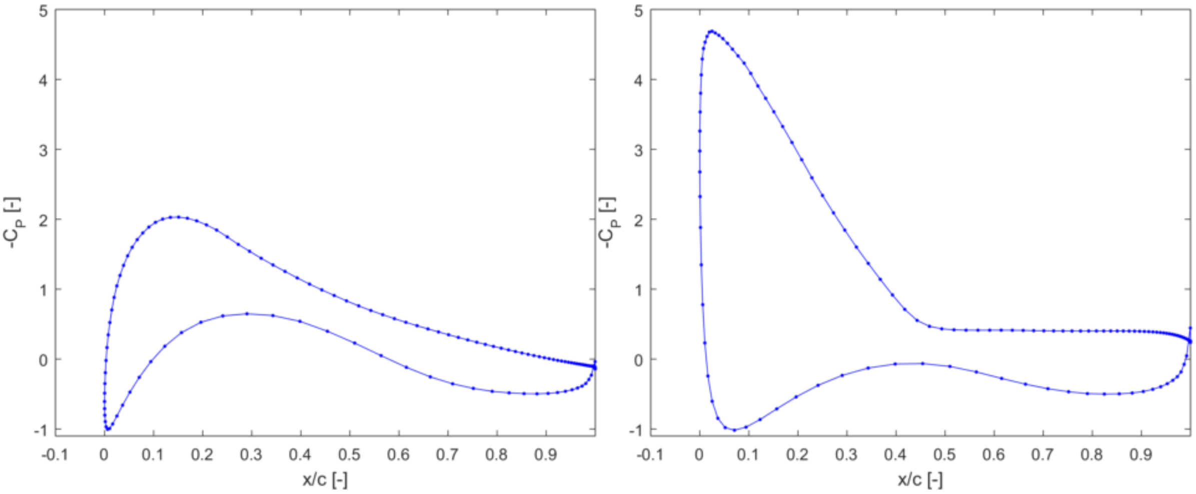

(a) (b)

Figure 4.21: Pressure coefficient curves of the FFA W3-301 airfoil with an angle of attack of a) 4 and b) 20 degrees

Figure 4.21 illustrates the pressure distribution over FFA W3-301 airfoil when it moves through the fluid with an angle of attack of 4 degrees (a) and 20 degrees (b). After the stagnation point, the pressure rapidly sinks to a minimum. The pressure gradient in this region is negative and is also known as favorable pressure gradient. The pressure then increases as the flow moves towards the trailing edge. The pressure gradient is positive in this region (adverse pressure gradient). The adverse pressure gradient in sub-figure (a) is small compared to the one in sub-figure (b). The adverse pressure gradient causes the flow to reverse and the flow is eventually separated around 0.4 x/c in sub-figure (b). The flow separation causes an abrupt loss of lift and dramatic increase in drag (pressure drag).

Figure 4.22 shows the pressure coefficient curve of the FFA W3-301 airfoil. The VGs are installed at 0.25 x/c in this case. It can be observes from this pressure plot, that after the stagnation point the pressure sank to the minimum point as the flow accelerates over the airfoil leading edge. After that, the pressure expands with a positive gradient (adverse pressure gradient). If the adverse pressure gradient is high enough, the force then pushes the flow backwards and results in a flow separation.

It is seen that the pressure plots for clean and VGs (0.25c) airfoil are identical in the range of angle of attack between 0 and 12 degrees. This shows that the VGs have no effect on the force over the airfoil in that range. However, for higher angle of attacks, the airfoil with baseplate&VGs and VGs have a lower minimum pressure than in the clean airfoil case. This could mean that the VGs enhances the lift and drag forces exerted on the airfoil.

By taking the baseplate into consideration, a sudden jump in pressure plot could be observed at the baseplate's location. Without VGs, the airfoil with baseplate has a lower lift than other cases. With VGs installed, the lift improves and is seen to be higher than the clean airfoil case.

The flow separation can be roughly predicted from the pressure plot, where the gradient is infinite. From figure 4.22 (e), the separation can be occurred around 0.5 x/c for airfoil with baseplate as the gradient is very high in this region. Similar phenomena can also be observed in sub-figure (f), the separation moves forward to 0.3 x/c for airfoil with baseplate case.

Figure 4.23 shows the friction coefficient curves of the FFA W3-301 airfoil. The airfoil with baseplate has a jump at the baseplate location. From sub-figure (d), (e), and (f) the friction force jumps ahead of the VGs location. This jump could be as a result of highly adverse pressure gradient, which contributes to the pressure drag. This means that, the separation occurs in front of the VGs at high angle of attack. This separation is however delayed by adding the VGs.

For the airfoil with rough surface at the leading edge, it can be seen in the friction coefficient curve in figure 4.23, there is a huge jump where the surface is rough.

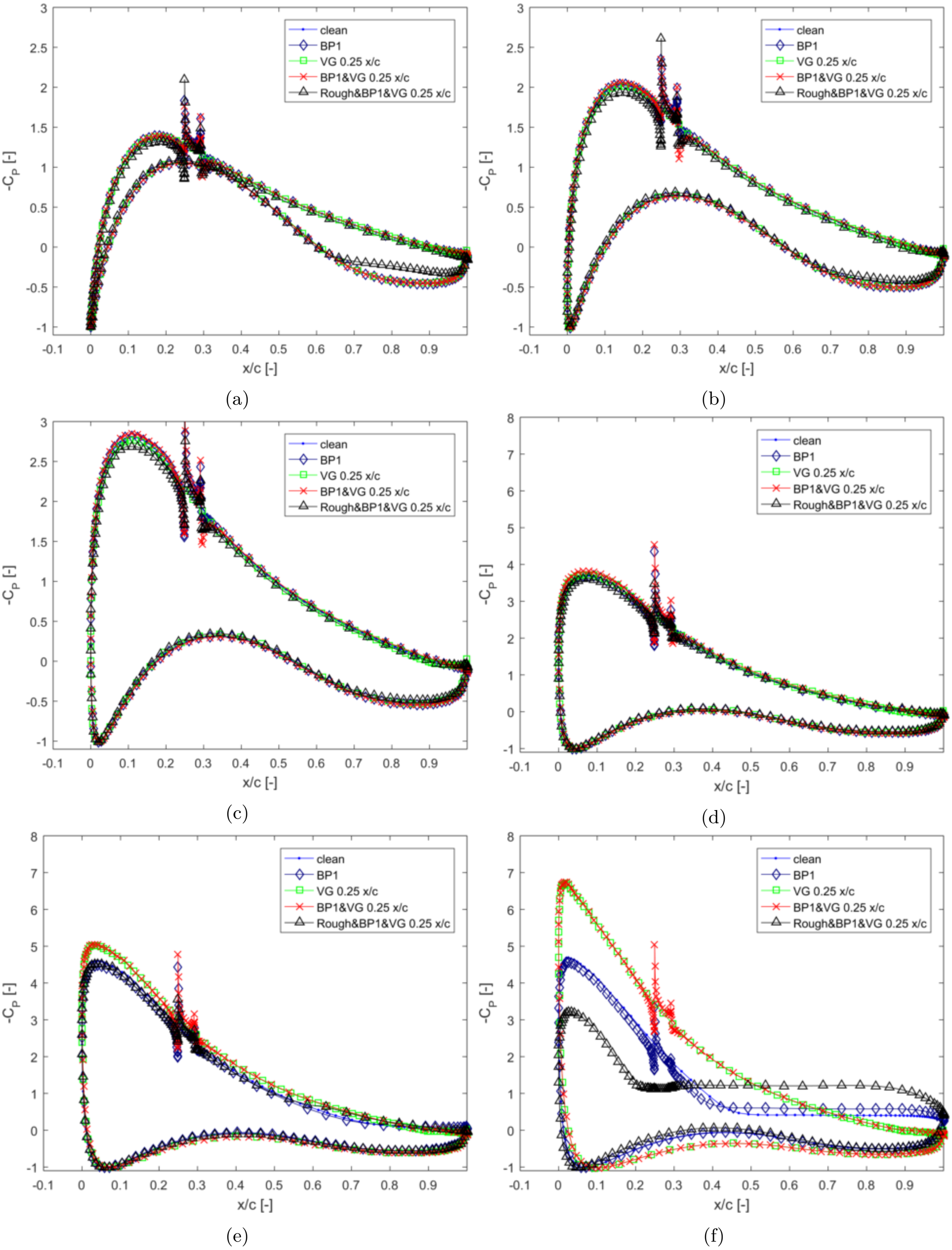
(a) (b) (c) (d) (e) (f)

Figure 4.22: Pressure coefficient curves for the FFA-W3-301 airfoil at AoA of a) 0 , b) 4, c) 8, d) 12, e) 16, f) 20 degrees

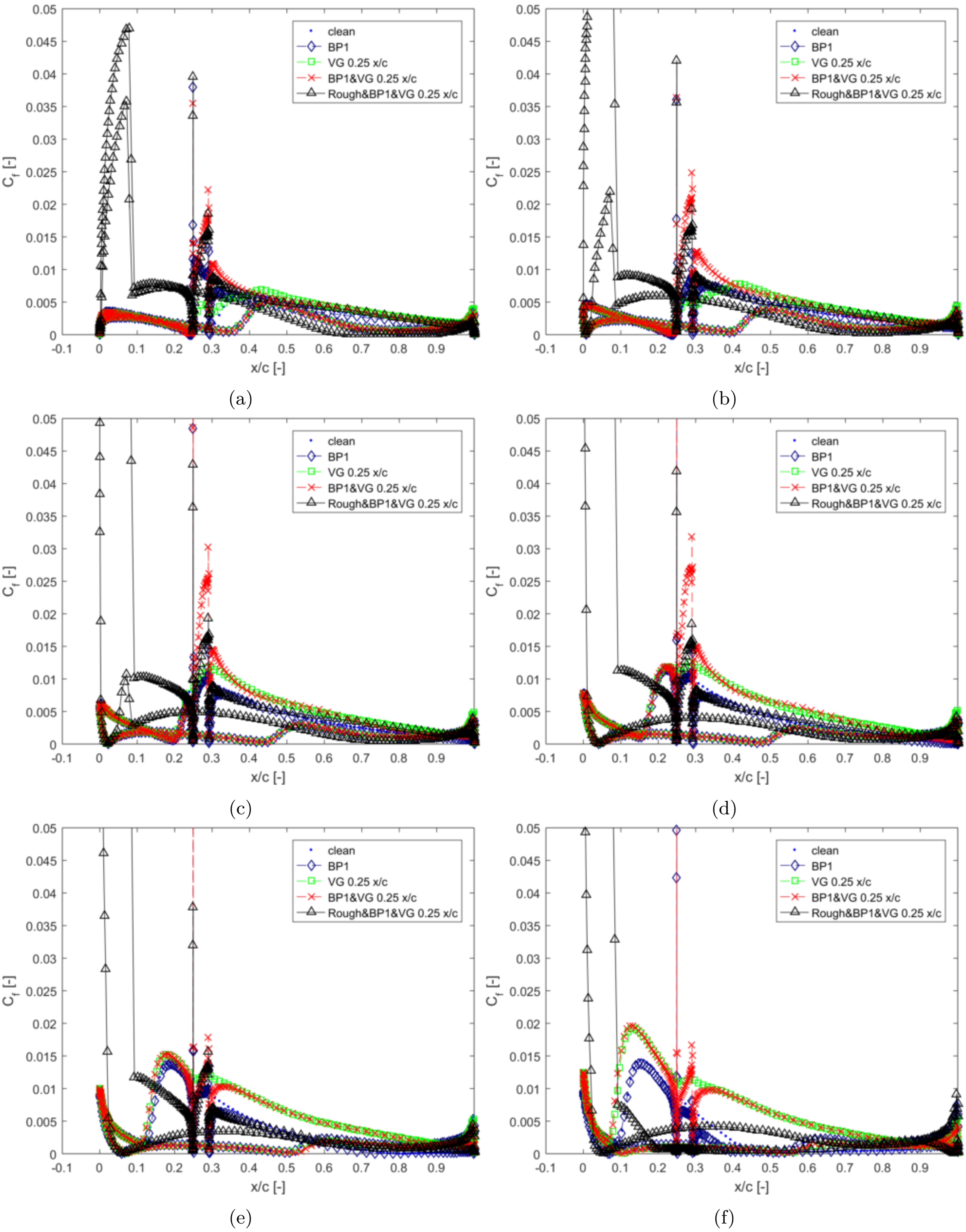

(a) (b) (c) (d) (e) (f)

Figure 4.23: Friction coefficient curves for the FFA-W3-301 airfoil at AoA of a) 0 , b) 4, c) 8, d) 12, e) 16, f) 20 degrees

4.2 DU 91 W2-250

4.2.1 Resolution Study

The resolution study is performed on DU 91 W2-250 airfoil. The number of cells around the airfoil (N_C) is 256, 128 cells in the normal direction and 384 cells in the span-wise direction. Number of cell in span-wise direction is obtained by trial-error on the airfoil section with VGs with the aspect ratio of 2.042 and 70 VGs. Set-up detail of this resolution study could be found in table 4.5. From the table grid 1 is the finest grid, whereas grid 4 is the coarsest grid. The simulation in this study is done using $k - \omega\ SST$ turbulence model with e^N method for transition model. For transition model, N value of 12 is used for this resolution study.

Figure 4.24 shows lift and drag coefficient of the airfoil section corresponding to each grid. From lift and drag polar, it could be seen that all results for the airfoil with VGs are in good agreement in the range of 0 to 10 degrees. The airfoil with VGs is separated at around 14.33 degrees in the experiment and between 15 and 20 degrees in the simulation. Difference in lift coefficient is seen in grid 1 at around 15 degrees. The rest of the simulation results are in good agreement between 0 and 15 degrees in both lift and drag coefficient. This can be concluded that the computation is insensitive to the span mesh-resolution for grid 2 to 4.

Although, it is recommended that the simulation should have done with the same airfoil section aspect ratio as in the experiment. This large wing span is however computationally expensive. From grid study lowering number of VGs (G1, G2 and G3) can also yield the same results as in grid 4 case. As it is seen from figure 4.24 that grid 2 and 3 yield to the same results as the simulation performed with grid 4. The simulation done on grid 3 is still computational expensive as the number of VGs is 34. Therefore, grid 2 is carried out for the remaining part of DU 91 W2-250 analysis. Further analysis is done in order to reduce the number of cells on the grid 2 and yields to the result of 64 cells in the span-wise direction.

Grid	N_c	N_N	N_S	$L_{S\backslash C}$	N_{VG}
1	256	128	384	0.234	8
2	256	128	384	0.525	18
3	256	128	384	0.992	34
4	256	128	384	2.042	70

Table 4.5: Resolution study set-up

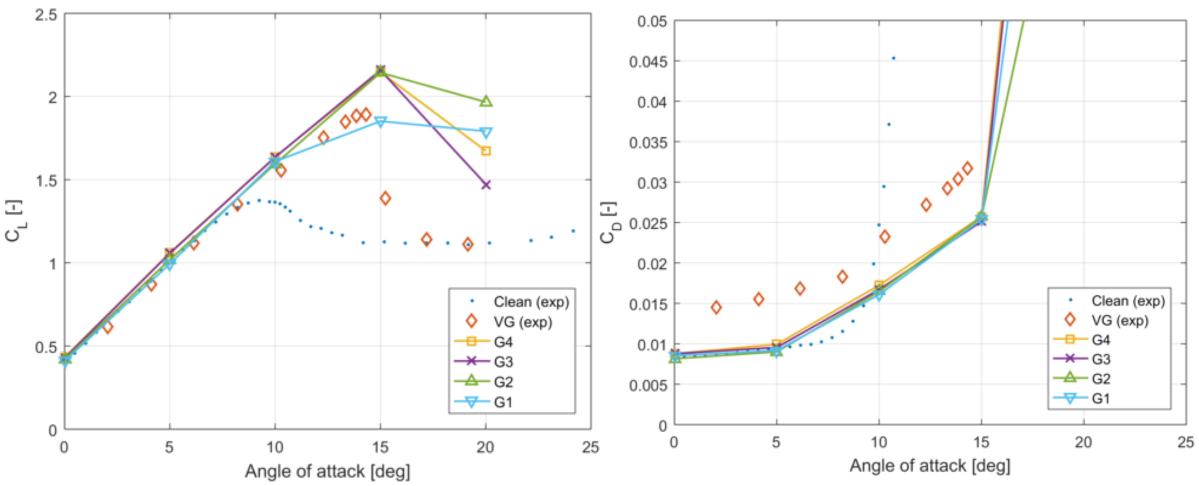

Figure 4.24: Comparison of lift and drag coefficient curves for DU 91-W2-250 airfoil with VGs calculated using different grid

4.2.2 Transition Study

Transition study of DU 91-W2-250 airfoil shows that both lift and drag results in the experiment and simulation are in good agreement for the angle of attack between 0 and 8 degrees as seen in figure 4.25. The drag coefficients in this range are slightly less than the experimental results by 14%. More differences between experimental and numerical results can be noticed between 8 and 20 degrees in the same figure. The reason for this variation can be as a results of prediction of the flow separation, which is an issue for CFD simulation [37]. Figure 4.26 shows that lower N value the results tend to get closer to the experimental result. The slope of the lift curves between 0 to 8 degree is computed and compared against experimental data. The detail of the lift curves can be found in the table 4.6. The slope of experimental result is in good agreement with the slope of numerical result for N equal to 11.5. The maximum lift for each N values changed slightly. Therefore, $N = 11.5$ value is selected and used throughout the research for DU 91-W2-250 airfoil with transition model.

For a clean and low turbulence intensity wind tunnel, the N value can be computed from turbulence intensity (0.07%) using equation A.14 and the corresponding N is 9. Chosen N value is higher but the results give a better agreement with the experimental data in the linear region.

It can be noticed from figure 4.26 that the numerical results are shifted to the left hand-side of the figure. A gap between numerical and experimental results is around 1.01×10^{-3} or approximately 12.8& difference. This offset is close to the value obtained for the FFA W3-301 airfoil, which has the gap of around 13.9% difference.

N	Slope	Max CL	AoA at CLmax
Exp	0.1180	1.375	9.24
9	0.1148	1.519	12.00
10	0.1161	1.543	12.00
11	0.1175	1.567	12.00
11.5	0.1181	1.580	12.00
12	0.1187	1.557	12.00

Table 4.6: Summary of transition study on DU 91-W2-250 airfoil

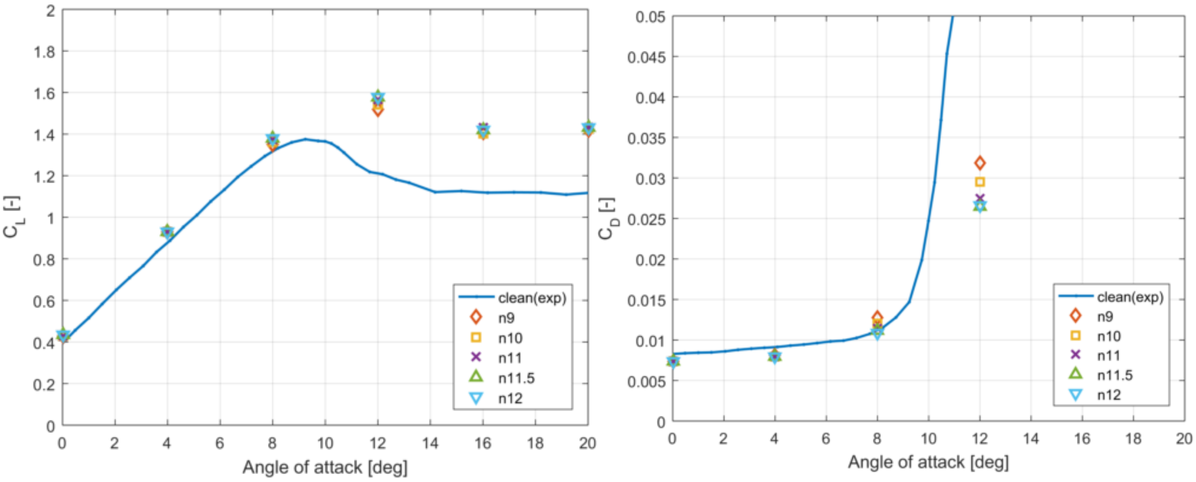

Figure 4.25: Comparison of lift and drag coefficient curves for the DU-91-W2-250 airfoil calculated using different N values

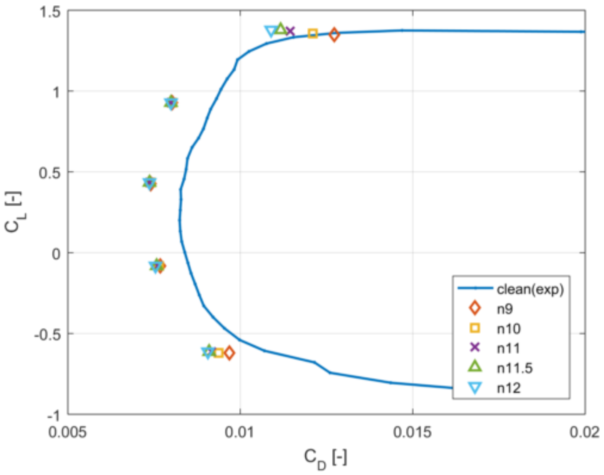

Figure 4.26: Lift over drag coefficient curve for the DU-91-W2-250 airfoil calculated using different N values

4.2.3 Effect of VGs' baseplate

From previous transition study, the N value of 11.50 is chosen for the e^N transition model. The flow in turbulence region is simulated using $k - \omega \ SST$ turbulence model. The shape of the baseplate in this studies illustrates in figures 3.3 to 3.7. In the following study, the airfoil is simulated with VGs at 0.30c.

4.2.3.1 Only VGs

The airfoil with only VGs at 0.30c is simulated. Figure 4.27 shows the comparison of lift and drag curves for the DU 91 W2-250 airfoil. For airfoil without VGs, the numerical results show good agreement with experimental data in the range of 0 to 8 degrees. Clean airfoil in the experiment stalls at around 9.73 degrees, where as it stalls between 12 and 16 degrees in the simulation. For drag coefficient, it is slightly underpredicted in the simulation at low angle of attack.

From figure 4.27, the airfoil with VGs shows good agreement between simulation and experimental results for lift coefficients in the range of 0 to 12 degrees. The airfoil with VGs shows that it could effectively delayed flow separation from around 9.73 to 14.33 degrees in the experiment and from around 12 to 17 degrees in the simulation. Difference can be noticed between experimental and numerical results. The maximum lift is increased by adding VGs by 50% when compared both simulation results of the airfoil with and without VGs. Likewise for the experimental results, the maximum lift coefficient is increased by approximately 38%.

From the drag curves in the figure 4.27, the airfoil with VGs has higher drag coefficients than the clean airfoil. The simulation results of the airfoil with VGs are underpredicted compared with the experimental results of the airfoil with VGs. By adding forces from the BAY model, the drag coefficient curve is elevated. The major difference between the airfoil with and without additional BAY model forces was found at low angle of attack. At high angle of attack (18 degrees), the difference is less than 1 percent and the forces from BAY model can be ignored.

Additional forces from BAY model are added into then numerical results. There is no significance difference for lift curve between with and without BAY model forces. However, the drag force is substantially increased at low angle of attack when BAY model forces are taken into accounted. This is evidenced that forces from BAY model are crucial and cannot be ignored. In the following studies, forces from BAY model are added into the numerical results.

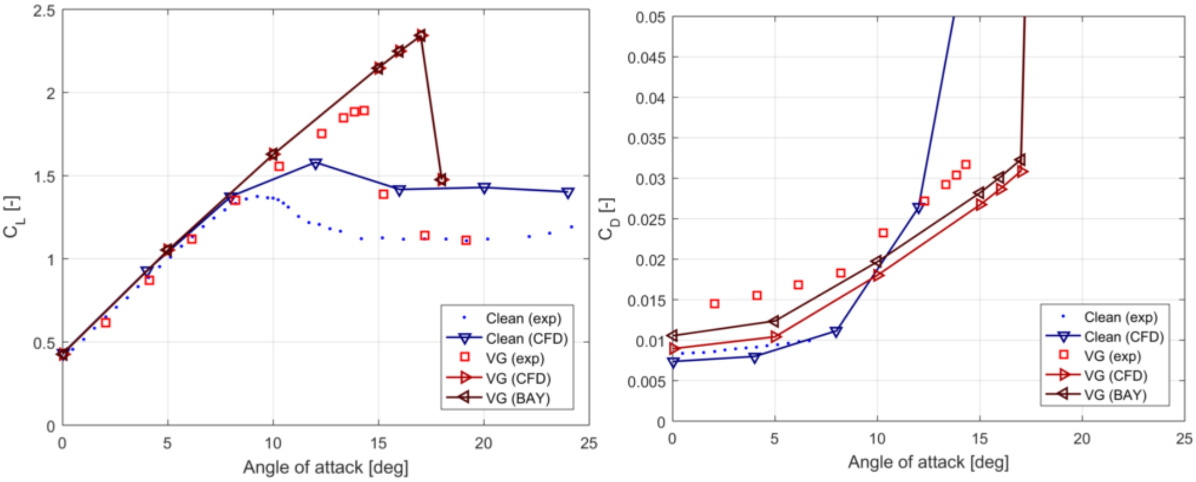

Figure 4.27: Comparison of lift and drag coefficient curves for the DU 91 W2-250 airfoil

AoA [degree]	0	5	10	15	16	17	18
%Difference	17.93	18.79	9.24	5.56	5.10	4.64	0.56

Table 4.7: Percentage increase in drag coefficient when including forces from BAY model

4.2.3.2 Only VGs' Baseplate

The VGs' baseplate is added to the DU 91-W2-250 airfoil. The results are shown in figure 4.28. There is no significance difference between the results from difference baseplate shapes for lift and drag coefficients. From the simulation, the lift coefficient from the airfoil with the baseplate shows no difference to the simulation clean airfoil from 0 to 12 degrees. All simulation lift curves are in good agreement with the experimental results in the range of 0 to 5 degrees.

The drag coefficients from the airfoil with the baseplates are higher than the clean airfoil in both experiment and simulation in the range from 0 to 8 degrees. After around 10 degrees the drag coefficients of the experimental clean airfoil dramatically increase and are higher than the simulation results. The simulation results for the airfoil with and without baseplates are congruent after the angle of attack of 8 degrees.

Disagreement between experiment and simulation drag coefficient in clean airfoil is noticed in the previous section. By considering only the simulation results, this can be concluded that the airfoil with baseplate has no influence to the lift force for DU 91 W2-250 airfoil. The presence of the baseplate is only effect to the drag coefficients of the airfoil at low angle of attack (< 8 degrees). The effect of the baseplates on the clean airfoil can be ignored at high angle of attack.

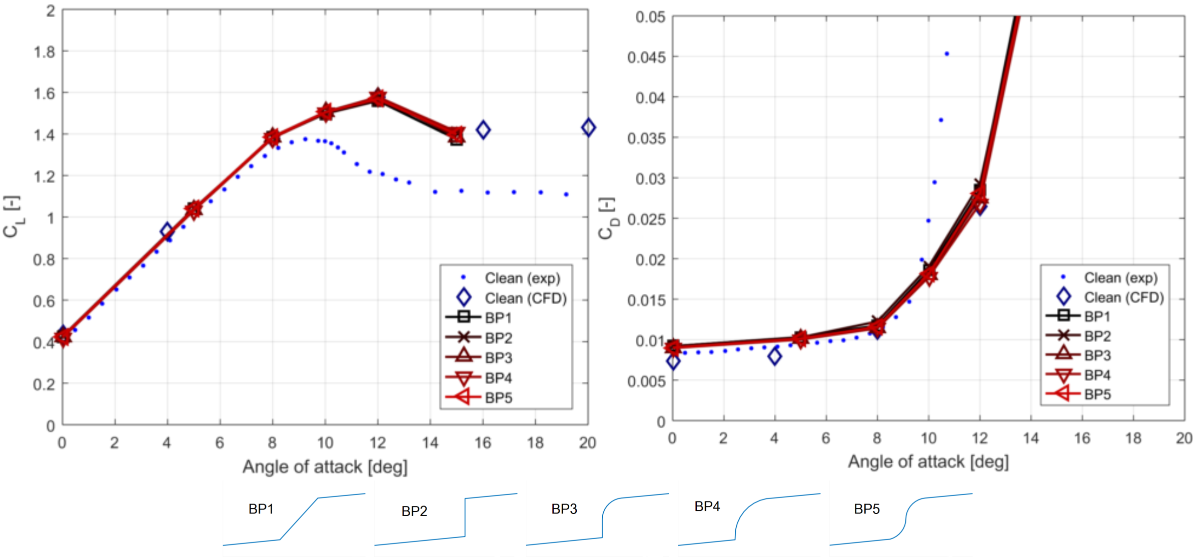

Figure 4.28: Comparison of lift and drag coefficient curves for the DU 91 W2-250 airfoil with different baseplate shapes

4.2.3.3 VGs & Baseplate

Figure 4.29 shows comparison of lift and drag curves for DU 91-W2-250 airfoil with VGs at 0.30c for difference baseplate shapes. It can be seen that baseplate shape no.1, 3 and 5 are in good agreement with the one without baseplate and separated around 17 to 20 degrees. These baseplate configurations have shown effectively control flow separation when compared with the clean airfoil results which is separated at between 12 and 16 degrees. The airfoil with baseplate shape no.2 has the worst performance compared to others geometries. It shows an early separation around 12 to 14 degrees which is much lower than the airfoil with only VGs and with VGs&Baseplate (stall at around 17 to 20 degrees). The baseplate shape no.4 also shows early separation at around 15 to 17 degrees.

The right hand-side of the figure 4.29 shows drag coefficient of DU 91 W2-250 airfoil with VGs at 0.30c for difference baseplate shapes. The airfoil with VGs configurations has generally higher drag coefficient than the clean airfoil in the range between 0 to 10 degrees. It is seen that baseplate shape no. 2 and 5 have slightly higher drag than the experimental results of the airfoil with VGs at the angle of attack between 0 to 5 degrees. The drag coefficient for the baseplate shape no.2 jumps at the angle of attack of 12 degrees due to flow separation. For angle of attack below 10 degrees, airfoil with baseplates have higher drag compared with the simulated airfoil without baseplate except for the baseplate shape no.4.

One clear effect of the airfoil with VGs and baseplate is that the airfoil section with baseplate shape no. 2 and 4 are separated early. The lift curves of the baseplate shape no. 1, 3 and 5 are in good agreement with the airfoil without baseplate. The airfoil with baseplates have higher drag coefficient than the simulated airfoil without baseplate at low angle of attack (<10 degrees) except baseplate shape no.4.

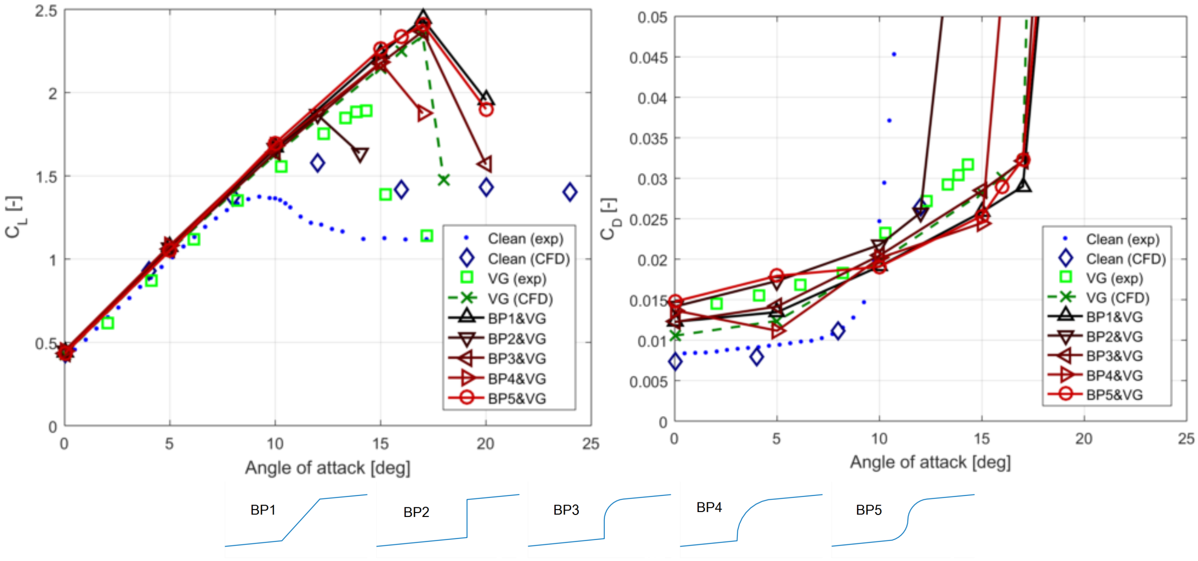

Figure 4.29: Comparison of lift and drag coefficient curves for the DU 91-W2-250 airfoil with VGs and different baseplate shapes

4.2.4 VGs' Position

Effect of VGs' position on DU 91-W2-250 airfoil is studied and shows in figure 4.30. It can be noticed that all results are in good agreement for the linear part of the lift curves in the range of 0 to 8 degrees. From the experimental results, flow separations occurs around 14 degrees for both VGs' positions. In the experiment, the airfoil with VGs at 0.30c suddenly drops at around 15 degrees. The airfoil with VGs at 0.20c tends to have flow attached after its lift coefficient drops due to flow separation at around 14.8 degrees. This could mean that the flow separation might occur earlier on the airfoil with VGs at 0.30c, however the results resolution at the maximum lift coefficient is inadequate. From the numerical results, it is seen that VGs at 0.20c separated at around 16 degrees which is earlier than the VGs at 0.30c (around 17 degrees). The differences are also very small for the simulation results. It also noticed that for the airfoil with VGs at 0.20c, flow seems to not attached after its separated at around 16 degrees likes in the experiment.

From the experimental results, it is seen that moving the VGs toward the leading edge, different amount of drag coefficient between both VGs positions gradually rises as the angle of attack increases. Similar trends can be observes in the numerical results in the range of 0 to 5 degrees. The simulated airfoil with VGs at 0.20c had slightly higher drag than the VGs at 0.30c. The amount of drag increase remains the same in the range of 5 to 16 degrees with the values of approximately 7%.

Both experimental and numerical results show that there is a small difference in the airfoil characteristics between VGs' at 0.20c and 0.30c. In the experiment, VGs at 0.20c shows a slightly better flow separation control even after the stall angle of attack, whereas it is better to put the VGs at 0.30c in the simulation. By moving the VGs towards the leading-edge, the drag coefficients slightly increases.

4.2.5 Reynolds Number Study

Reynolds number study is done on the DU 91-W2-250 airfoil. The airfoil with Reynolds number of 3.33×10^6 and 5×10^6 are investigated. The baseplate shape no.1, 2 and 5 are studied. The N value of 11.50 is used for the e^N transition model and $k - \omega\ SST$ for the turbulence model. In this study, the airfoil is simulated with VGs' position at 0.30c.

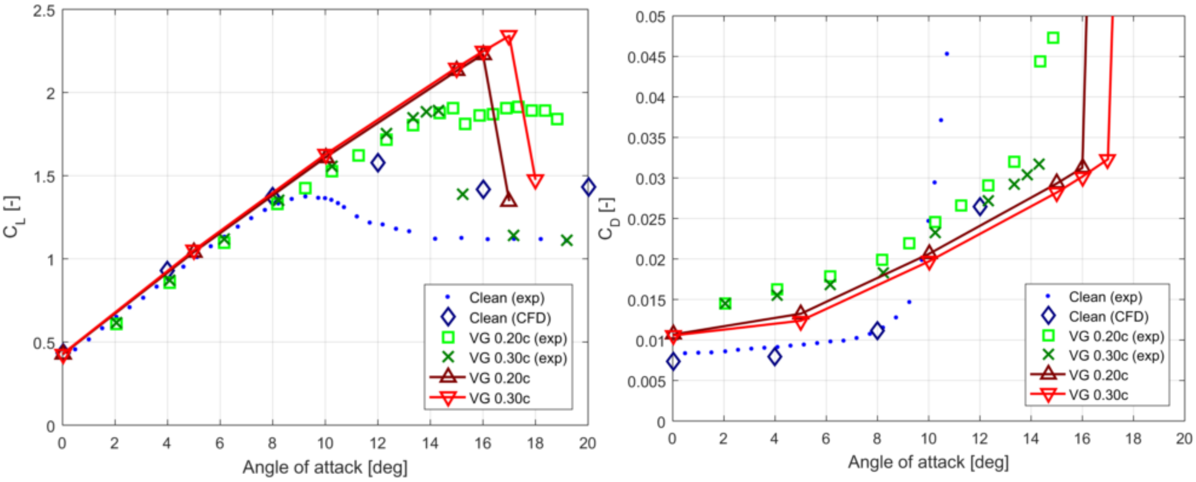

Figure 4.30: Comparison of lift and drag coefficient curves for the DU 91-W2-250 airfoil with VGs at different VGs' locations

4.2.5.1 Only VGs

Figure 4.31 shows the lift and drag coefficients curve of the DU 91-W2-250 airfoil at difference Reynolds numbers. The clean airfoil shows a slight increase of maximum lift at higher Reynolds number by approximately 3.5%. For the airfoil with VGs, there is no significance change in the lift curve. The airfoil with and without VG at higher Reynolds number (5×10^6) show slightly higher drag coefficient. However, after around 8 degrees, the drag coefficient of the clean airfoil at Reynolds number of 3.33×10^6 is higher. This mean that for the airfoil with VGs, drag coefficient increases as the Reynolds number rises.

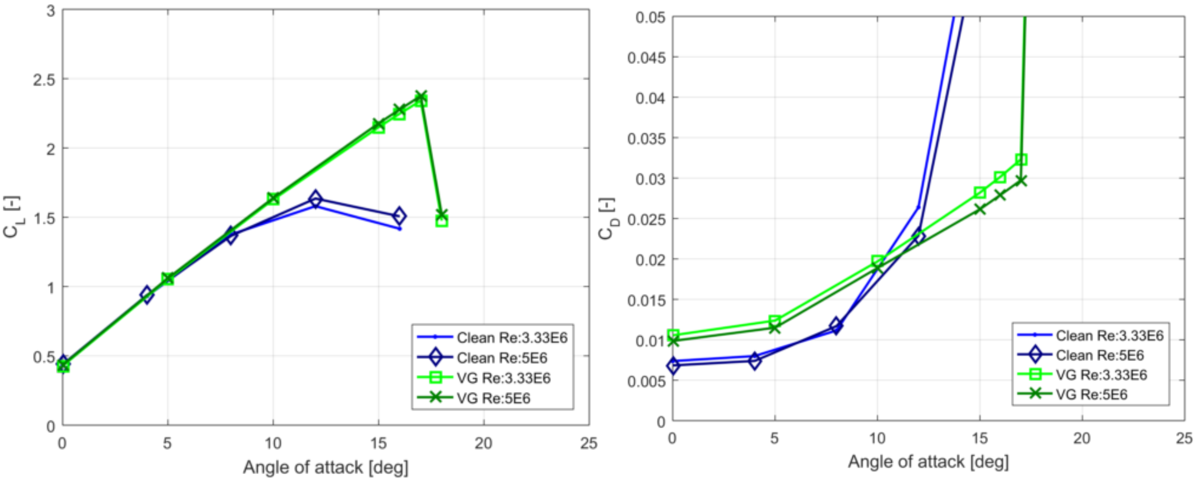

Figure 4.31: Comparison of lift and drag coefficient curves of the DU 91-W2-250 airfoil at different Reynolds numbers

4.2.5.2 VGs' Baseplate

Figure 4.32 shows the airfoil simulation with baseplate shape no.1, 2 and 5. It can be seen that the results of the airfoil at Reynolds number of 3.33×10^6 and 5×10^6 with baseplate are in good agreement to each other for both lift and drag coefficients. The clean airfoil with Reynolds number of 5×10^6 has higher maximum lift compared to the one with lower Reynolds number and is the highest. The maximum lift coefficient is reduced on the airfoil with baseplate configurations.

There is no significance difference in drag coefficients between results from both Reynolds numbers. The airfoil with baseplate shows higher drag coefficients than the clean airfoil in the range of 0 to 8 degrees.

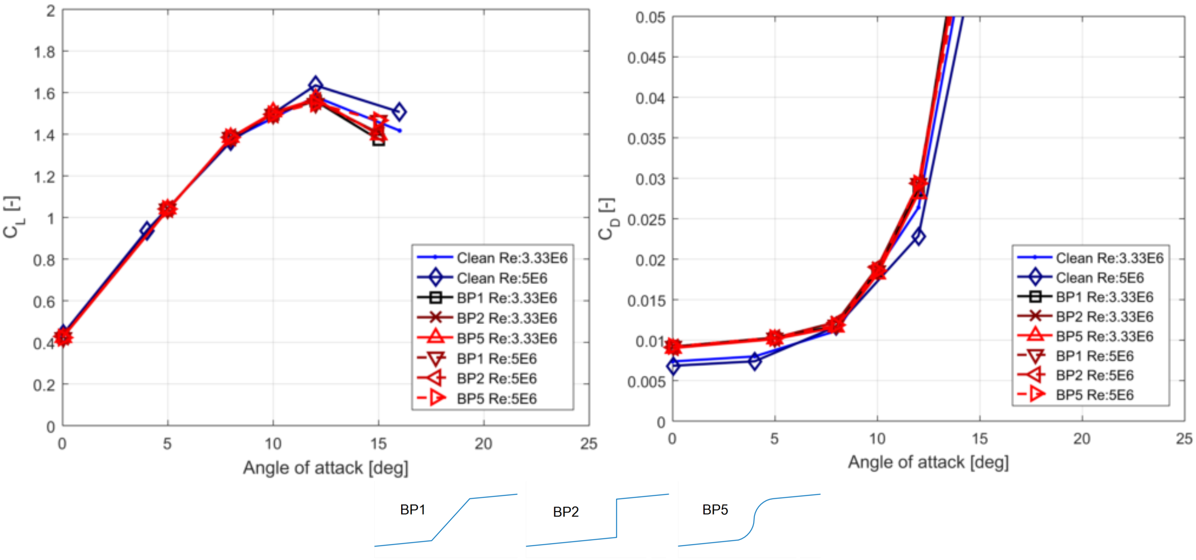

Figure 4.32: Comparison of lift and drag coefficient curves of the DU 91-W2-250 airfoil at different Reynolds numbers

4.2.5.3 VGs & Baseplate

The airfoil with baseplate and VGs is simulated and the results show in figure 4.33. It could be seen from the lift curve that the baseplate shape no.2 separates around 12 degrees at the Reynolds number of 3.33×10^6, whereas it separates later around 14 degrees at higher Reynolds number (5×10^6). The airfoil with baseplate shape no.1 and 5 are stalled at the angle of attack around 17 degrees. Similarly the airfoil with only VGs stalled at about the same angle of attack.

It could be seen that the drag coefficient decreases as the Reynolds number increases. The airfoil with baseplate shape no.5 with the Reynolds number of 3.33×10^6 has the highest drag coefficient in low angle of attack range (0 to 5 degrees). For the angle of attack greater than 5 degrees, the airfoil with baseplate shape no.2 at Reynolds number of 5×10^6 has the highest drag among other configurations until it jumps at around 12 degrees. There is very small differences between the airfoil section with baseplate shape no.1 at Reynolds number of 3.33×10^6 and 5×10^6. The one with lower Reynolds number has slightly higher drag coefficients.

The effect of the Reynolds numbers to the airfoil with VGs & baseplate is pronounced on the baseplate shape no.2. Increasing the Reynolds number can improve control of the flow separation on the airfoil section with baseplate shape no.2. Besides, drag coefficients are reduced as the Reynolds number increased as seen in the airfoil with baseplate shape no.2 and 5.

4.2.6 Baseplate's Height Study

Baseplate's height study is performed on the airfoil with and without VGs. The baseplate height of $0.667c\times10^{-3}$ and $1.000c\times10^{-3}$ are studied. The simulation is performed with $k-\omega$ SST turbulence model and e^N method for transition model ($N = 11.5$). The VGs are at 0.30c.

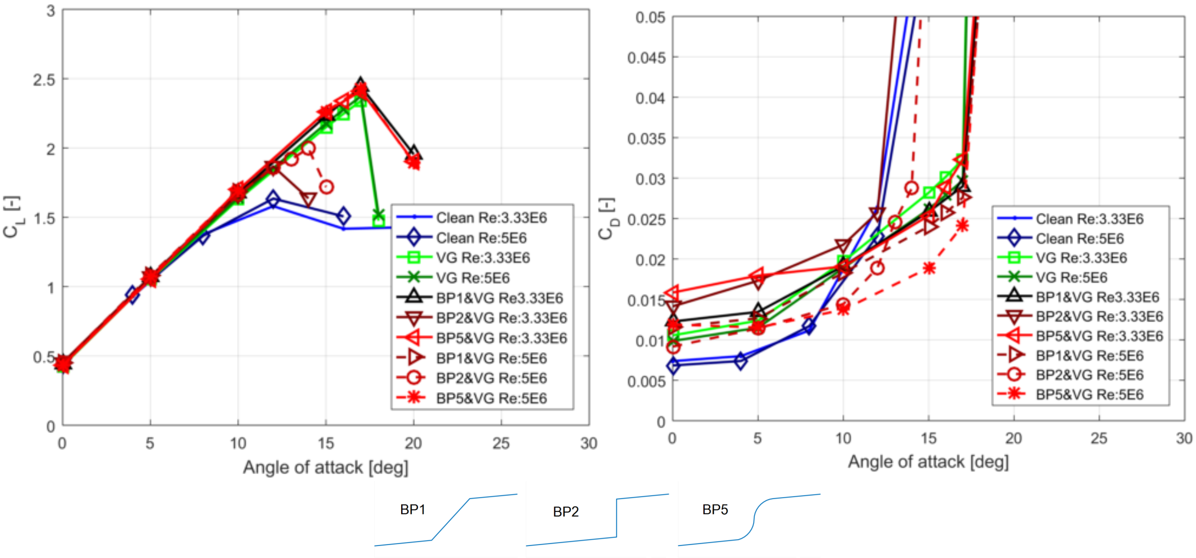

Figure 4.33: Comparison of lift and drag coefficient curves of the DU 91-W2-250 airfoil at different Reynolds numbers

4.2.6.1 Only VGs' Baseplate

From figure 4.34, the simulation results of the airfoil with and without baseplate are congruent in the range of 0 to 12 degrees. The airfoil with baseplates show slightly lower maximum lift coefficient compared with the simulated clean airfoil. The baseplate shape no.2 with the height of $1.000c\times10^{-3}$ has the least maximum lift coefficient.

In the same figure, the drag coefficients of the airfoil with baseplates are higher than the clean airfoil in the range between 0 and 8 degrees by approximately 25% in the simulation and 10% in the experiment. There is no significance difference noticed in drag coefficient between 0 to 8 degrees among the airfoil with baseplate configurations. The amount of drag increase in the airfoil with baseplate shape no.1, 2 and 5 are approximately 0.3%, 3.6% and 1.5% respectively. The baseplate shape no.2 with the height of $1.000c\times10^{-3}$ has the highest drag among other airfoil configurations.

4.2.6.2 VGs & Baseplate

From figure 4.35, it is seen that the airfoil with VGs&baseplate has higher lift coefficient than the simulated clean airfoil. The airfoil with baseplate shape no.1 and 5 at both heights are in good agreement and separated in the range between 17 and 20 degrees. Besides, they show slightly higher maximum lift coefficient than the simulated airfoil with only VGs. The baseplate shape no.2 at both height are in congruent to each other. They show early separation at around 12 to 14 degrees when compared with other airfoil with VGs configurations. They also have slightly lower maximum lift coefficient when compared with the experimental airfoil with VGs.

For the angle of attack in the range between 0 and 5 degrees, the drag coefficients of the airfoil with baseplate height of $1.000c\times10^{-3}$ are higher than the one with the height of $0.667c\times10^{-3}$. The airfoil with baseplate shape no.5 with both heights show the highest drag in the range of 0 to 5 degrees. They have also higher drag coefficient than the experimental results of the airfoil with VGs in the same region. After that the airfoil with baseplate shape no.2 has the highest drag coefficients before the one with the baseplate height of $1.000c\times10^{-3}$ jumps at around 10 degrees. The airfoil with baseplate shape no.2 with the height of $1.000c\times10^{-3}$ shows a good agreement to the experimental results of the airfoil with VGs in the range between 0 and 10 degrees. The same airfoil configuration with the baseplate height of $0.667c\times10^{-3}$ has slightly higher lift coefficient at around 5 degrees but the rest of the results between

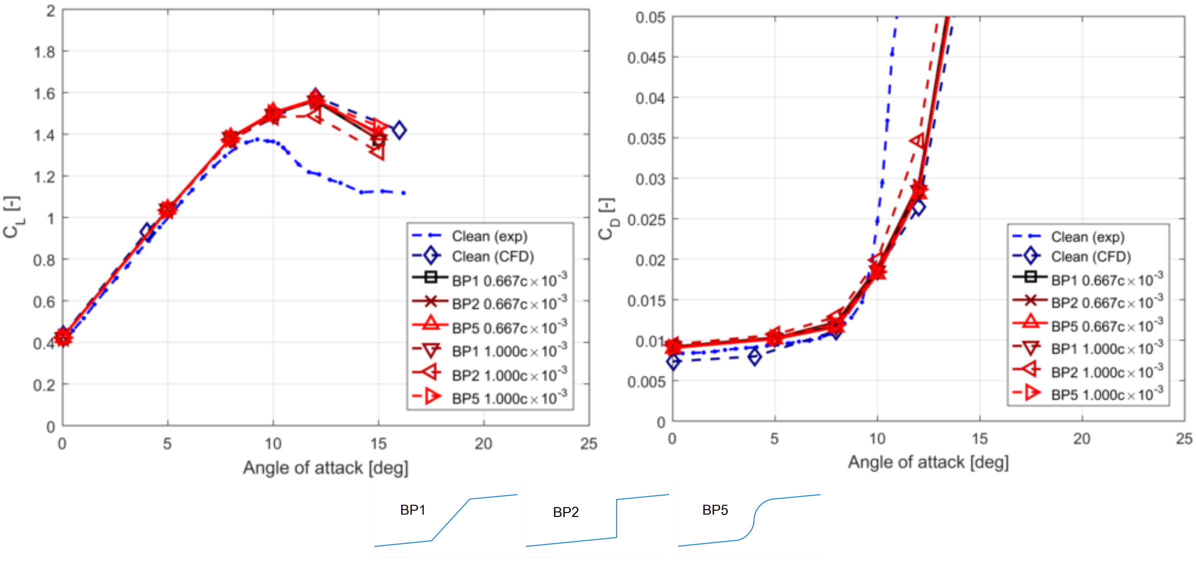

Figure 4.34: Comparison of lift and drag coefficient curves of the DU 91-W2-250 airfoil with different baseplate heights

0 to 10 degrees are in good agreement with the experiment.

This can be concluded for the airfoil without VGs, an increase of the baseplate height yields a decrease of the maximum lift coefficient. The airfoil with baseplate shape no.2 has the lowest maximum lift coefficient. Besides, the drag coefficient also rises as the height increases. The amount of drag increase is large for the airfoil with the baseplate shape no.2, whereas it is negligible for the airfoil with the baseplate shape no.1. For the airfoil with VGs, these two level of baseplate height seems to have little affected to the airfoil drag coefficients. The one with higher elevation has slightly higher drag coefficient at some angle of attack.

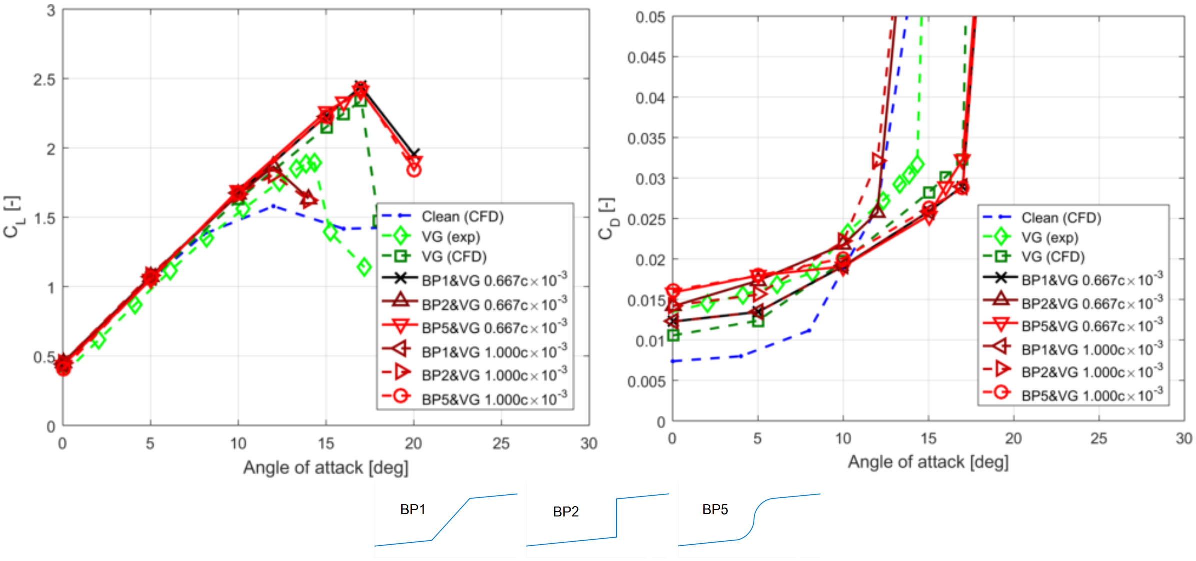

Figure 4.35: Comparison of lift and drag coefficient curves of the DU 91-W2-250 airfoil with VGs at different baseplate heights

4.2.7 Roughness Study

Roughness study on the DU 91 W2-250 airfoil is performed. The leading edge of the airfoil up to 0.08c is covered by the sand roughness as in the table 4.3. The set-up is exactly the same to the previous study done on the FFA W3-301 airfoil.

Figure 4.36 illustrates the comparison of lift and drag curves vs angle of attack of the DU 91-W2-250 airfoil with different surface treatments. The airfoil with roughness has much lower lift in comparison with the numerical results from the clean airfoil. The maximum lift coefficient drops from around 1.6 to 1.2 (approximately 25%). The drag coefficient of the rough airfoil increases almost twice of the drag force on the clean airfoil at the angle of attack below 10 degrees. The drag curve of the rough airfoil increases dramatically after 5 degrees due to flow separation. The results of the airfoil with fully turbulent and hydraulically smooth 1 set-up are in a good agreement in both lift and drag polar. However, the results of the airfoil with hydraulically smooth 2 configurations show slightly lower maximum lift coefficient (approximately 1%) and higher drag coefficients (approximately 3%) compared with the fully turbulent model.

4.2.7.1 VGs´ Position

Effect of VGs on the rough airfoil is shown in figure 4.37. The lift loss due to the leading edge roughness is restored by adding VGs on the airfoil. Moving VGs towards the airfoil trailing-edge has slightly improved the control of the flow separation. Hence, VGs' position has little effect to the flow separation control as it is mentioned in the earlier section. By adding VGs the linear part of the lift curve is extended. For the airfoil with the rough surface, flow separation starts around 5 degrees, whereas the ones that had VGs the linear lift curve is prolonged to around 10 degrees and eventually stalled around 15 degrees.

From previous results on the FFA W3-301 airfoil, the lift curve is recovered from the rough airfoil by installing VGs but the effect of VGs is limited. Although, the lift forces are regained but they are still below the clean airfoil curve as seen in figure 4.17. In contrast, for DU 91 W2-250 airfoil the lift curve is restored and is higher than the clean airfoil as seen in figure 4.37. This could be evidenced that the roughness sensitivity of the DU 91 W2-250 airfoil is less than FFA-W3-301 airfoil.

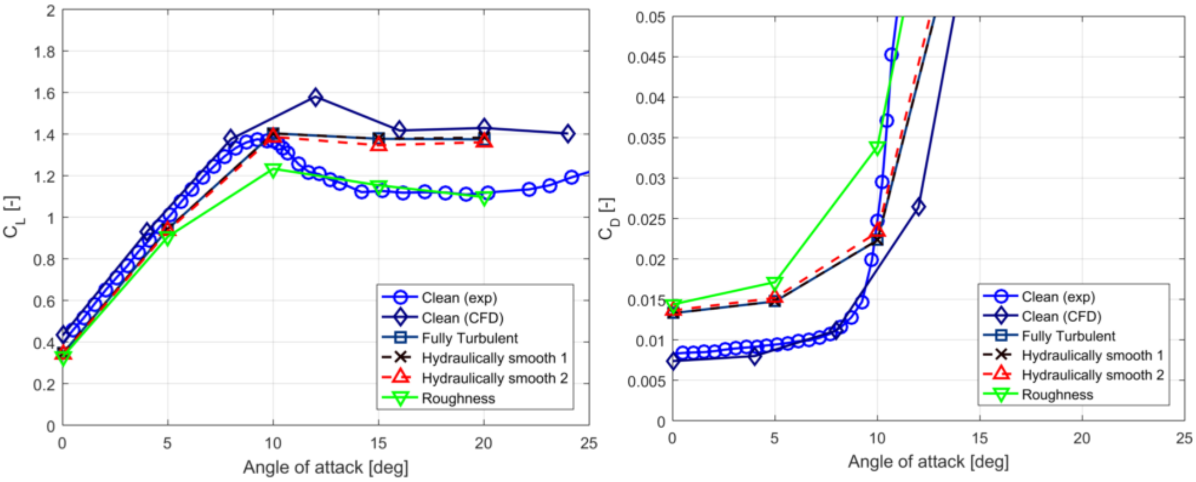

Figure 4.36: Comparison of lift and drag coefficient curves of the DU 91-W2-250 airfoil with different surface treatments

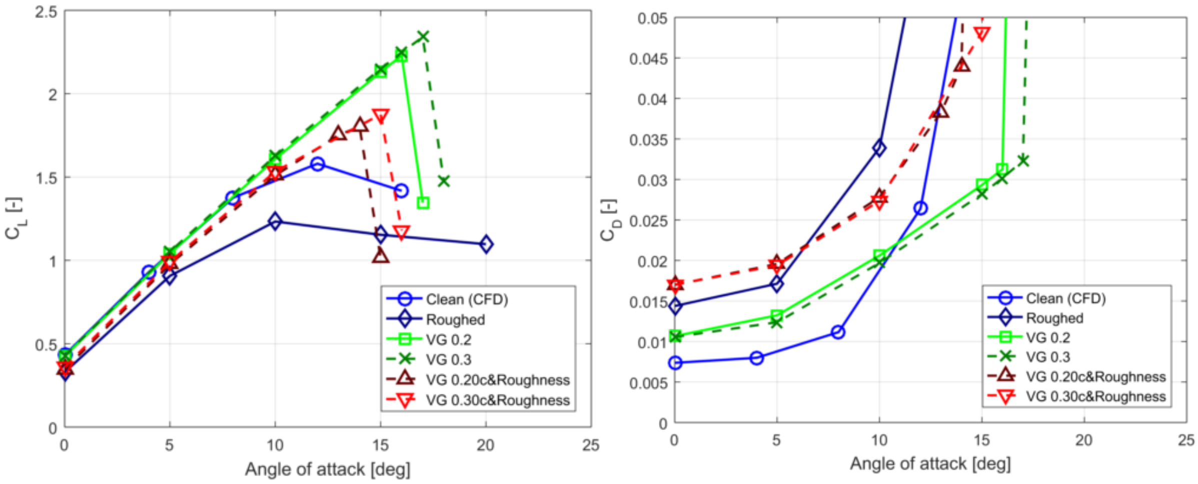

Figure 4.37: Comparison of lift and drag coefficient curves of the DU 91-W2-250 airfoil with roughness at different VGs' position

4.2.7.2 VGs' Baseplate

The effect of VGs' baseplate to the rough airfoil is studied. Figure 4.38 illustrates the lift and drag curves for the DU 91-W2-250 airfoil with roughness, baseplate, and VGs (at 0.30c). It is seen that VGs has improved the lift curve for the airfoil with roughness and baseplate. The baseplate shape no. 1 shows the highest maximum lift coefficient compared with other configurations. The lift curve of the baseplate shape no.1 is in good agreement to the airfoil with VGs and without roughness in the range of 0 to 15 degrees. This could mean that the roughness has less affect to the airfoil with baseplate shape no.1. The airfoil with VGs can effectively restore the losing lift due to the roughed surface. However, other baseplate shapes could not perform well as in the baseplate shape no. 1. This could be as a result of the shape of the baseplate. The flow passing over the blaseplate with shape no.1 might accelerate due to its beveled shape unlike the other shapes where the flow stagnates. The sharp bevel baseplate likes no.2 and 3 have shown that they are less effectively control the flow separation as in the airfoil with baseplate shape no.1. The baseplate shape no.5 shows earlier separation and lower lift at around 16 degrees. The baseplate shape no.2 and 4 are in good agreement to each others and separates at around 14 degrees. The worst performance could be found on the baseplate shape no.3. It is separated at around 15 degrees and has the least lift compare to others airfoil with VGs and baseplate configurations. The roughed airfoil with VGs has the lowest lift among the results.

The right hand-side of the figure 4.38 shows drag coefficient of the DU 91-W2-250 airfoil with roughness, baseplate, and VGs. For the airfoil with the roughness, the drag coefficient is higher than the clean airfoil and airfoil with VGs. For angle of attack in the range of 0 to 10 degrees, there are small variation among rough airfoil cases. The baseplate shape no. 2 has the highest drag in this range. The baseplate shape no.2 and 4 dramatically rise at around 14 degrees whereas other shapes jumped at around 15 degrees due to flow separation.

By installing the VGs on the rough airfoil section, lift loss is substantially improved especially for the airfoil with baseplate shape no.1. The lift curve of the rough airfoil with only VGs is higher than the simulated results from clean airfoil, which means that DU 91 W2-250 airfoil is less sensitive to the roughness when compared with FFA W3-301 airfoil. The effect of the baseplate in combination with the surface roughness is expected to be worse, however the baseplate has actually improved the the flow separation on the DU 91-W2-250 airfoil. One of the possible explanation is that, the flow passing over the blaseplate might accelerate due to its beveled shape.

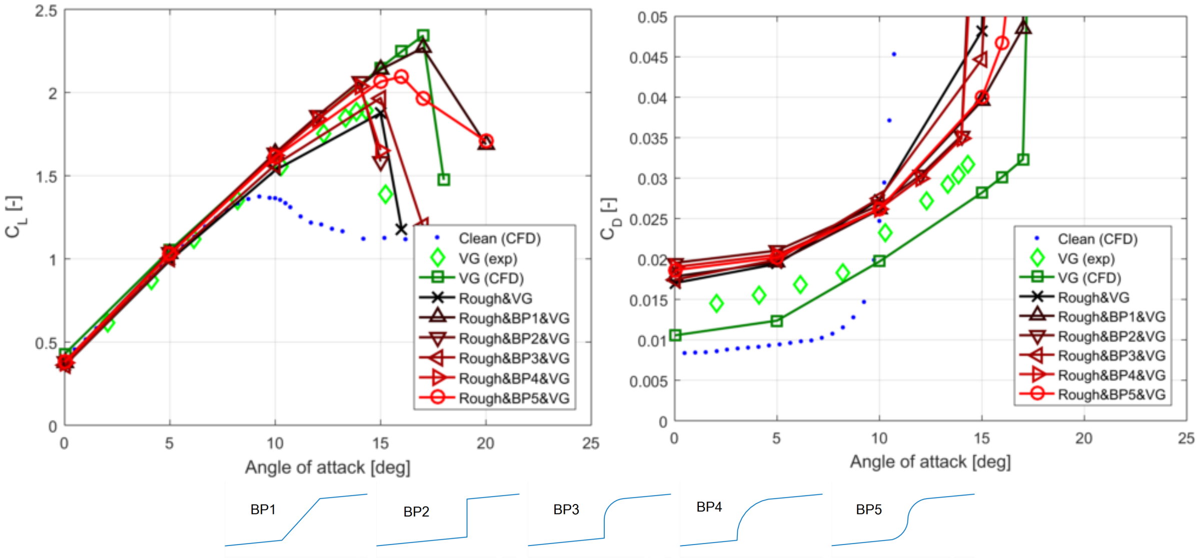

Figure 4.38: Comparison of lift and drag coefficient curves for the DU 91-W2-250 airfoil with surface roughness for different baseplate shapes

4.2.7.3 Annual Energy Production (AEP)

The airfoil with roughness, baseplate and VGs is further analyzed using the wind turbine model as described in the Appendix C.

Figure 4.39 illustrates power and thrust curves of the DU 91 W2-250 airfoil with roughness and VGs. The rough airfoil shows the lowest performance among the other cases. From the power curve the rough airfoil without VGs shows less power production in the range of the wind speed of 5 to 12 m/s. The power curve of the blade with and without VGs are in good agreement. From the thrust curve, clean airfoil has the lowest maximum thrust compared with other configurations. The rough airfoil has slightly lower thrust when compared with the ones with VGs. This means that by introducing VGs, maximum thrust increased.

Effect of baseplate to the rough airfoil with and without VGs is shown in figure 4.40. The rough airfoil still shows the lowest performance. There is no significance difference in power curve among various baseplate shapes. Clean airfoil slightly produces higher power in the wind speed range from 5 to 10 m/s. On the right hand-side of the figure 4.40 shows thrust for each cases. The highest thrust is found in the airfoil with VGs & baseplate shape no.2.

From table 4.8, the rough airfoil has the lowest annual energy production at 8.90 GWhr. By adding only VGs, the energy production is improved by approximately 7%. The airfoil with baseplate and VGs show higher annual energy production than the airfoil with only VGs by around 3%-4%. The highest annual energy production could be found on the airfoil with baseplate shape no.1. The rough airfoil with VGs at 0.30c has the highest thrust. The airfoil with VGs & baseplate shape no.2 has the highest thrust among other airfoil with baseplate configurations.

A slight improvement in the rough airfoil with VGs&baseplate could be as a result of the bevel of the baseplate has accelerated the flow. However, baseplate shape no.2 seen to have slightly higher AEP than the one with only VGs, this could be as a result of inadequate resolution of the results (5 degrees).

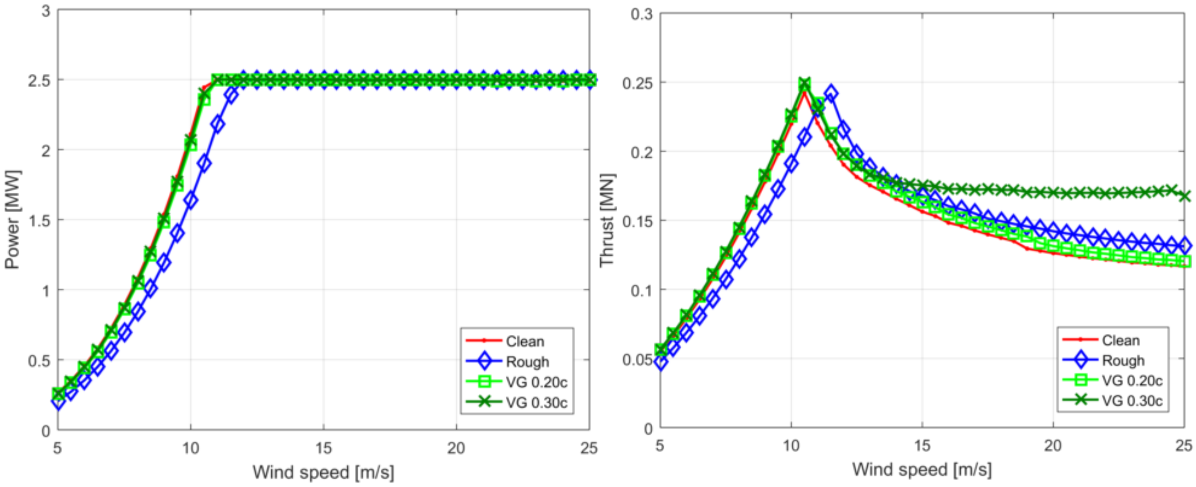

Figure 4.39: Comparison of power [MW] and thrust [MN] of the DU 91-W2-250 airfoil with surface roughness and VGs

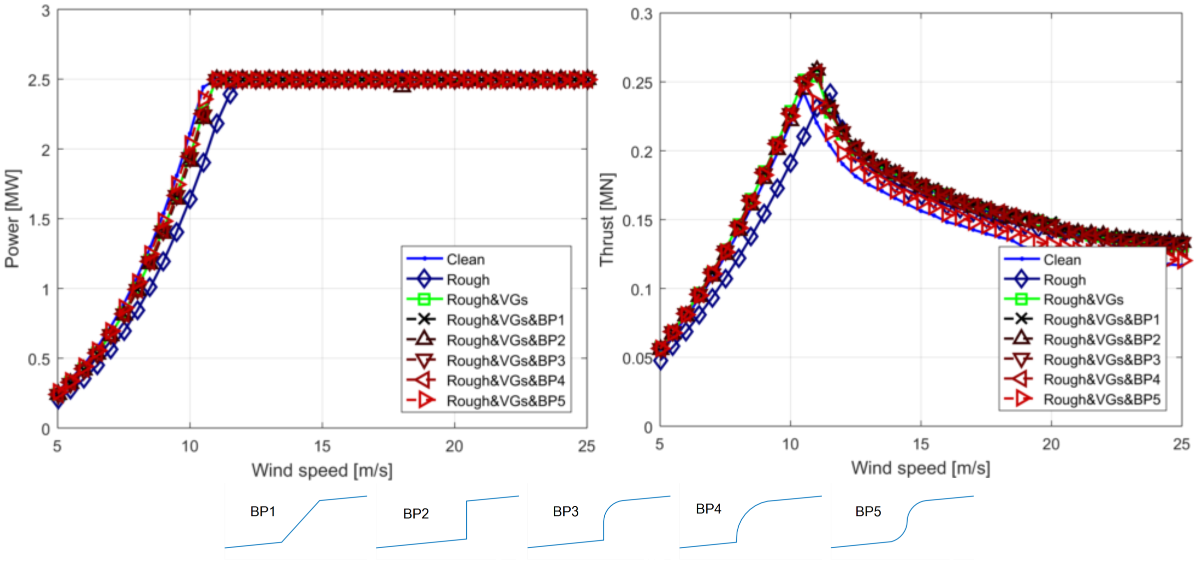

Figure 4.40: Comparison of power and thrust of the DU 91-W2-250 airfoil with surface roughness and VGs for different baseplate shapes

Cases	$AEP[GWhr]$	%Difference	Max. Thrust [MN]	%Difference
Clean	10.22	-	0.242	-
Rough	8.90	-12.89	0.241	0.33
Rough & VGs 0.20c& Roughness	9.43	-7.71	0.256	5.82
Rough & VGs 0.30c& Roughness	9.56	-6.44	0.260	7.45
Rough & VGs & BP1& Roughness	9.82	-3.93	0.254	4.85
Rough & VGs & BP2& Roughness	9.79	-4.24	0.260	7.10
Rough & VGs & BP3& Roughness	9.72	-4.90	0.258	6.61
Rough & VGs & BP4& Roughness	9.79	-4.20	0.256	5.85
Rough & VGs & BP5& Roughness	9.80	-4.12	0.257	5.99

Table 4.8: Wind turbine Annual energy production

4.2.8 Pressure & Friction

Figures 4.41 and 4.42 show pressure and friction distribution over DU 91-W2-250 airfoil with baseplate shape no.1. It could be seen from both figures that the presence of baseplate caused fluctuation at the baseplate position in both pressure and friction distributions. There is no significance effect of the baseplate to the airfoil at low angle of attack as seen in figure 4.41. However, at high angle of attack, the airfoil with baseplate is seen to have lower pressure suction as seen in figure 4.42 (a) and (b). By installing VGs, the baseplate effect is diminished up to a certain angle of attack. Figure 4.42 (b) shows that the airfoil with baseplate and VGs has more pressure suction. This could result in higher lift in this case.

It could be seen from figures 4.41 and 4.42 that by covered airfoil leading-edge with roughness, the friction coefficient substantially jumps. The friction coefficient then drops and jumps again due to the presence of VGs or baseplate.

The flow separation can be noticed from pressure coefficient plot in figure 4.42 (b) in the airfoil with only baseplate no.1 configuration. The pressure coefficient curve has high adverse pressure gradient and eventually flat at around 0.35 x/c. This is indicated that the flow has already separated. Corresponding friction coefficient curve (b) also shows a dipped at 0.60 x/c.

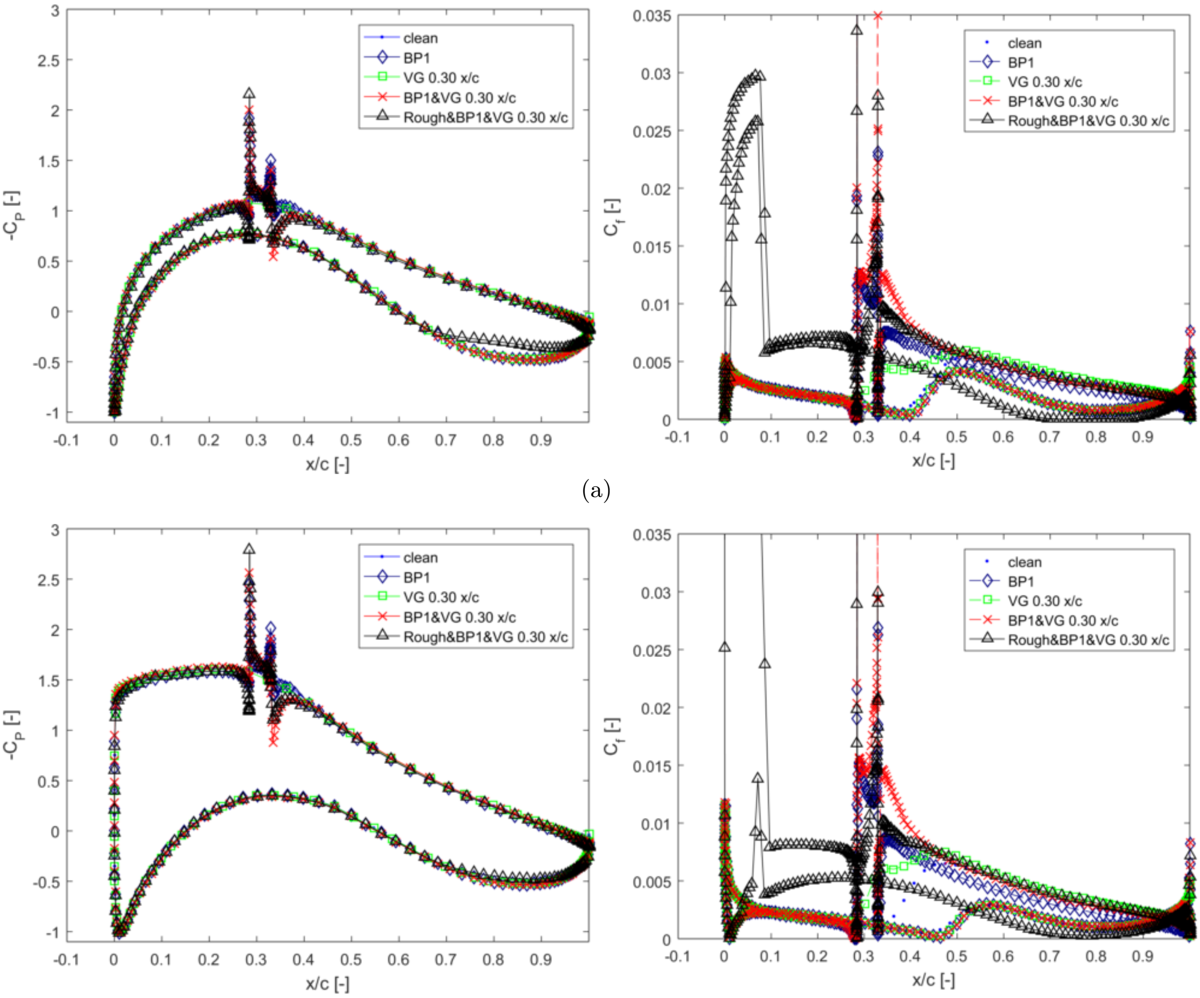

(a)

(b)

Figure 4.41: Pressure and friction coefficient curves for the DU 91-W2-250 airfoil with baseplate shape no.1 at angle of attack of a) 0 b) 5 degrees

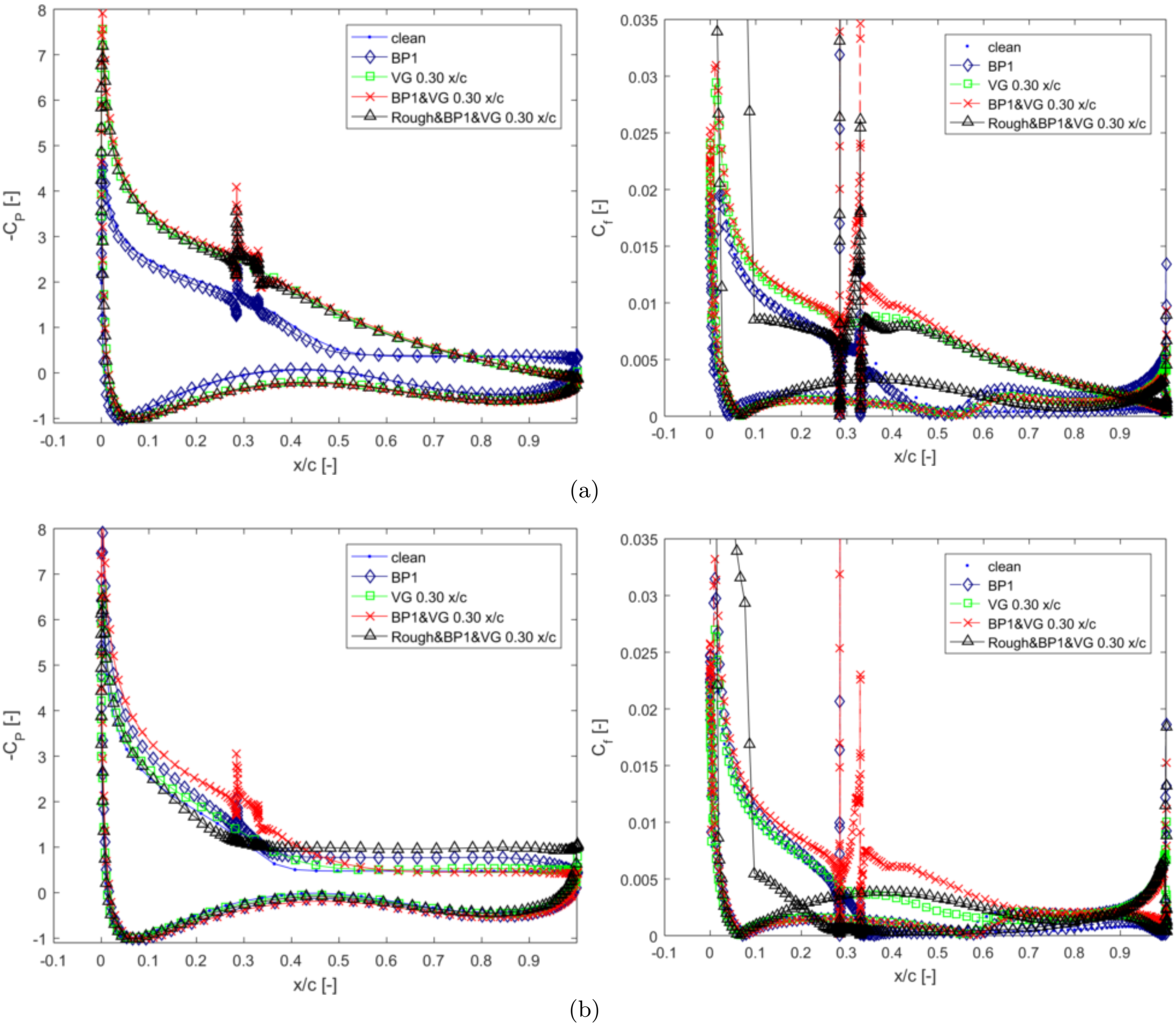

(a)

(b)

Figure 4.42: Pressure and friction coefficient curves for the DU 91-W2-250 airfoil with baseplate shape no.1 at angle of attack of a) 15 b) 20 degrees

4.3 Airfoils performance

Airfoil section with VGs are shown to be effective in delaying flow separation for both FFA W3-301 and DU 91-W2-250 airfoils. The maximum lift coefficient is increased from approximately 2 to 3 for FFA W3-301 airfoil with VGs at 0.20c and from approximately 1.6 to 2.3 for DU 91-W2-250 airfoil with VGs at 0.30c. However, the lift increase also results in additional drag due to the presence of the VGs as can be seen from table 4.9 where the airfoil section with VGs has a lower lift to drag ratio as compared to the clean airfoil. The aerodynamic efficiency (L/D ratio) decreases by approximately 33% for the FFA W3-301 airfoil with VGs at 0.20c and approximately 44% for the DU 91-W2-250 airfoil with VGs at 0.20c. By the moving VGs toward the trailing edge, aerodynamic efficiency is improved.

The effect of roughness on the airfoil is studied next. From these studies, the FFA W3-301 airfoil shows a dramatic loss in lift. By installing VGs on the rough airfoil, the maximum lift coefficient is regained from approximately 1.1 to 2.0 (VGs 0.20c) and the aerodynamic efficiency is improved by approximately 5%. Similar improvements can be seen on the DU 91-W2-250 airfoil. The maximum lift is increased from approximately 1.2 to 1.8 (VGs 0.20c) and aerodynamic efficiency is recovered by approximately 4.6%.

It seems that by adding a baseplate (except shape no.2) into the model, maximum lift and aerodynamic efficiency are slightly improved in both airfoils. The maximum lift coefficient is improved from approximately 1.96 to 2.11 for the FFA W3-301 with baseplate shape no.3 and VGs at 0.25c and the aerodynamic efficiency is increased by approximately 5%. Similarly for DU 91-W2-250 airfoil with baseplate shape no.1, the maximum lift coefficient is increased from around 1.88 to 2.27 and the aerodynamic efficiency is increased by approximately 6%. This could mean that for rough airfoils with VGs, the baseplate have accelerated the flow instead of obstructing it. However, baseplate shape no.2 fails to regain the flow from its separation in both airfoils.

	FFA W3-301			**DU 91-W2-250**		
	$\alpha_{CL_{max}}[deg]$	C_{Lmax}	$(\frac{C_L}{C_D})_{max}$	$\alpha_{CL_{max}}[deg]$	C_{Lmax}	$(\frac{C_L}{C_D})_{max}$
Clean	16.0	2.07	118.63	12.00	1.58	123.32
VGs 0.20c	24.0	3.13	85.56	16.00	2.23	78.65
VGs 0.25c	22.0	2.95	92.67	-	-	-
VGs 0.30c	20.0	2.75	99.77	17.00	2.34	84.99
VGs & BP1	20.0	2.76	110.99	17.00	2.44	87.45
VGs & BP2	14.0	2.19	103.09	12.00	1.87	72.44
VGs & BP3	18.0	2.53	105.25	17.00	2.37	80.19
VGs & BP4	20.0	2.74	89.80	15.00	2.18	97.05
VGs & BP5	22.0	2.94	90.27	17.00	2.41	89.14
Rough	12.0	1.13	41.43	10.00	1.23	52.93
VGs 0.20c&Rough	16.0	1.96	46.87	14.00	1.80	54.30
VGs 0.25c&Rough	16.0	1.96	46.87	-	-	-
VGs 0.30c&Rough	14.0	1.79	50.58	15.00	1.88	56.05
VGs&BP1&Rough	16.0	2.08	52.19	17.00	2.27	62.66
VGs&BP2&Rough	12.0	1.61	49.86	14.00	2.07	61.41
VGs&BP3&Rough	16.0	2.11	52.20	15.00	1.97	56.88
VGs&BP4&Rough	16.0	1.94	48.29	14.00	2.04	61.84
VGs&BP5&Rough	16.0	1.94	48.54	16.00	2.09	61.54

Table 4.9: Overall performance of FFA W3-301 (VGs at 0.25c) and DU 91-W2-250 (VGs at 0.30c) airfoils from the simulation

CHAPTER 5 Conclusion

The main objective of this research was to identify the effect of the baseplate of the vortex generators by comparing the simulation against experimental results. The main objective was accomplished by carried out the following tasks. Firstly, the baseplate configurations was added into the computational model. Five baseplate configurations were successfully implemented into the computational airfoil model. The simulations were performed on FFA W3-301 and DU 91 W2-250 airfoils in order to identify the effect of the baseplates.

Effect of the baseplate to the flow field was one of the main question of this research in order to analyze that series of studies had been performed.

From the results of the baseplate on the flow field we can conclude that the airfoil with baseplate (without VGs) had slightly lower maximum lift and higher drag coefficients. The airfoil with baseplate shape no.2 showed the lowest maximum lift and higher drag coefficients compared with other configurations. The drag coefficient curves of the airfoils with baseplate were higher than the simulated clean airfoil and higher than the experimental results for DU 91-W2-250 airfoil.

Next airfoil section with baseplate and VGs were studied. It seems that the presence of baseplate had negatively affected to the maximum lift in both FFA W3-301 and DU 91-W2-250 airfoils with VGs configurations. Severe reductions in the lift coefficients were found on the airfoil section with baseplate shape no.2 in both airfoils. Both FFA W3-301 and DU 91-W2-250 airfoils with baseplate shape no.5 showed a good agreement with the results from the airfoil with only VGs. Also, for the DU 91-W2-250 airfoil baseplate shapes no. 1 and 3 were in good agreement with the airfoil configuration with only VGs. From the results of this study, it was shown that the results of the simulations with baseplate shape no.5 most closely matched the results of simulations performed without a baseplate.

The effect of the Reynolds numbers to the airfoil was studied. From the results of the both FFA W3-301 and DU 91-W2-250 airfoils with VGs, the maximum lift coefficients were remained the same as the Reynolds number increased and the drag coefficients slightly decreased.

The results from both airfoils with VGs and baseplate shape no.1 remained the same as the Reynolds number increased. Both FFA W3-301 and DU 92-W2-250 with VGs and baseplate shape no.2 showed that as the Reynolds number increased the flow separation was improved. The FFA W3-301 airfoil with baseplate shape no.5 showed a good agreement at low Reynolds number. However as the Reynolds number increased, it separated earlier and drag coefficients also increased. This could be as a result of high parasitic drag.

Two different baseplate heights ($0.667c \times 10^{-3}$ and $1.000c \times 10^{-3}$) were studied. For the airfoil without VGs, as the baseplate height increased, the maximum lift coefficients decreased and the drag coefficients increased. This effect was pronounced with the airfoil with baseplate shape no.2.

For the airfoil with VGs and baseplate, There was no effect of the height to the airfoil lift coefficient. However, the drag coefficients were increased in both airfoils. The FFA W3-301 airfoil with VGs&BP1 with the height of 1.000×10^{-3} showed the closest drag coefficient curve to the experimental result. This can be concluded that the baseplate height had small effect to the airfoil lift coefficient. However, it marginally affected to the drag coefficients.

In order to answer the second main question regarding to the importance of the baseplate in the wind turbine design process. The airfoil with baseplate was simulated with the roughness model. From the results of the airfoil with VGs&roughness, the rough airfoil lift loss could be restored by installing

VGs. The airfoil with VGs&roughness&baseplate (except shape no.2) had favorable effect to the rough airfoil performance. It seems that by adding a baseplate (except shape no.2) into the model, maximum lift and aerodynamic efficiency were slightly improved in both airfoils. This is because the baseplate might accelerate the flow. However, baseplate shape no.2 had failed to recover from the flow separation. This could mean that for rough airfoils with VGs, the baseplate had accelerated the flow instead of obstructing it. However, baseplate shape no.2 failed to regain the flow from its separation in both airfoils.

Annual energy production (AEP) was computed using rough airfoil data. From the results of the airfoil with roughness, the AEP had dramatically dropped when the blade had rough surface. By installing VGs, the rough airfoil AEP was regained by 10% and 5% for DU 91-W2-250 airfoil. Although, the AEP was improved by VGs, the maximum thrust was also increased by approximately 4% for FFA W3-301 airfoil and 7% for DU 91-W2-250 airfoil. Taking the baseplate (except shape no.2) into consideration, both the maximum lift and aerodynamic efficiency were slightly increased and result in increasing the AEP around 2% to 1% for FFA W3-301 airfoil and 2.5% to 3% for DU 91-W2-250 airfoil. For FFA W3-301 airfoil, the blade with rough airfoil and baseplate shape no.2 produced the least AEP compared with rough airfoil with only VGs and other baseplate configurations. It could be seen that the baseplate showed favourable effect to the rough blade. This could be as a result of the accelerating flow passing over the bevel of the baseplate. Besides, the resolution of the simulation results could be inadequate (4-5 degrees) to perform this analysis which might cause a small variation in the results. More simulations needed to be performed in order to obtain accurate results.

It could be seen from the simulation results that the baseplate shape no.2 had performed poorly in simulations with both airfoils, although the flow separation was seen to be delayed at higher Reynolds numbers. However, due to the simplicity in manufacturing, this shape may still be used in practice and as such, it is highly recommended that the baseplate configuration is taken into accounted during the design process. This research has shown that it is advantageous to have baseplates with a smooth bevel likes baseplate shape no.1 and 5 in order to avoid unexpected flow separation. The effect of the baseplate could also be more important to account for in simulations as the height of the baseplate might increase in the future, if a larger VG is needed.

APPENDIX A Governing Equations

The capabilities of numerical analysis are ever increasing. Many in-house and commercial CFD solvers have emerged in the hope of better solving aerodynamic problems. EllipSys3D solver is one such example from the work of Michelsen and Sørensen [27] [34].

A.1 Flow Solver (EllipSys3D)

EllipSys3D solver is based on the incompressible Reynolds Averaged Navier-Stokes equation (RANS). This in-house solver allows a user to perform calculations required to simulate the interaction between a fluid and an object. The flow field is modeled using turbulence models, transition models, or roughness models.

A.1.1 Reynolds Averaged Navier-Stokes

The fundamental principle for a CFD is to solve a Newtonian fluid using Navier-Strokes equation. The equation is composed of inertial forces, pressure forces, viscous forces, and external forces applied to the fluid. The latter part is generally equal to zero for the natural flow. For an incompressible fluid, the continuity equation is:

$$\frac{\partial \bar{u}_i}{\partial x_i} = 0 \tag{A.1}$$

A Newtonian fluid could be described by Navier-Stokes equation:

$$\rho(\frac{\partial u_i}{\partial t} + u_j \frac{\partial u_i}{\partial x_j}) = \rho g_i + \frac{\partial \sigma_{ij}}{x_j} \tag{A.2}$$

where the stress of the fluid (σ_{ij}) is given as

$$\sigma_{ij} = -p\delta_{ij} + \mu(\frac{\partial u_i}{\partial x_j} + \frac{\partial u_j}{\partial x_i}) \tag{A.3}$$

inserting equation A.3 into equation A.2 and averaging each term gives

$$\rho(\frac{\partial \bar{u}_i}{\partial t} + \bar{u}_j \frac{\partial \bar{u}_i}{\partial x_j}) = \rho \bar{g}_i + \frac{\partial}{\partial x_j}(-\bar{p}\delta_{ij} + \mu(\frac{\partial \bar{u}_i}{\partial x_j} + \frac{\partial \bar{u}_j}{\partial x_i})) - \rho \bar{u_i' u_j'} \tag{A.4}$$

There are three equations of motion A.4 and a continuity equation (A.1) where there are ten unknowns. The problem is called the closure problem. In order to remedy the problem, a number of turbulence models can be applied. Examples of turbulence models are Algebraic models, Turbulence-energy equation models, and Simulation models.

A.2 Flow Models

In order to model the flowfield for difference flow regions, various flow models such as $k - \omega$ SST for turbulence model, and the e^N Method [9] for transitional flow are implemented. The following sub-section will describe each flow model individually.

A.2.1 Turbulence Model

A flow field can be discretized into three main regions namely Laminar, Turbulent, and Transition. For laminar flow, the Reynolds number for this regions is low and the flow is steady. In contrast to laminar flow, flow at high Reynolds number is categorized as in the turbulent region. The characteristics of the flow in this region has irregularity, diffusivity, large Reynolds numbers, three-dimensional vorticity fluctuations, dissipation and continuum [41]. In order to compute and analyze such a flow, a turbulence model needs to be implemented. One such model in the early development of turbulence modeling is the Mixing-Length model. The origin of this model is from the work of Boussinesq in 1887 [32]. He proposed a hypothesis stating that Reynolds stresses and the mean flow are related. Later on, Prandtl proposed the Mixing-length model, which is computationally inexpensive and simple. Although seen to be promising, the model cannot accurately compute a flow separation.

A.2.1.1 $k - \epsilon$ Turbulent Model

Turbulence model $k-\epsilon$ is one of the turbulence-energy equation models and it is a two-equations model. The model is governed by two main variables. The first one is for the turbulence kinetic energy k. The second one is the dissipation of the turbulence ϵ which determines the scale of the turbulence. Using mixing length model approach, one can connect the turbulence kinetic energy and the dissipation of the turbulence in term of eddy viscosity.

$$\mu_t = \rho C_\mu \frac{k^2}{\epsilon} \tag{A.5}$$

where C_μ is a dimensionless constant. The derivation of the turbulent kinetic energy equation starts with the RANS equation A.4 and one is multiplied by U_i and another one is multiplied by $\bar{u}_i$. Subtracting both equations and substituting turbulent kinetic energy (A.6) and rate of dissipation energy (A.7) equations.

$$k = \frac{1}{2}(\bar{u}'^2 + \bar{v}'^2 + \bar{w}'^2) \tag{A.6}$$

$$\epsilon = \frac{\nu}{2} \sum_{i,j} \overline{((\frac{\partial u_i'}{\partial x_j} + \frac{\partial u_j'}{\partial x_i})^2)} \tag{A.7}$$

This leads to the following turbulent kinetic energy equation.

$$\frac{\partial}{\partial t}(\rho k) + \frac{\partial}{\partial x_j}(\rho U_j k) - \frac{\partial}{\partial x_j}[(\mu + \frac{\mu_t}{\sigma_k})\frac{\partial k}{\partial x_j}] = \mu_t \frac{\partial U_i}{\partial x_j}(\frac{\partial U_i}{\partial x_j} + \frac{\partial U_j}{\partial x_i}) - \rho\epsilon \tag{A.8}$$

The dissipation of the turbulence energy equation is

$$\frac{\partial}{\partial t}(\rho \epsilon) + \frac{\partial}{\partial x_j}(\rho U_j \epsilon) - \frac{\partial}{\partial x_j}[(\mu + \frac{\mu_t}{\sigma_\epsilon})\frac{\partial \epsilon}{\partial x_j}] = C_{\epsilon 1}\frac{\epsilon}{k}\mu_t \frac{\partial U_i}{\partial x_j}(\frac{\partial U_i}{\partial x_j} + \frac{\partial U_j}{\partial x_i}) - \rho C_{\epsilon 2}\frac{\epsilon^2}{k} \tag{A.9}$$

As it is seen from equation A.8 and A.9, there are five constants $(C_\mu, \sigma_k, \sigma_\epsilon, C_{\epsilon 1}, C_{\epsilon 2})$, which are used to control the $k - \epsilon$ model. The model showed success in simulation of the unconfined flow cases [47]. However it has some disadvantages such as it fails to predict flow when the flow has high adverse pressure gradient [8] which is very crucial for this research as prolonging the linearity part of the lift curve is the goal for adding a VG. Failure to predict the adverse pressure gradient will raise the uncertainty in this research.

A.2.1.2 $k - \omega$ Turbulent Model

Wilcox proposed a new $k - \omega$ turbulent model [50] in order to overcome the aforementioned issue in $k-\epsilon$ turbulent model in 1988. The model has two main variables. The first parameter is the turbulence kinetic energy k. The second parameter is the turbulence specific dissipation ω. The full derivation of this model can be found in Wilcox's original literature [50]. The turbulent mixing energy equation is as follows.

$$\frac{\partial}{\partial t}(\rho k) + \frac{\partial}{\partial x_j}(\rho U_j k) - \frac{\partial}{\partial x_j}[(\mu + \sigma_k \mu_t)\frac{\partial k}{\partial x_j}] = \tau_{ij}\frac{\partial U_i}{\partial x_j} - \beta^* \rho \omega k \tag{A.10}$$

The specific dissipation rate of turbulence energy equation is

$$\frac{\partial}{\partial t}(\rho \omega) + \frac{\partial}{\partial x_j}(\rho U_j \omega) - \frac{\partial}{\partial x_j}[(\mu + \sigma_\omega \mu_t)\frac{\partial \omega}{\partial x_j}] = \frac{\gamma}{\nu_t}\tau_{ij}\frac{\partial U_i}{\partial x_j} - \beta \rho \omega^2 \tag{A.11}$$

where

$$\omega = \frac{\epsilon}{k\beta^*} \tag{A.12}$$

This model bypasses the adverse pressure gradient problem. However, the model introduces another limitation, which is the farfield dissipation dependency. Therefore the new baseline model is introduced by Menter [26] to improve on Wilcox's $k - \omega$ turbulent model.

A.2.1.3 BSL $k - \omega$ Turbulent Model

The BSL $k - \omega$ Turbulent model [26] was intended to combine two turbulence models ($k - \omega$ and $k - \epsilon$). The novelty of this method is that, the $k - \omega$ model will resolve the simulation in the viscous sub-layer. Then the equation will be manipulated with a blending function such that it will become the standard $k - \epsilon$ model to solve the flow field in the outer wake region. This method could be done by adding a term with the blending function into the original specific rate of turbulence energy equation (A.11).

$$\frac{\partial}{\partial t}(\rho \omega) + \frac{\partial}{\partial x_j}(\rho U_j \omega) - \frac{\partial}{\partial x_j}[(\mu + \sigma_\omega \mu_t)\frac{\partial \omega}{\partial x_j}] = \frac{\gamma}{\nu_t}\tau_{ij}\frac{\partial U_i}{\partial x_j} - \beta \rho \omega^2 + 2\rho(1 - F_1)\frac{\sigma_{\omega 2}}{\omega}\frac{\partial k}{\partial x_j}\frac{\partial \omega}{\partial x_j} \tag{A.13}$$

The blending function (F_1) in the last term of the equation (A.13) is equal to one for the boundary layer in order to maintain the original $k - \omega$ turbulence model and becomes zero for the outer wake region.

A.2.1.4 $k - \omega$ SST model

Shear-Stress Transport (SST) model is used for improving results for highly adverse pressure gradient flow which is very important for flow separation prediction. Previous turbulence models used the Boussinesq approximation in order to express Reynolds stresses in term of eddy viscosity. This technique is practical but it has not taken the nature of the transportiveness of the Reynolds stresses into account. The Reynolds stresses is derived from the left-hand side of the Navier-Stokes equation and is due to the fluid momentum exchanges. This means that Reynolds stresses can be transported. In order to take transportiveness of Reynolds stresses into account, the eddy-viscosity is modified. This model is an extension of $k - \omega$ model by the work of Menter [26] and is used throughout this research.

A.2.2 Transition Model

The flow between Laminar and Turbulent regions is called Transition. In this region, the flow is partly steady and unsteady. In order to accurately predict the flow separation on the airfoil section, a transition model also needs to be implemented. The e^N method is used throughout this research and it is developed by Drela and Giles [9]. This transition model is implemented in EllipSys3D as described by Michelsen [27] and can be controlled by changing parameter N. Validation of appropriate N value will be done on the clean airfoil. The N value that gives the closest lift and drag force to the experimental results will be used in the further study' portions.

The N value can also be computed from turbulence intensity (TI) using following equation from Mack [23]:

$$N = -8.43 - 2.4ln(TI) \tag{A.14}$$

A.2.3 Roughness Model

Roughness model is also another parameter that will be studied and validated against experimental results. The rough airfoil surface will trip the flow from laminar to turbulence and as a consequence, the airfoil will suddenly lose lift. The roughness model that is used in this research is based on the work of Knopp [11] and it could be achieved by changing the boundary condition at the wall in $k-\omega$ turbulence model. The leading edge of the airfoil will be covered with different types of a sand roughness in order to mimic the roughness that can be expected on a real wind turbine blade.

A.3 Numerical Scheme

Stagged grid is used in a common finite volume discretization. Variables such as velocities are store on the cell faces, whereas pressure is kept at the center of the control volume. This method is widely used as it is robust and can prevent odd-even decoupling between pressure and velocity. Semi-Implicit Method for Pressure-Linked Equations (SIMPLE) procedure [29] is used for the iterative solvers. Velocity is solved explicitly, whereas pressure will be calculated using the solution from the previous iteration. In order to solve convected velocities in the convective term of finite-volume equation, appropriate differencing schemes are applied. Common difference schemes such as Central differencing scheme (CDS) or Upwind differencing scheme (UDS) cannot handle a highly convective problem ($Pe \rightarrow \infty$) or such a flow with highly adverse pressure gradient. Therefore, Quadratic Upstream Interpolation for Convective Kinematics (QUICK) is implemented in order to tackle the issue.

A.3.1 Central Differencing Scheme (CDS)

The CDS scheme is second-order accurate in terms of Taylor serie expansion. This scheme uses two neighboring stencils (upwind and downwind) in order to get the cell value. Both neighboring stencils are given as the same weight in the calculation. This method could lead to boundedness problem for the flow that is highly convective or as $Pe \rightarrow \infty$, since the scheme fails to reflect the transportiveness of the flow.

A.3.2 Upwind Differencing Scheme (UDS)

Upwind differencing scheme (UDS) can tackle boundedness problem. However, the scheme is only first-order accurate which has higher truncation error than the CDS scheme. Besides this, a false diffusion problem also arises in UDS scheme as the flow moves non-orthogonally through the fluid, which occurs in multidimensional flow.

A.3.3 Second-order Upwind Differencing Scheme (SUD)

For second-order upwind differencing scheme (SUD) two upstream stencils are interpolated instead of using only one as in UDS scheme. The SUD scheme is second-order accurate. A modification has been made in order to improve the original SUD scheme by Yeo et al.[52].

A.3.4 Quadratic Upstream Interpolation for Convective Kinematics (QUICK)

In order to achieve accuracy and convective stability, Quadratic Upstream Interpolation for Convective Kinematics (QUICK) by Leonard [20] is one of the schemes that fit the requirements. The scheme uses two stencils upstream and one stencil downstream to parabolically interpolate. The result of this scheme is third-order accuracy. This uses the same method as the SUD scheme [52] to overcome the growing number of stencils and numerical instability issues.

A.4 Pressure Equation

Momentum equations and the continuity equation are used to derive the equation for the pressure. Rhie/Chow interpolation [30] is used to avoid odd-even pressure decoupling. The method to compute pressure is as described in the SIMPLE procedure [29].

APPENDIX B Pressure & Friction

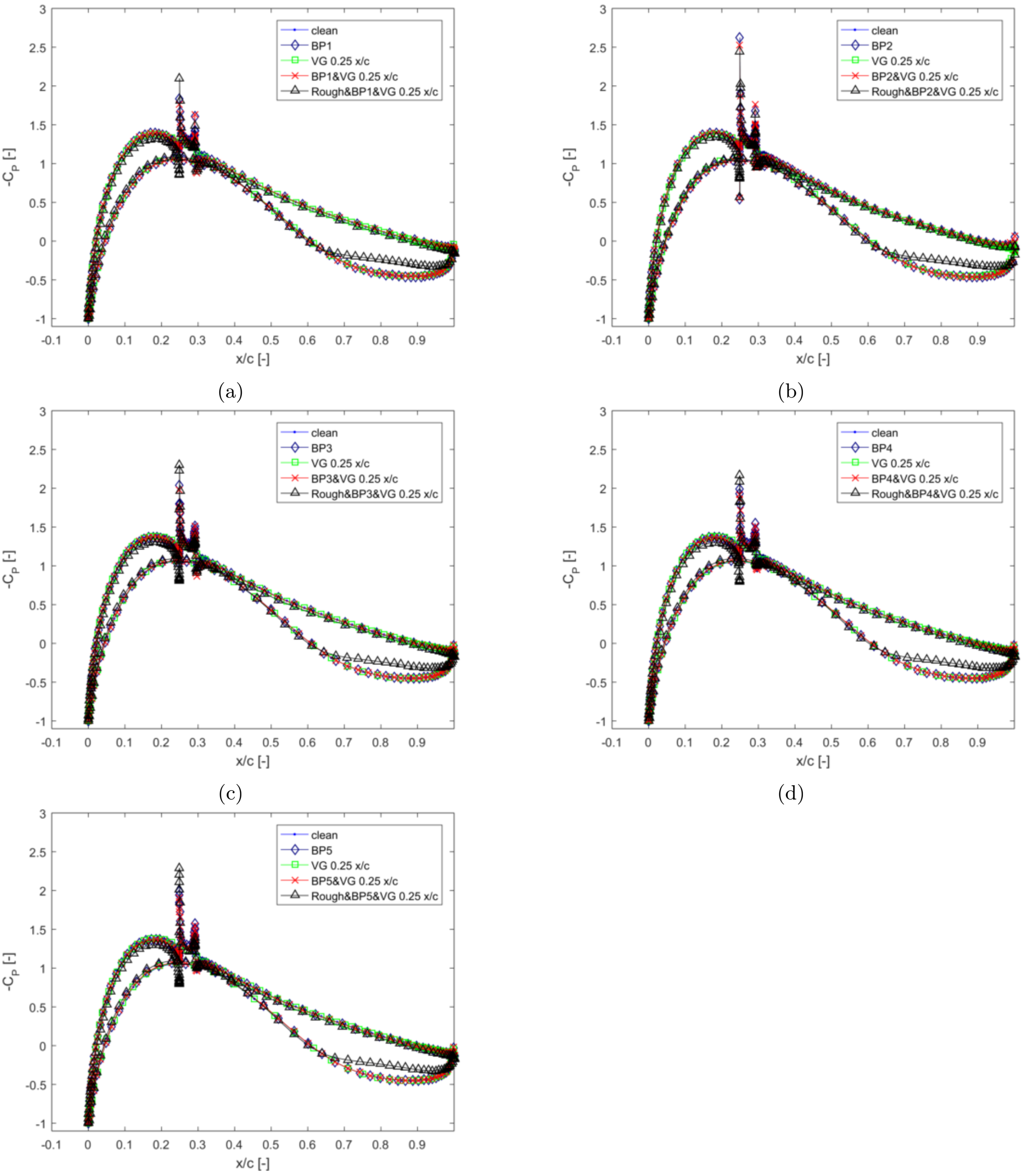

(a) (b) (c) (d) (e)

Figure B.1: Pressure coefficient curves for the FFA-W3-301 airfoil at AoA of 0 degree

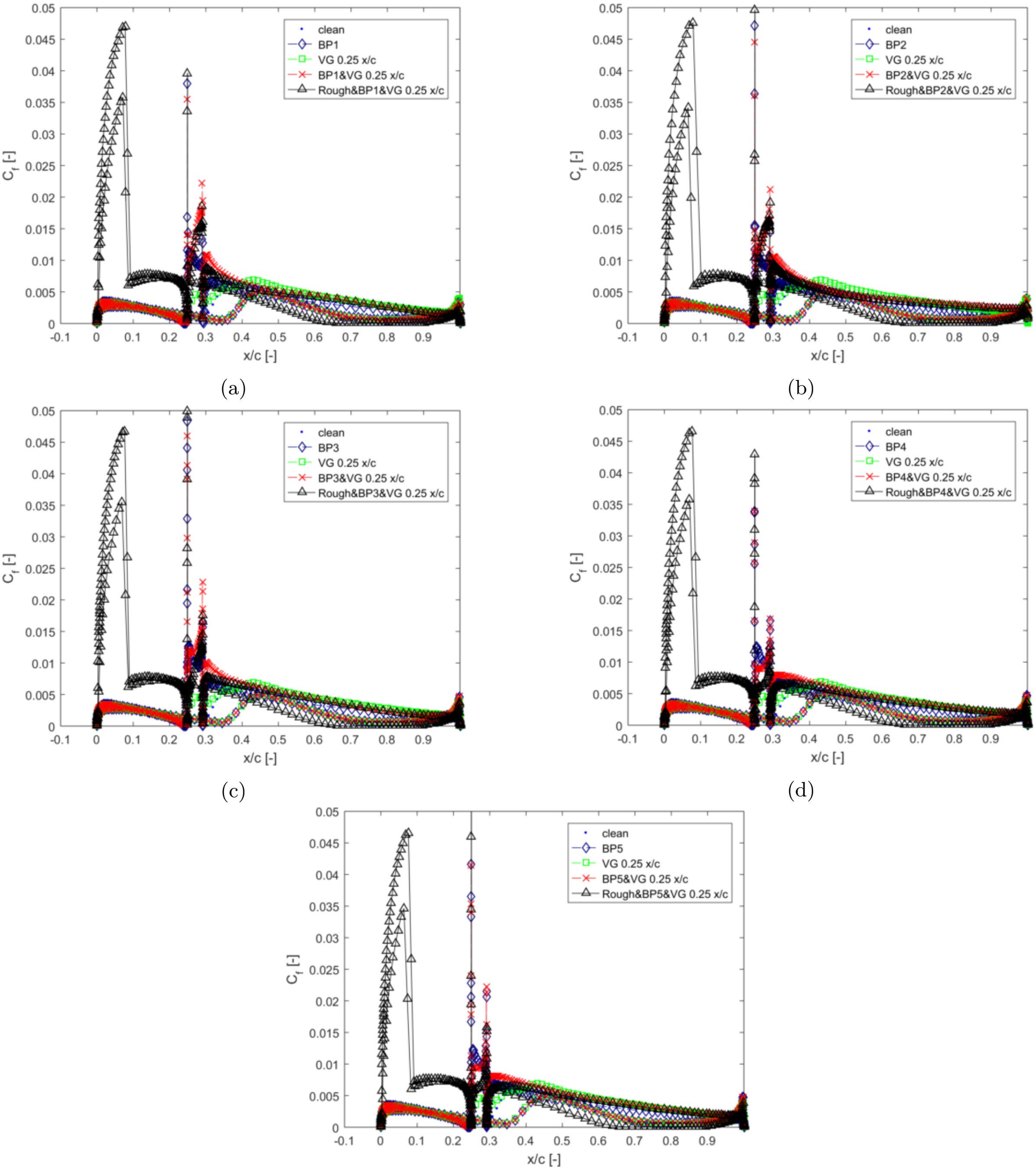

(a)

(b)

(c)

(d)

(e)

Figure B.2: Friction coefficient curves for the FFA-W3-301 airfoil at AoA of 0 degree

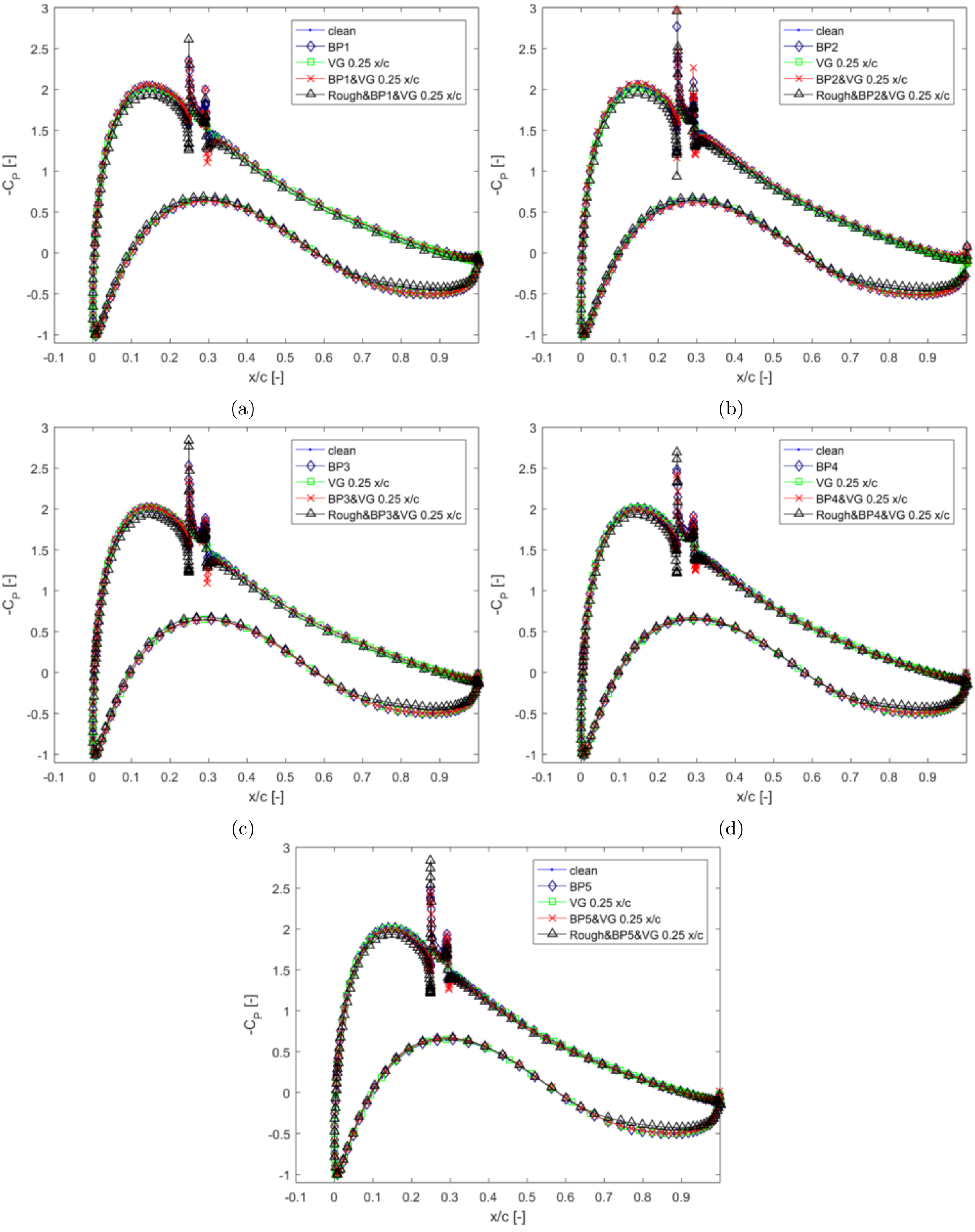

(a) (b) (c) (d) (e)

Figure B.3: Pressure coefficient curves for the FFA-W3-301 airfoil at AoA of 4 degrees

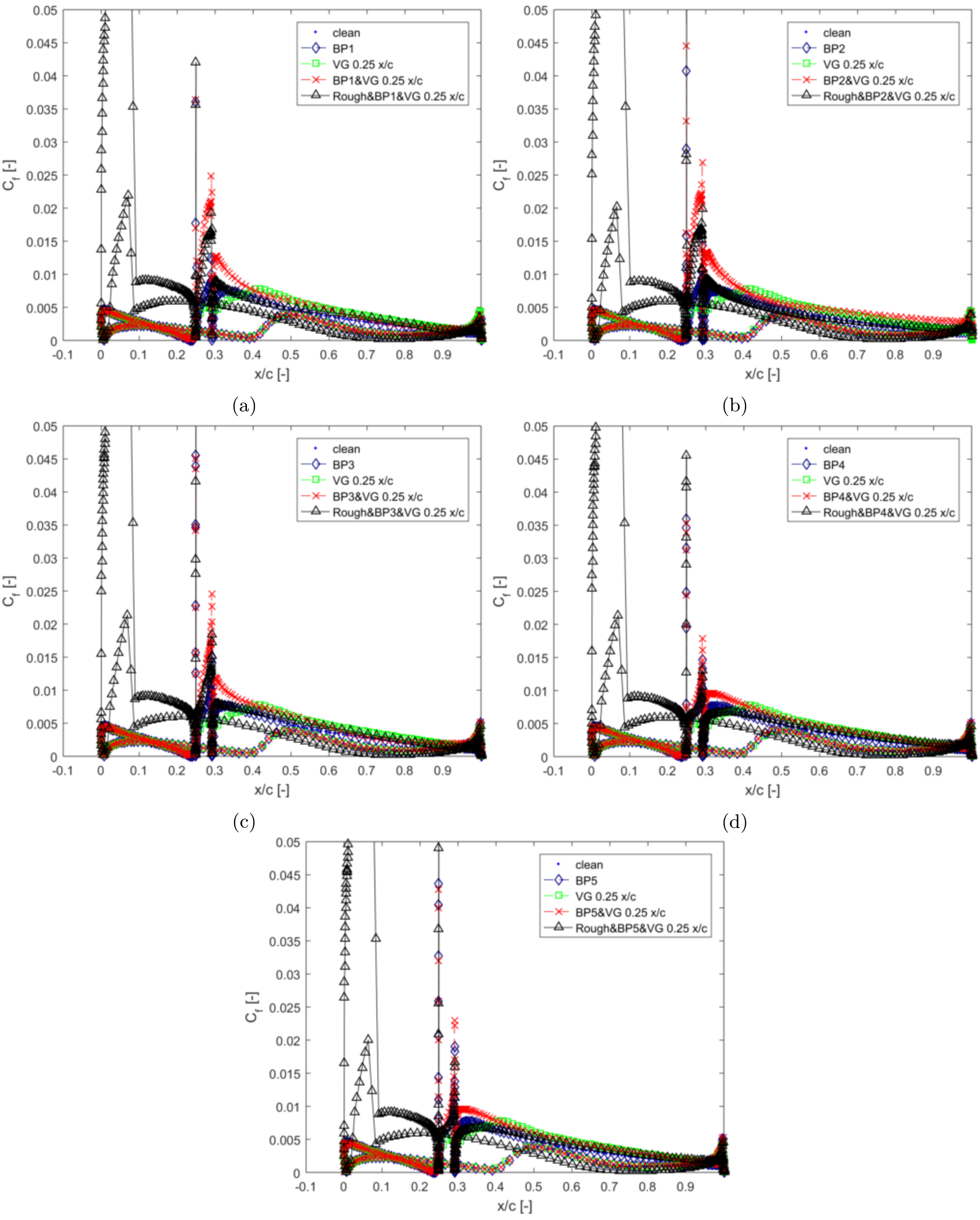

(a) (b)

(c) (d)

(e)

Figure B.4: Friction coefficient curves for the FFA-W3-301 airfoil at AoA of 4 degrees

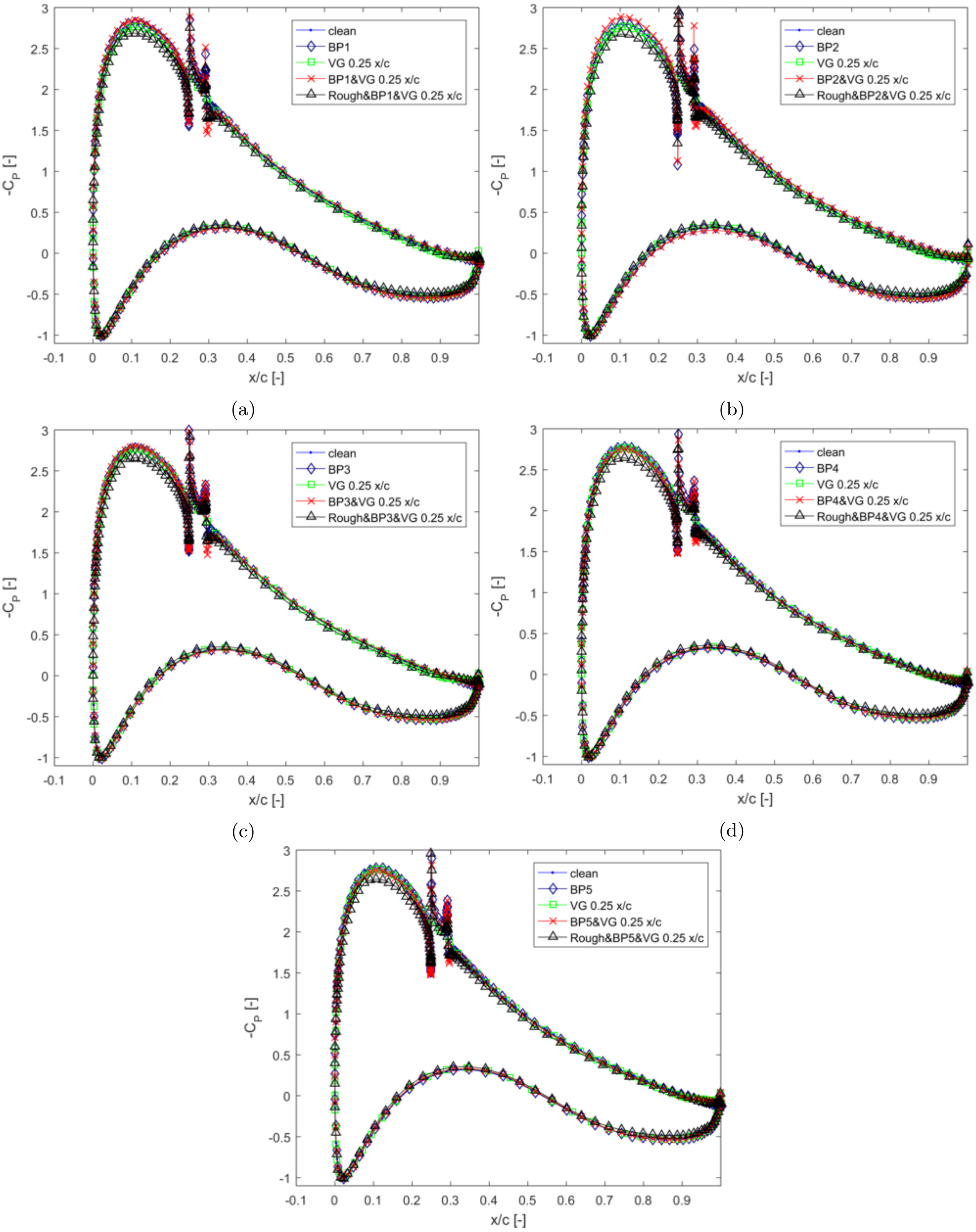

(a) (b) (c) (d) (e)

Figure B.5: Pressure coefficient curves for the FFA-W3-301 airfoil at AoA of 8 degrees

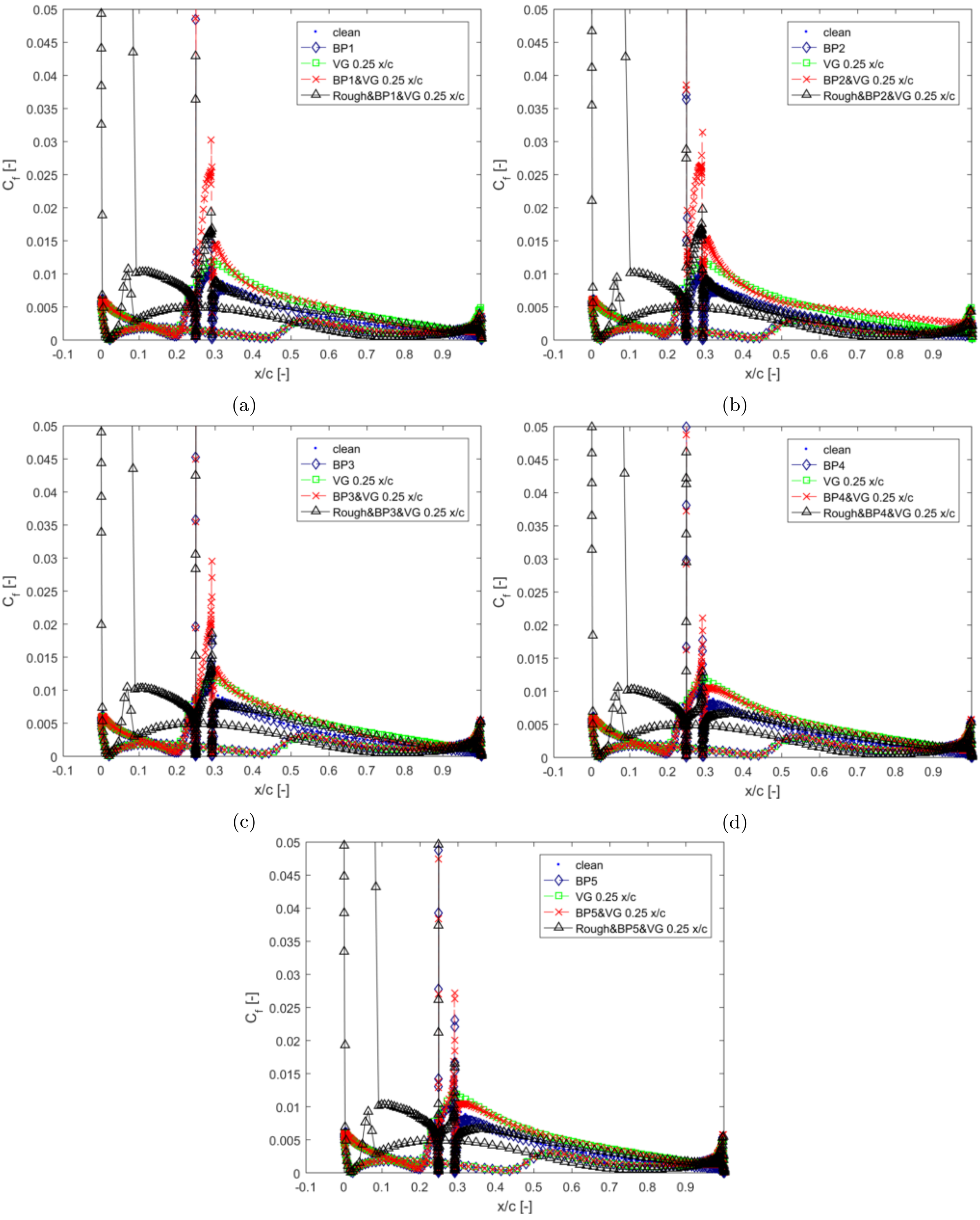

(a) (b)

(c) (d)

(e)

Figure B.6: Friction coefficient curves for the FFA-W3-301 airfoil at AoA of 8 degrees

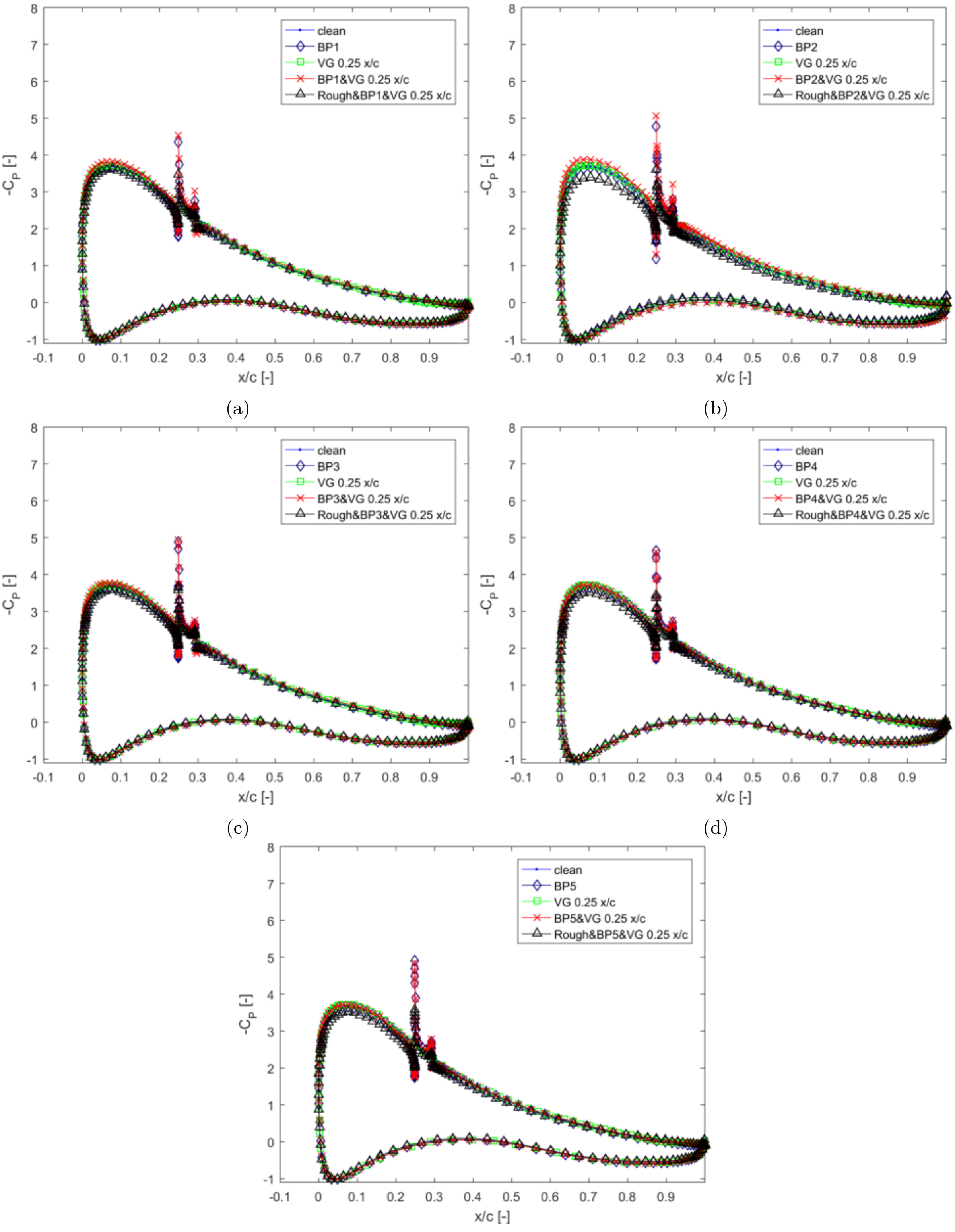

(a) (b) (c) (d) (e)

Figure B.7: Pressure coefficient curves for the FFA-W3-301 airfoil at AoA of 12 degrees

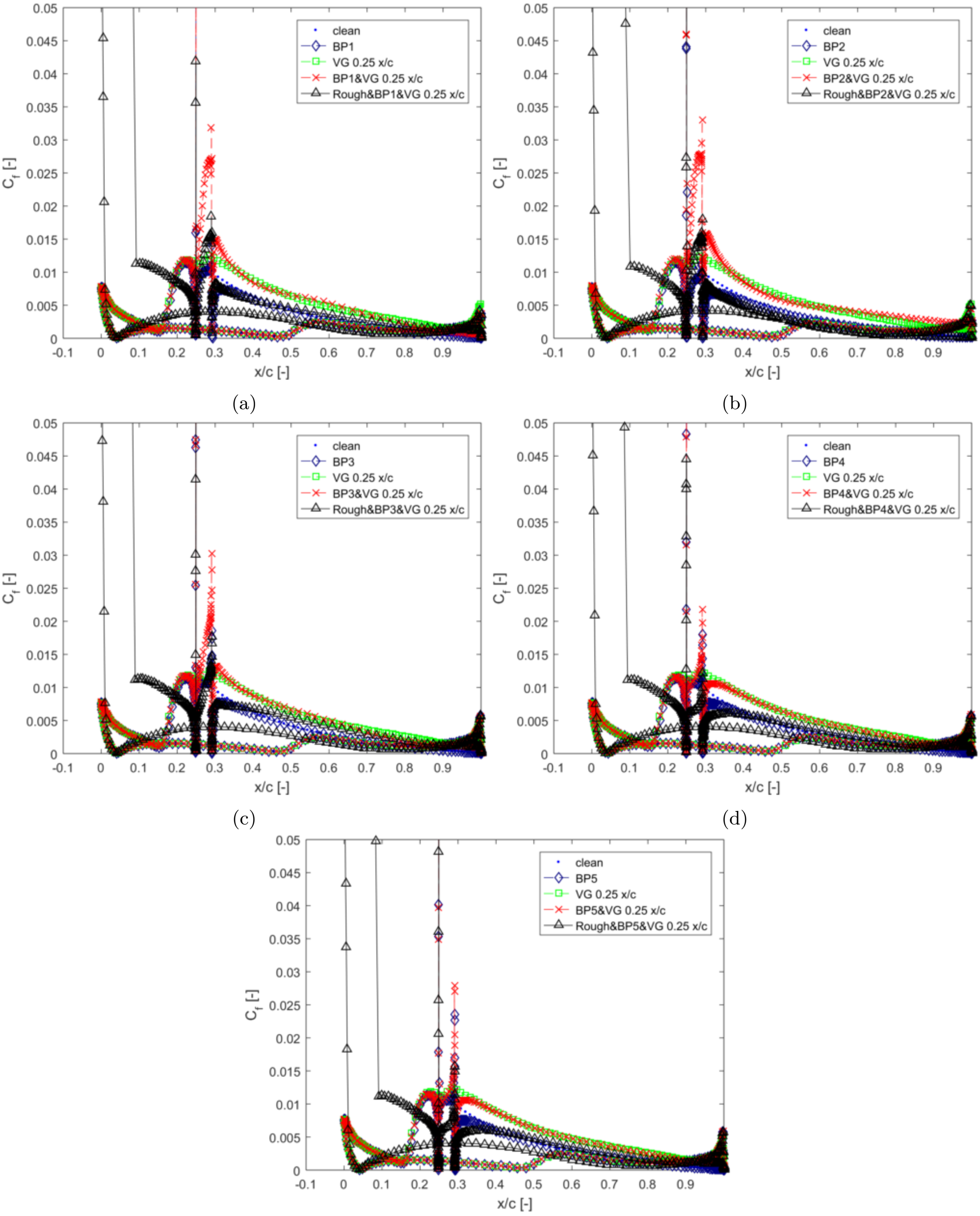

(a)

(b)

(c)

(d)

(e)

Figure B.8: Friction coefficient curves for the FFA-W3-301 airfoil at AoA of 12 degrees

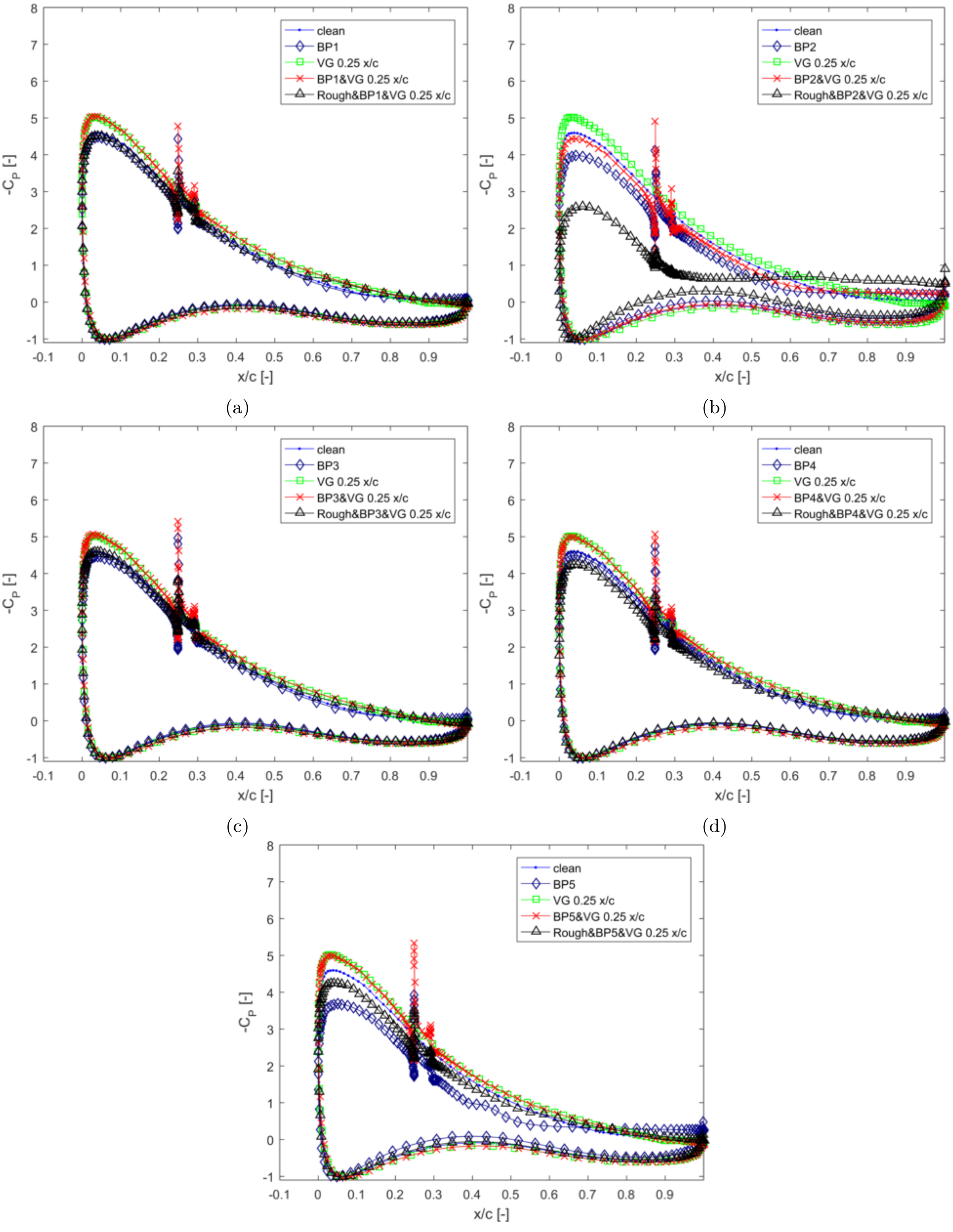

(a) (b) (c) (d) (e)

Figure B.9: Pressure coefficient curves for the FFA-W3-301 airfoil at AoA of 16 degrees

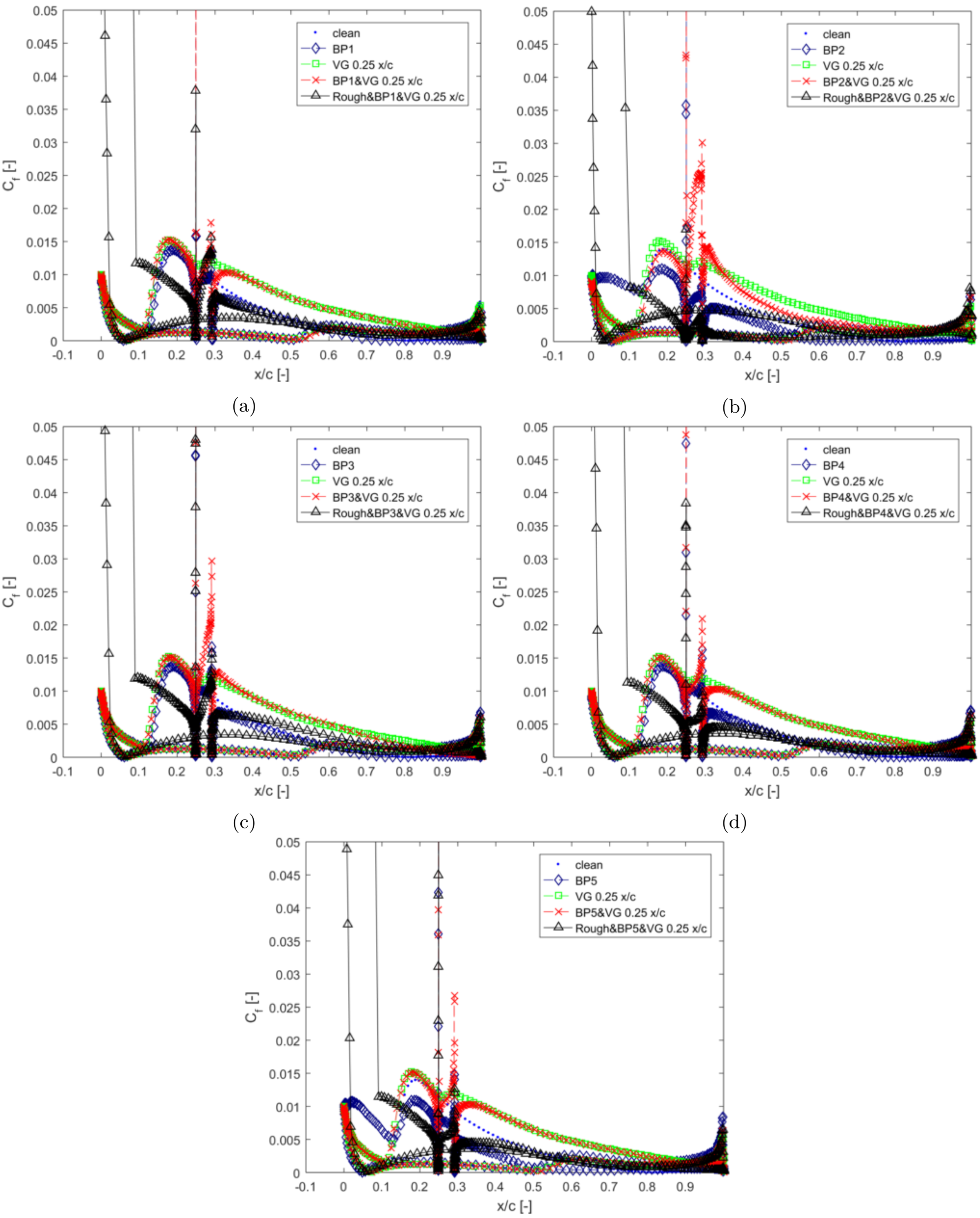

(a)

(b)

(c)

(d)

(e)

Figure B.10: Friction coefficient curves for the FFA-W3-301 airfoil at AoA of 16 degrees

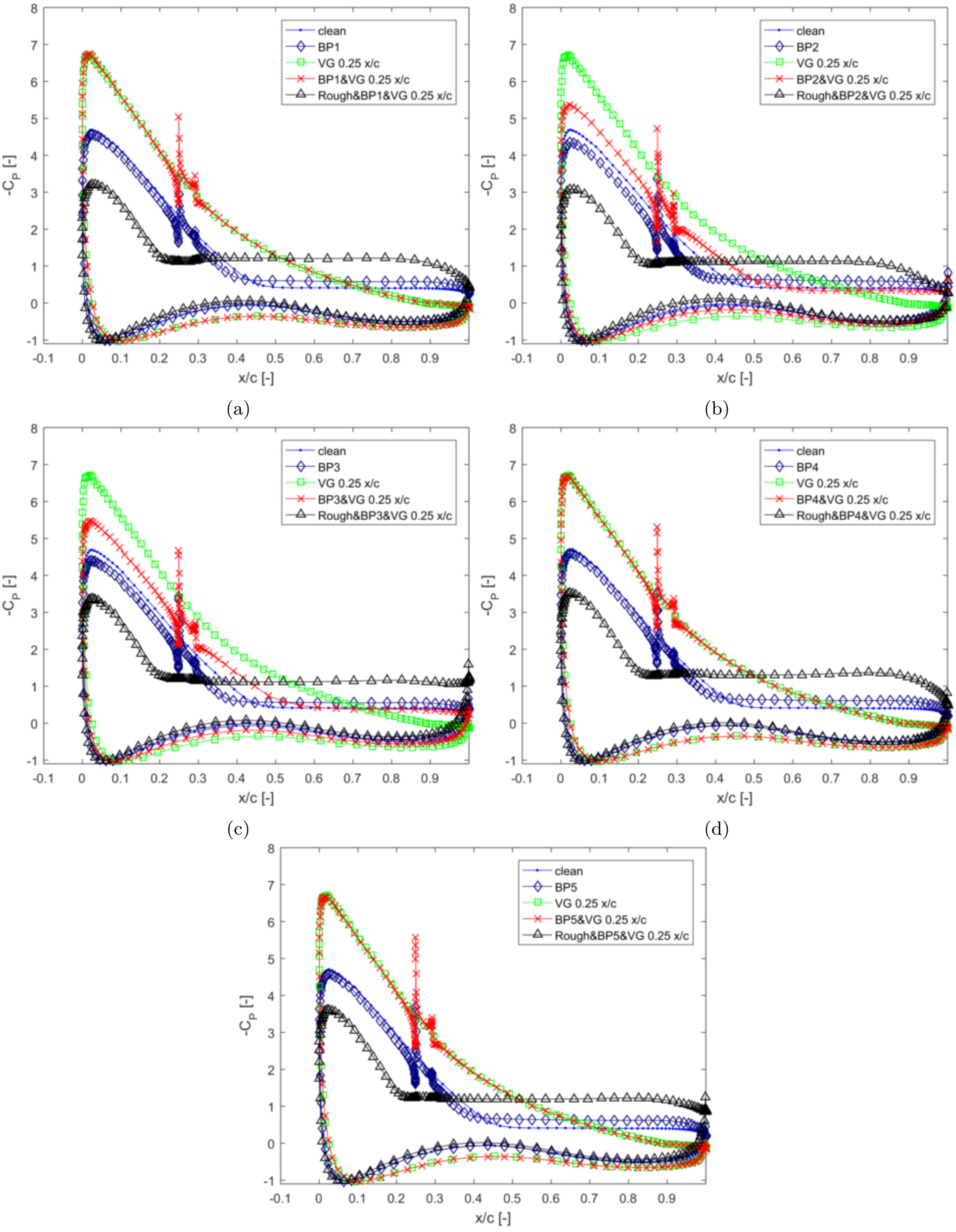

(a) (b) (c) (d) (e)

Figure B.11: Pressure coefficient curves for the FFA-W3-301 airfoil at AoA of 20 degrees

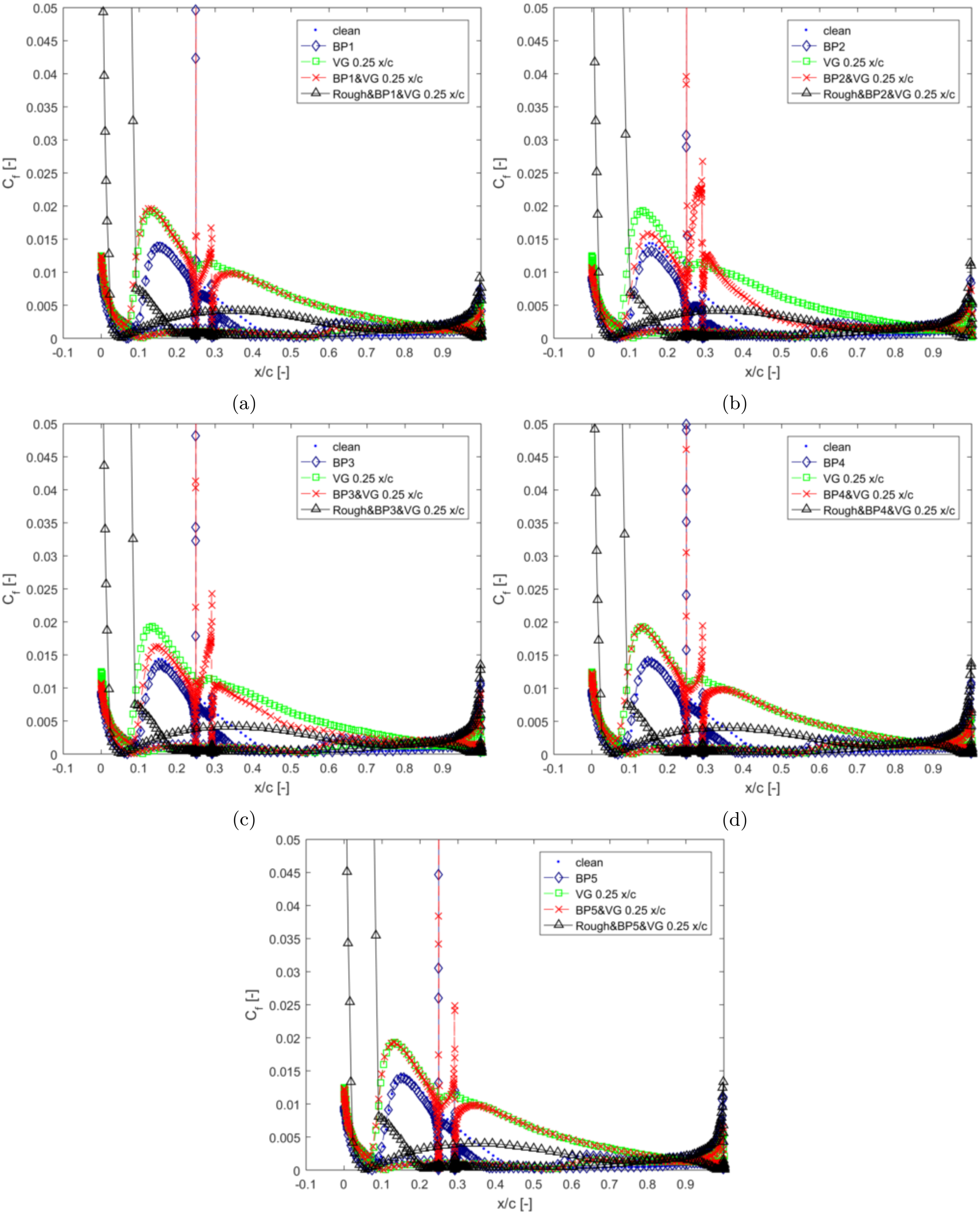

(a) (b) (c) (d) (e)

Figure B.12: Friction coefficient curves for the FFA-W3-301 airfoil at AoA of 20 degrees

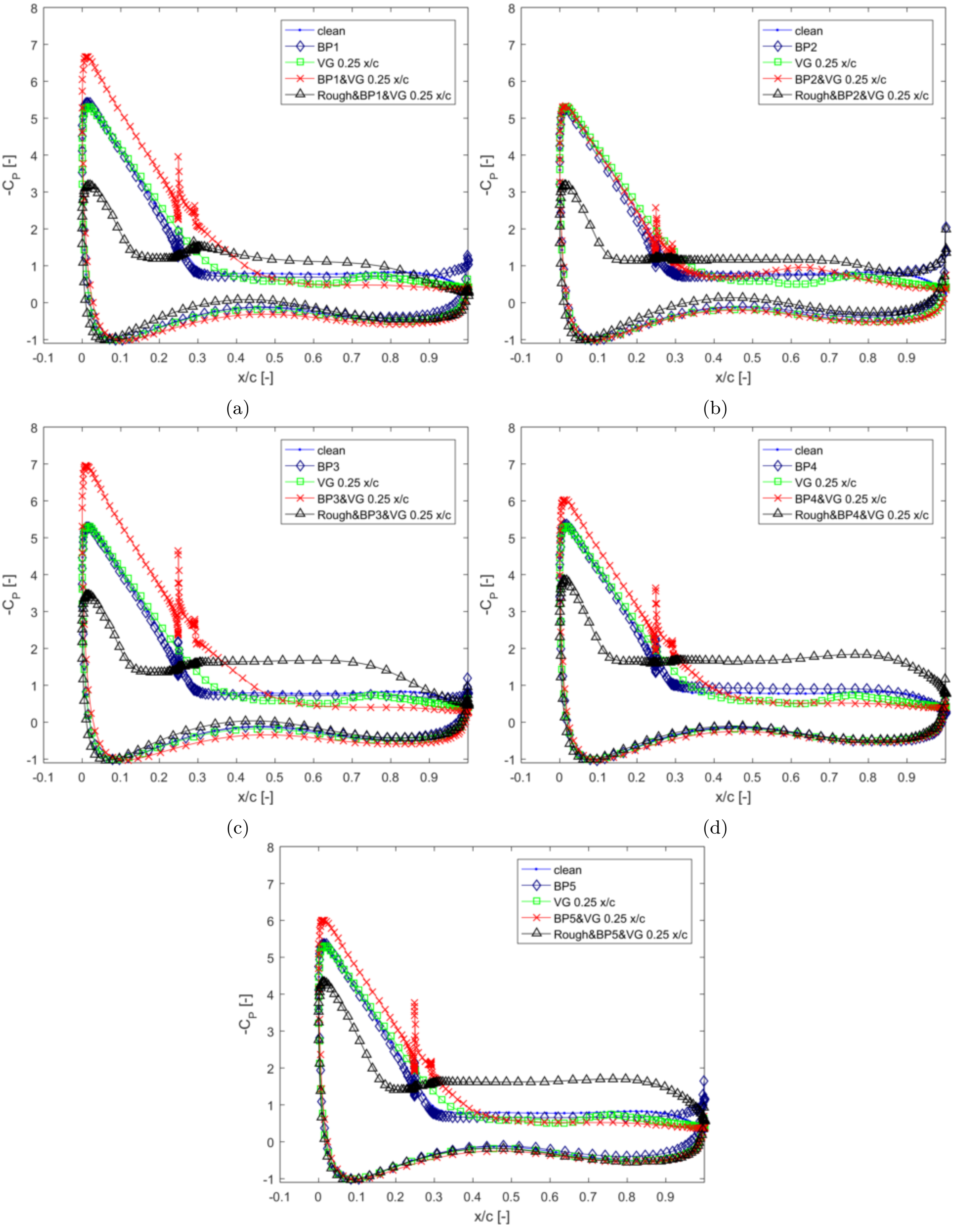

(a)

(b)

(c)

(d)

(e)

Figure B.13: Pressure coefficient curves for the FFA-W3-301 airfoil at AoA of 24 degrees

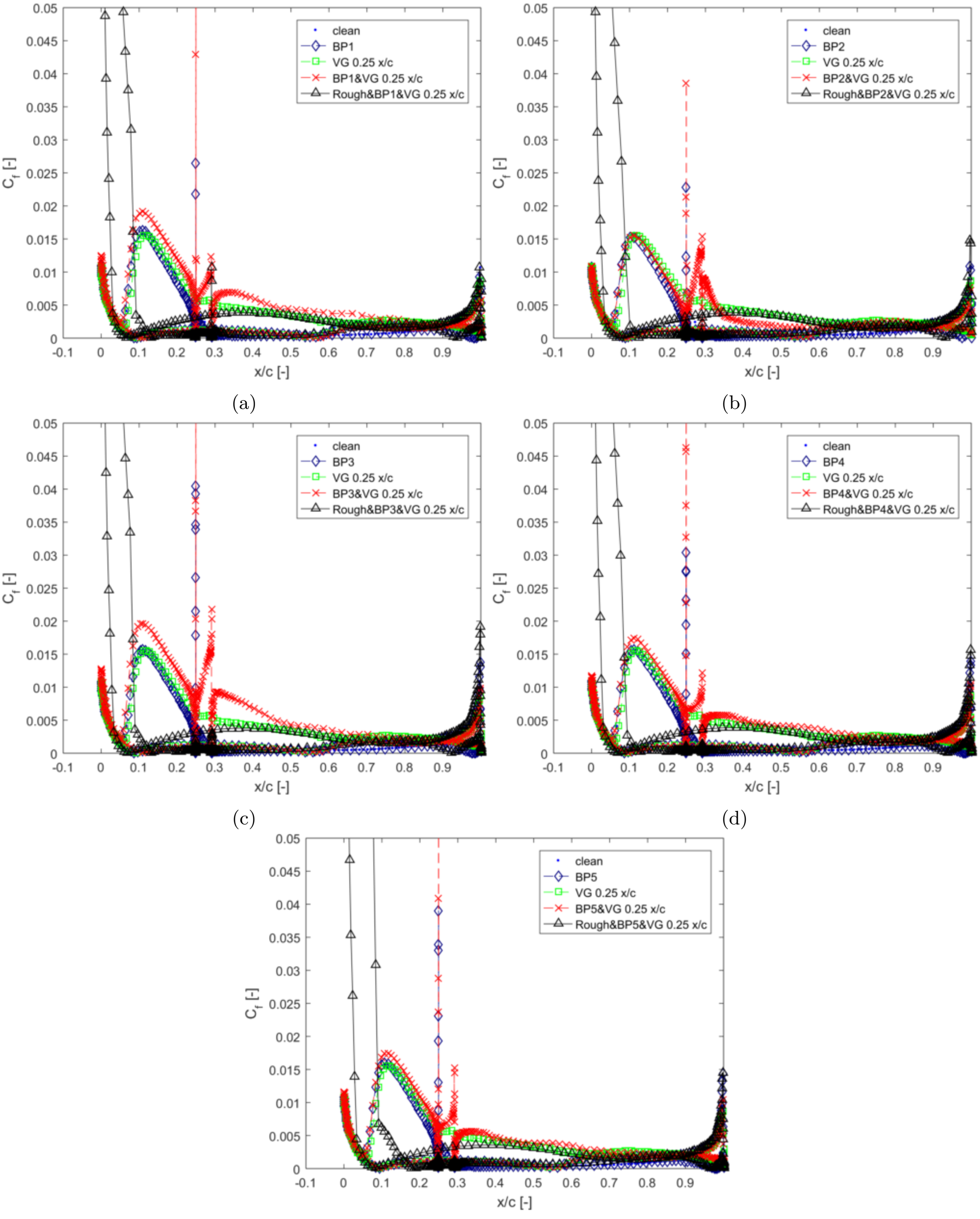

(a) (b) (c) (d) (e)

Figure B.14: Friction coefficient curves for the FFA-W3-301 airfoil at AoA of 24 degrees

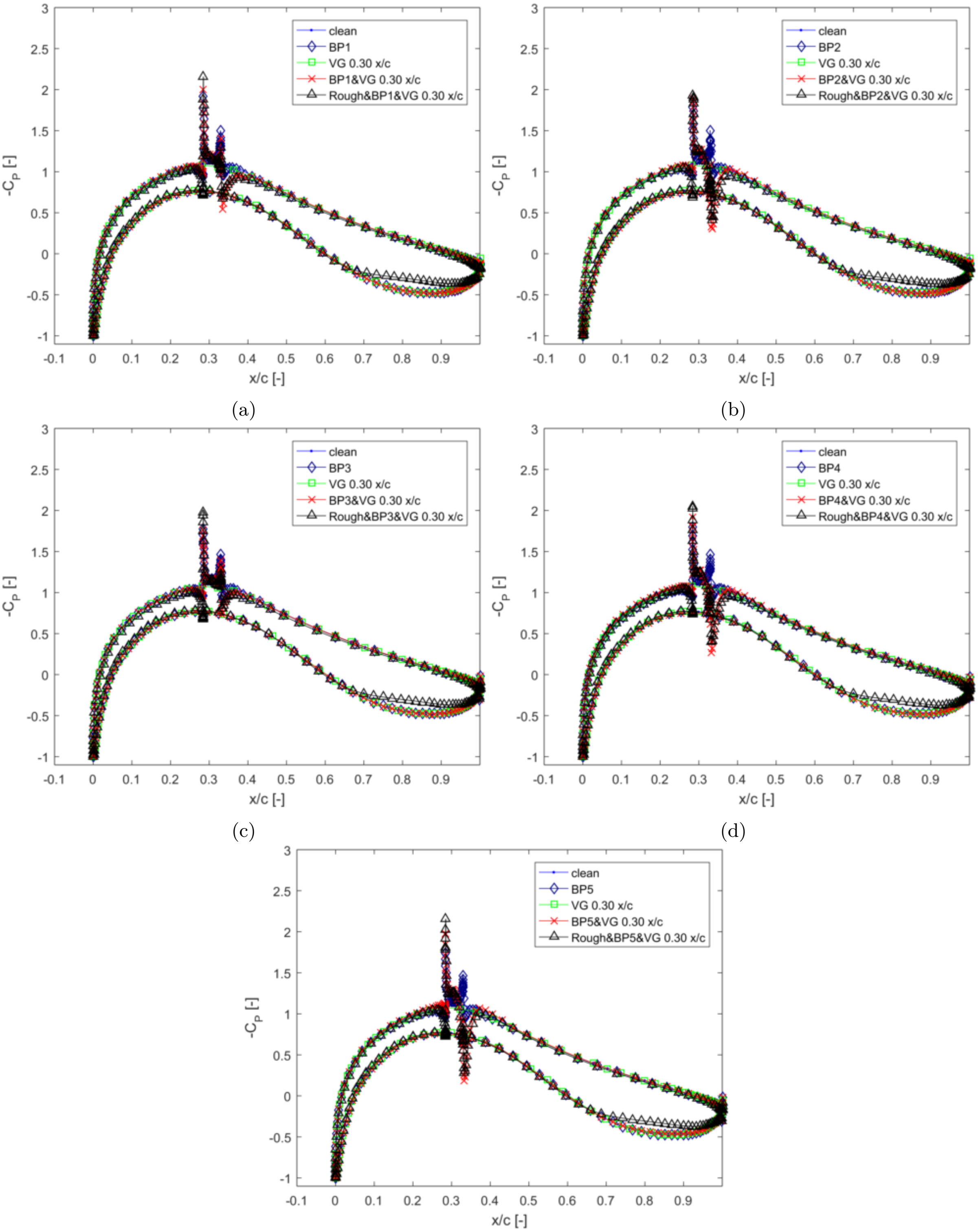

(a) (b) (c) (d) (e)

Figure B.15: Pressure coefficient curves for the DU 91-W2-250 airfoil at AoA of 0 degree

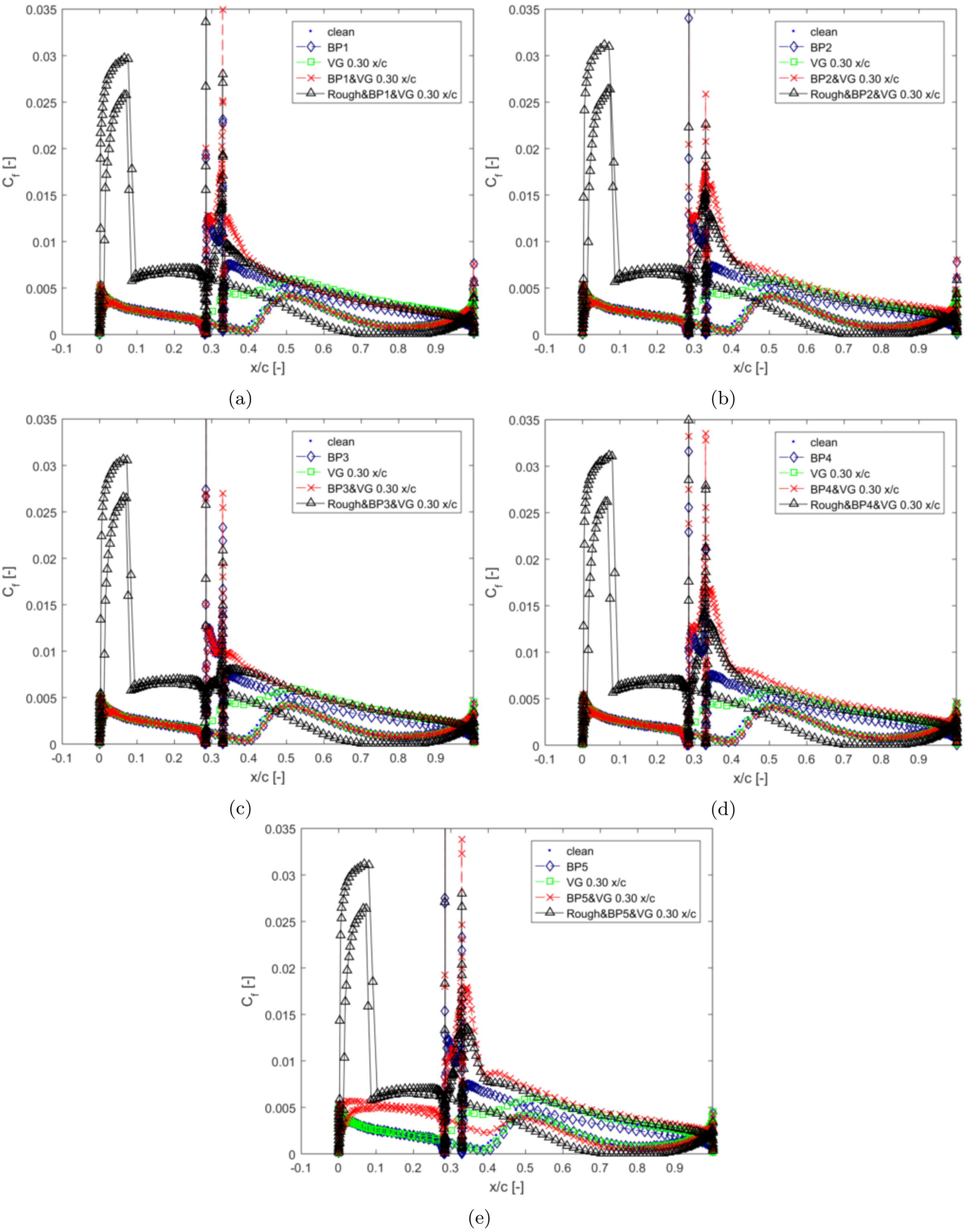

(a) (b)

(c) (d)

(e)

Figure B.16: Friction coefficient curves for the DU 91-W2-250 airfoil at AoA of 0 degree

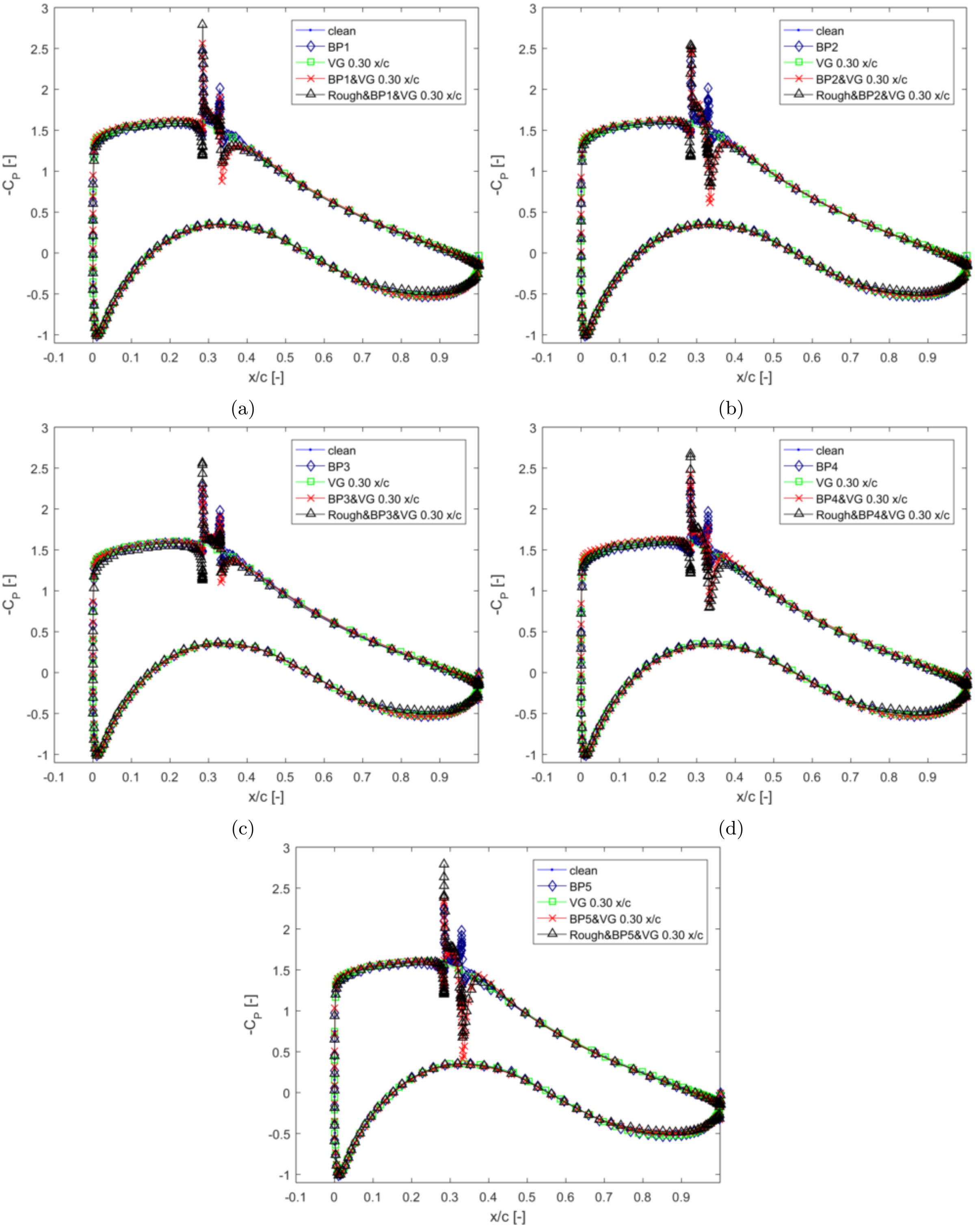

(a) (b)

(c) (d)

(e)

Figure B.17: Pressure coefficient curves for the DU 91-W2-250 airfoil at AoA of 5 degrees

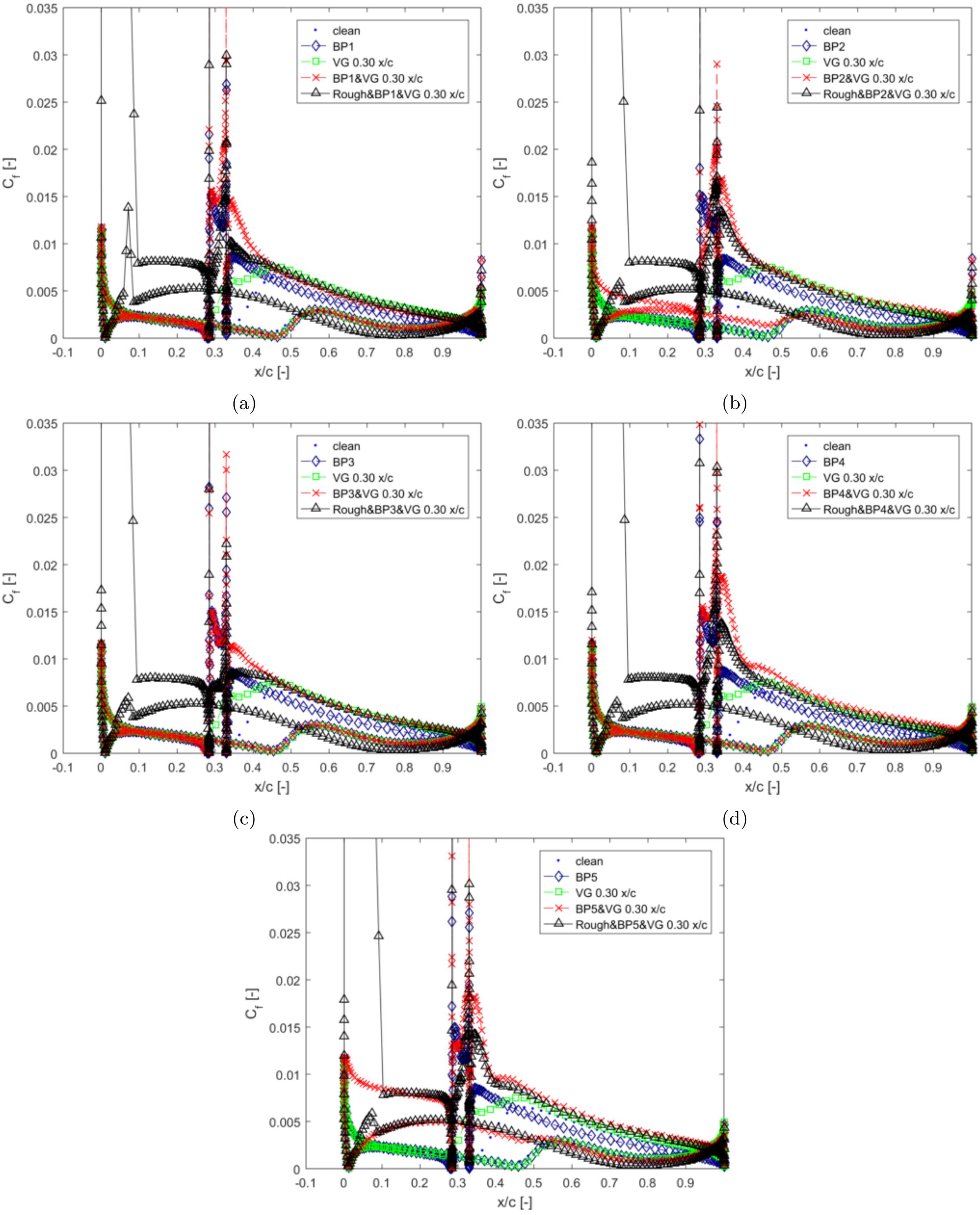

(a) (b) (c) (d) (e)

Figure B.18: Friction coefficient curves for the DU 91-W2-250 airfoil at AoA of 5 degrees

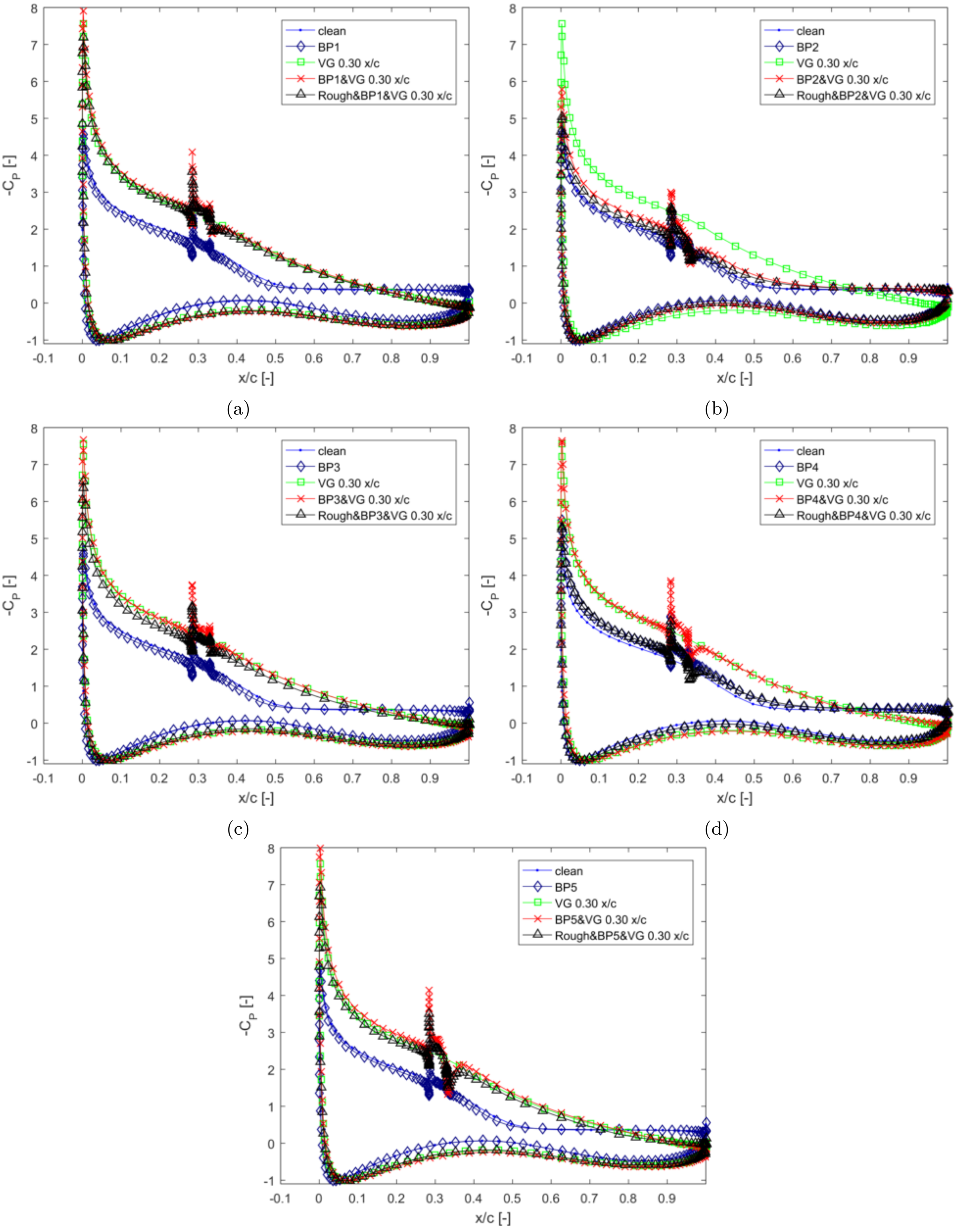

(a)

(b)

(c)

(d)

(e)

Figure B.19: Pressure coefficient curves for the DU 91-W2-250 airfoil at AoA of 15 degrees

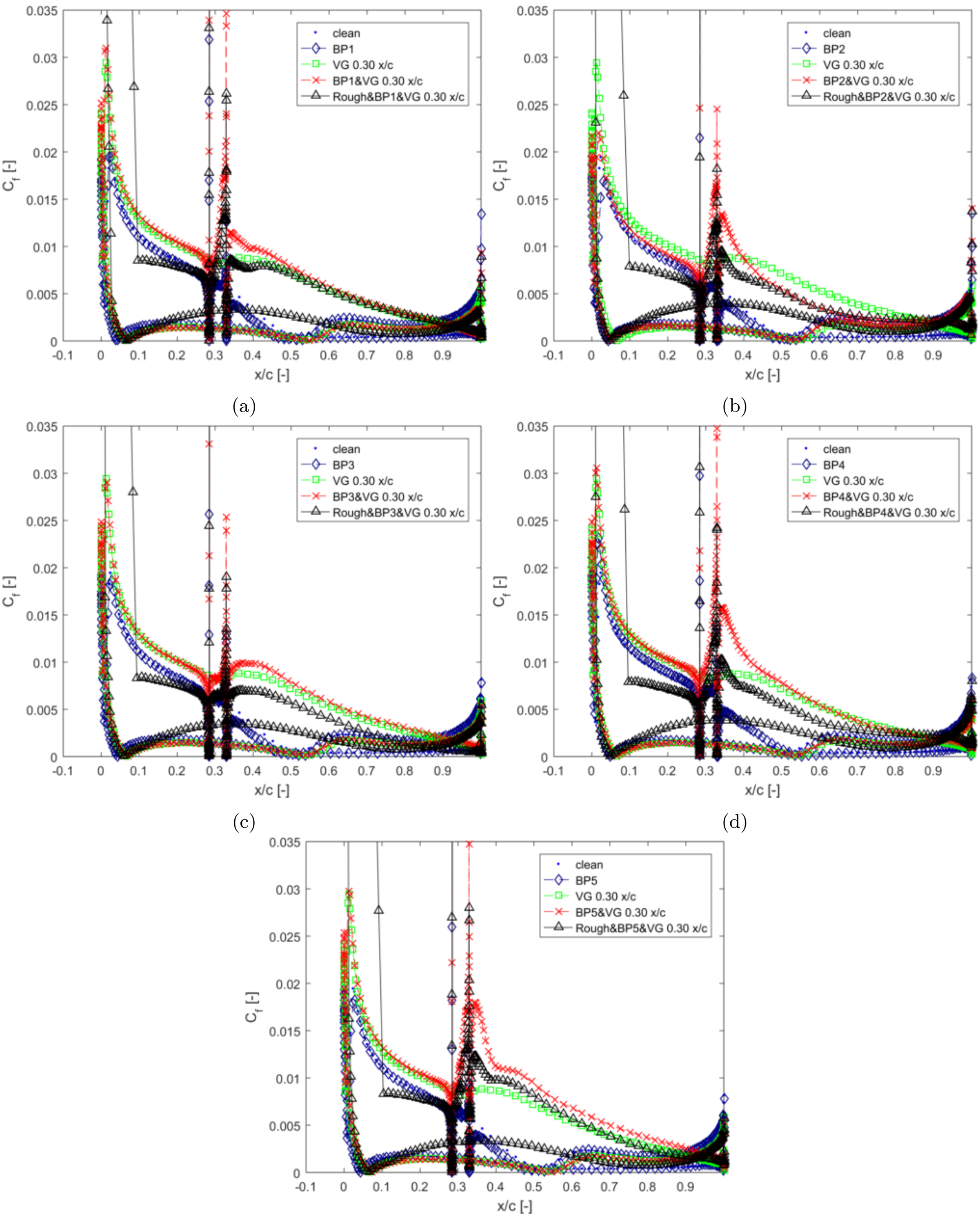

(a) (b)

(c) (d)

(e)

Figure B.20: Friction coefficient curves for the DU 91-W2-250 airfoil at AoA of 15 degrees

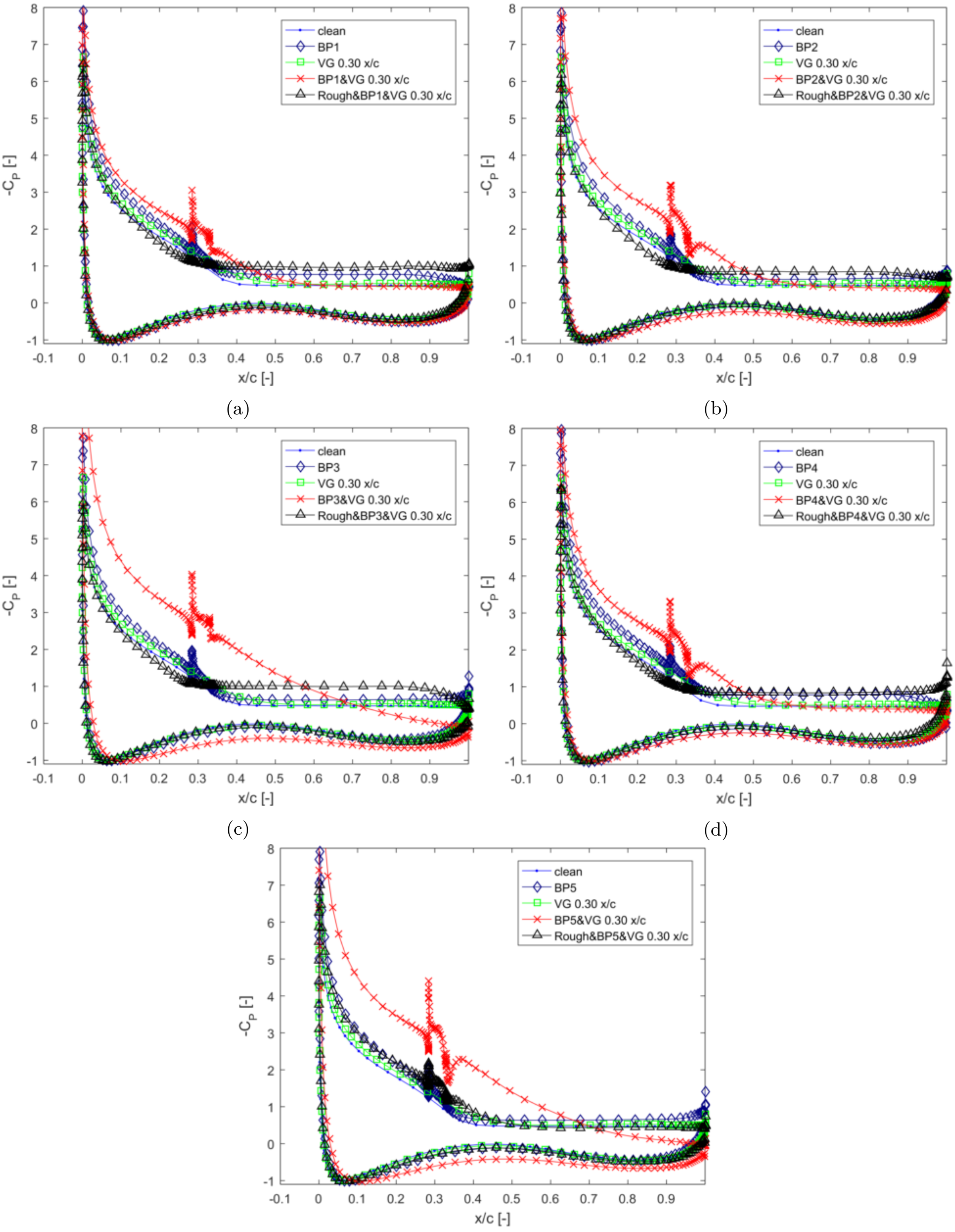

(a) (b) (c) (d) (e)

Figure B.21: Pressure coefficient curves for the DU 91-W2-250 airfoil at AoA of 20 degrees

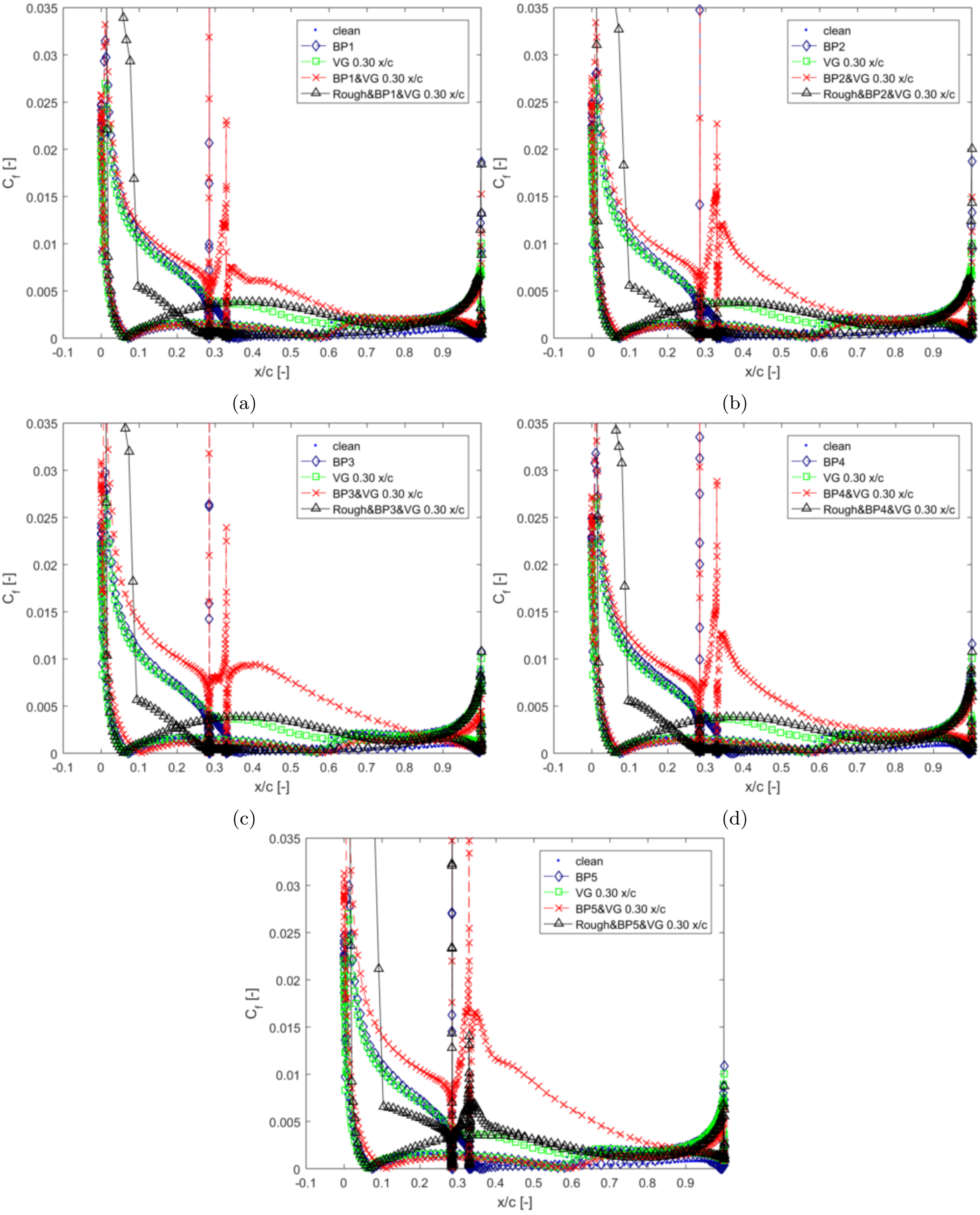

(a)

(b)

(c)

(d)

(e)

Figure B.22: Friction coefficient curves for the DU 91-W2-250 airfoil at AoA of 20 degrees

APPENDIX C Wind Turbine Model

Wind turbine that used in this research for analyzing the effect of roughness to the airfoil section with baseplate, was based on the wind turbine model from 46300 Wind Turbine Technology and Aerodynamics course. The course was delivered at DTU Lyngby in winter semester 2015. Table C.1 gives the description of the wind turbine.

Parameter	*Value*
Rated Power [MW]	2.5
Concept	Pitch regulated variable speed
Rotor diameter [m]	80
No. of blade	3
Cut-in/-out [m/s]	5, 25

Table C.1: Test-case wind turbine

The blade has zero twist and one airfoil is used for the whole blade. Its geometry is detailed in the following table.

$r\backslash R$	0.20	0.30	0.40	0.50	0.60	0.70	0.80	0.90	0.94	0.97
c [m]	3.30	2.51	1.98	1.62	1.37	1.18	1.02	0.83	0.69	0.52

Table C.2: Blade Geometry

The wind distribution over the wind turbine could be determined with weibull parameter (A and k). These parameter were computed using WAsP and data taken from a mast at FINO-2 in the Baltic sea [16]. In this research, scale parameter (A) is 9 and shape parameter (k) is 2.31. The wind probability density function according to this weibull parameter is depicted in following figure:

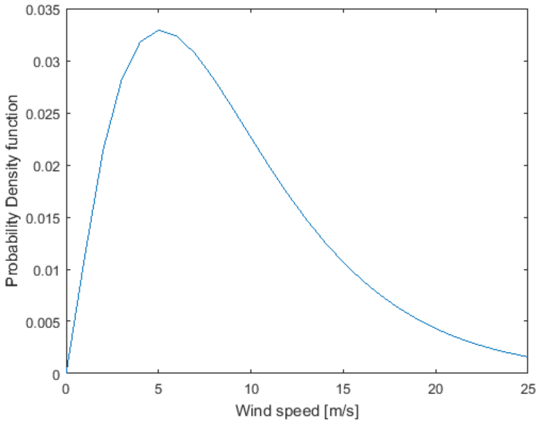

Figure C.1: Probability density function

APPENDIX D

Results Data

AoA [deg]	Without VGs						With VGs					
	Clean	BP1	BP2	BP3	BP4	BP5	Clean	BP1	BP2	BP3	BP4	BP5
0	0.352	0.362	0.339	0.315	0.325	0.337	0.346	0.353	0.329	0.325	0.330	0.331
2	0.615	0.624	0.597	0.573	0.584	0.599	0.605	0.613	-	0.579	0.589	0.589
4	0.869	0.885	0.844	0.808	0.837	0.858	0.845	0.870	0.822	0.829	0.844	0.845
6	1.114	1.138	1.084	1.082	1.085	1.088	1.084	1.120	0.000	1.083	1.096	1.096
8	1.357	1.363	1.319	1.335	1.337	1.328	1.336	1.348	1.240	1.305	1.330	1.329
10	1.582	1.594	1.559	1.559	1.563	1.574	1.583	1.549	1.409	1.492	1.545	1.540
12	1.777	1.833	1.789	1.797	1.810	1.816	1.824	1.700	1.468	1.625	1.720	1.197
14	1.926	2.067	1.991	2.024	2.036	2.053	2.061	1.770	1.409	1.390	1.840	1.804
16	2.000	2.296	2.185	2.239	2.263	2.284	2.292	1.694	1.398	1.472	1.752	1.666
18	1.945	2.516	2.198	2.325	2.483	2.506	2.517	1.500	1.515	1.506	1.631	1.569
20	1.845	2.724	2.039	1.960	2.690	2.717	2.729	1.551	1.777	1.662	1.664	1.962
22	-	1.928	1.835	1.822	1.873	2.124	2.926	1.963	1.974	2.175	1.857	2.192
24	-	1.776	1.943	1.961	1.807	2.254	1.893	2.165	2.060	2.186	2.342	2.136

Table D.1: Lift coefficients of FFA W3-301 airfoil

AoA [deg]	Without VGs						With VGs					
	Clean	BP1	BP2	BP3	BP4	BP5	Clean	BP1	BP2	BP3	BP4	BP5
0	0.010	0.015	0.017	0.014	0.013	0.013	0.011	0.013	0.015	0.012	0.012	0.012
2	0.010	0.015	0.018	0.015	0.014	0.014	0.012	0.013	-	0.013	0.012	0.012
4	0.011	0.016	0.019	0.016	0.014	0.015	0.013	0.014	0.017	0.014	0.012	0.012
6	0.012	0.017	0.021	0.016	0.015	0.016	0.015	0.015	0.000	0.014	0.013	0.013
8	0.013	0.020	0.024	0.018	0.017	0.017	0.016	0.016	0.023	0.016	0.014	0.014
10	0.014	0.022	0.027	0.021	0.019	0.019	0.018	0.019	0.027	0.019	0.016	0.016
12	0.017	0.025	0.030	0.024	0.021	0.022	0.020	0.024	0.039	0.025	0.019	0.014
14	0.021	0.027	0.036	0.027	0.024	0.024	0.022	0.033	0.064	0.061	0.025	0.028
16	0.031	0.031	0.041	0.031	0.028	0.027	0.025	0.060	0.211	0.167	0.049	0.056
18	0.051	0.034	0.082	0.045	0.031	0.030	0.028	0.158	0.224	0.214	0.124	0.123
20	0.084	0.039	0.160	0.094	0.036	0.035	0.032	0.180	0.261	0.193	0.136	0.245
22	-	0.191	0.226	0.162	0.137	0.103	0.036	0.309	0.295	0.350	0.158	0.313
24	-	0.240	0.394	0.176	0.214	0.168	0.191	0.371	0.289	0.268	0.334	0.263

Table D.2: Drag coefficients of FFA W3-301 airfoil

AoA [deg]	Without VGs						With VGs					
	Clean	BP1	BP2	BP3	BP4	BP5	Clean	BP1	BP2	BP3	BP4	BP5
0	0.432	0.424	0.426	0.423	0.418	0.423	0.428	0.443	0.451	0.431	0.449	0.432
4	0.930	-	-	-	-	-	-	-	-	-	-	-
5	-	1.038	1.042	1.038	1.032	1.038	1.052	1.073	1.071	1.059	1.084	1.051
8	1.376	1.386	1.382	1.387	1.380	1.386	-	-	-	-	-	-
10	-	1.498	1.497	1.506	1.502	1.505	1.628	1.673	1.664	1.640	1.678	1.697
12	1.580	1.560	1.560	1.577	1.578	1.569	-	-	1.867	-	-	-
15	-	1.374	1.406	1.385	1.411	1.398	2.150	2.231	1.719	2.176	2.180	2.261
16	1.417	-	-	-	-	-	2.247	-	-	-	-	-
17	-	-	-	-	-	-	2.341	2.442	1.885	2.368	1.875	2.410
20	1.430	1.785	1.828	1.810	-	1.863	1.568	1.954	2.126	1.568	2.131	1.900

Table D.3: Lift coefficients of DU 91-W2-250 airfoil

AoA [deg]	Without VGs						With VGs					
	Clean	BP1	BP2	BP3	BP4	BP5	Clean	BP1	BP2	BP3	BP4	BP5
0	0.007	0.009	0.009	0.009	0.009	0.009	0.009	0.009	0.009	0.011	0.009	0.012
4	0.008	-	-	-	-	-	-	0.014	-	-	-	-
5	-	0.010	0.010	0.010	0.010	0.010	0.011	0.010	0.011	0.012	0.009	0.013
8	0.011	0.012	0.012	0.011	0.011	0.012	-	-	-	-	-	-
10	-	0.019	0.019	0.018	0.018	0.018	0.018	0.015	0.014	0.019	0.013	0.014
12	0.029	0.025	0.029	0.027	0.027	0.028	-	-	018	-	-	-
15	-	0.076	0.072	0.074	0.072	0.072	0.027	0.021	0.069	0.027	0.022	0.019
16	0.081	-	-	-	-	-	0.029	-	-	-	-	-
17	-	-	-	-	-	-	0.031	0.025	0.077	0.031	0.077	0.026
20	0.130	0.141	0.164	0.167	-	0.169	0.143	0.110	0.091	0.149	0.088	0.114

Table D.4: Drag coefficients of DU 91-W2-250 airfoil

Bibliography

[1] H Abbott, Albert E. VonDoenhoff, and Louis S. Stivers. "Report No 824: Summary of Airfoil Data". In: *Natl. Advis. Comm. Aeronaut.* April (1943), page 141.

[2] P Ashill, J Fulker, and K Hackett. "A review of recent developments in flow control". In: *Aeronaut. J.* 109.1095 (2005), pages 205–232. ISSN: 00105317.

[3] Anders Bjorck. "Coordinates and Calculations for the FFA-Wl-xxx, FFA-W2-xxx, FFA-W2-xxx and FFA-W3-xxx Series of Airfoils for Horizontal Axis Wind Turbines". In: *Ffa Tn 1990-15* (1990).

[4] Christopher Booker, Xin Zhang, and Sergei Chernyshenko. "Large-Scale Source Term Modeling of Vortex Generation". In: *27th AIAA Appl. Aerodyn. Conf.* June (2009). ISSN: 10485953. DOI: doi:10.2514/6.2009-3951.

[5] M. B. Bragg and G. M. Gregorek. "EXPERIMENTAL STUDY OF AIRFOIL PERFORMANCE WITH VORTEX GENERATORS". eng. In: *Journal of Aircraft* 24.5 (1987), pages 305–309. ISSN: 15333868, 00218669.

[6] Vincent Brunet et al. "Experimental and Numerical Investigations of Vortex Generators Effects". In: *3rd AIAA Flow Control Conf.* June (2006), pages 1–12. DOI: 10.2514/6.2006-3027. URL: http://arc.aiaa.org/doi/abs/10.2514/6.2006-3027.

[7] DE Culley et al. "Active flow separation control of a stator vane using embedded injection in a multistage compressor experiment". eng. In: *Journal of Turbomachinery-transactions of the Asme* 126.1 (2004), pages 24–34. ISSN: 15288900, 0889504x. DOI: 10.1115/1.1643912.

[8] David C. Wilcox. *Turbulence-Modeling-for-CFD*. 1993.

[9] Mark Drela and Michael B. Giles. "Viscous-inviscid analysis of transonic and low Reynolds number airfoils". In: *AIAA J.* 25.10 (1987), pages 1347–1355. ISSN: 0001-1452. DOI: 10.2514/3.9789.

[10] Erich E.Bender, Bernard H. Anderson, and Patrick J. Yagle. "VORTEX GENERATOR MODELING FOR NAVIER-STOKES CODES". In: 1999. ISBN: FEDSM99-6919.

[11] Bernhard Eisfeld, Tobias Knopp, and Javier Bartolome Calvo. "Application of a new roughness extension for k - ?? turbulence models". In: *Notes Numer. Fluid Mech. Multidiscip. Des.* 112 (2010), pages 43–50. ISSN: 16122909. DOI: 10.1007/978-3-642-14243-7_6.

[12] EWEA. "Wind energy scenarios for 2030". In: *Ewea* July (2015), pages 1–8. URL: http://www.ewea.org/fileadmin/files/library/publications/reports/EWEA-Wind-energy-scenarios-2030.pdf.

[13] EWEA. "Wind in power 2014 European statistics". In: February (2015), pages 1–12.

[14] M Gad-el Hak and Dennis M Bushnell. "Separation Control : Review". In: *J. Fluids Eng.* 113 (1991), pages 5–30. DOI: 10.1115/1.2926497.

[15] M. O. L. Hansen et al. "Aerodynamically shaped vortex generators". In: *Wind Energy* 17.April 2013 (2014), pages 657–669. ISSN: 1099-1824. DOI: 10.1002/we. arXiv: arXiv:1006.4405v1. URL: http://onlinelibrary.wiley.com/doi/10.1002/we.1608/full.

[16] Charlotte B Hasager et al. "SAR-Based Wind Resource Statistics in the Baltic Sea". In: (2011), pages 117–144. DOI: 10.3390/rs3010117.

[17] James H. Henderson and Jack F. Runckel. "An Investigation of the Effects of a Vortex-Generator Configuration on the Aerodynamic Characteristics of a 1/4-Scale Model of the X-1 Airplane (10-Percent-Thick Wing)". und. In: (1952).

[18] P. Iannelli, F.M. Denaro, and P. Lampitella. *Micro Vortex Generators RANS Simulation via Source Term Modelling in a Commercial CFD Solver.* Technical report. Ischia, Italy: European Drag Reduction and Flow Control Meeting, 2006, pages 10–13.

[19] Adam Jirasek. "Vortex-Generator Model and Its Application to Flow Control". In: *J. Aircr.* 42.6 (2005), pages 1486–1491. ISSN: 0021-8669. DOI: `10.2514/1.12220`. URL: `http://arc.aiaa.org/doi/abs/10.2514/1.12220`.

[20] B. P. Leonard. "A stable and accurate convective modelling procedure based on quadratic upstream interpolation". In: *Comput. Methods Appl. Mech. Eng.* 19.1 (1979), pages 59–98. ISSN: 00457825. DOI: `10.1016/0045-7825(79)90034-3`.

[21] M.J. LIGHTHILL. "Introduction. Boundary layer theory in Laminar Boundary Layers". eng. In: (1963).

[22] John C. Lin. *Review of research on low-profile vortex generators to control boundary-layer separation.* Volume 38. 4-5. 2002, pages 389–420. ISBN: 1757864555. DOI: `10.1016/S0376-0421(02)00010-6`.

[23] L. M. M. Mack. "Aerodynamic analysis requiring advanced computers". In: *Paper nr 4. NASA SP-347* (1975).

[24] M Manolesos et al. "Computing the flow past Vortex Generators: Comparison between RANS Simulations and Experiments". In: *J. Phys. Conf. Ser.* 753 (2016), page 022014. ISSN: 1742-6588. DOI: `10.1088/1742-6596/753/2/022014`. URL: `http://stacks.iop.org/1742-6596/753/i=2/a=022014?key=crossref.ee12c1d237ffafdcdd45cfadc5523cf8`.

[25] E.C. Markell. *FLOW SEPARATION IN THREE DIMENSIONS.* Technical report. 1955.

[26] Florian R Menter. "AIAA 93 · 2906 Zonal Two Equation k · co Turbulence Models for Aerodynamic Flows . Mailing Address : 24th Fluid Dynamics Conference FOR AERODYNAMIC FLOWS". In: (1993).

[27] J. A. Michelsen. *Basis3D - a platform for development of multiblock PDE solvers.* Technical report. Lyngby: Technical University of Denmark, 1992.

[28] NASA. *Introduction to the Aerodynamics of Flight.* [Online; accessed May 12, 2017]. URL: `https://history.nasa.gov/SP-367/f35.htm`.

[29] S. V. Patankar and D. B. Spalding. "A calculation procedure for heat, mass and momentum transfer in three-dimensional parabolic flows". In: *Int. J. Heat Mass Transf.* 15.10 (1972), pages 1787–1806. ISSN: 00179310. DOI: `10.1016/0017-9310(72)90054-3`.

[30] W.L. Rhie, C.M and Chow. ""Numerical Study of the Turbulent Flow Past an Airfoil with Trailing Edge Separation."" In: *AIAA J. 21* 11.11 (1983), pages 1525–1532. ISSN: 0001-1452. DOI: `10.2514/3.8284`.

[31] Hermann Schlichting and Klaus Gersten. "Boundary-Layer Theory". In: (1979). ISSN: 09977546. DOI: `10.1007/978-3-662-52919-5`. arXiv: `arXiv:1011.1669v3`. URL: `http://link.springer.com/10.1007/978-3-662-52919-5`.

[32] F. G. Schmitt. "About Boussinesq's turbulent viscosity hypothesis: historical remarks and a direct evaluation of its validity". In: *Comptes Rendus Mecanique* 335 (September 2007), pages 617–627. DOI: `10.1016/j.crme.2007.08.004`.

[33] Smart Blade GmbH. *Vortex Generators for performance improvement.* [Online; accessed June 17, 2017]. URL: `http://smart-blade.com/products-services/vortex-generators.html`.

[34] Niels N Sørensen. "General Purpose Flow Solver Applied to Flow over Hills." In: (1995).

[35] Niels N. Sørensen. *HypGrid2D a 2-D mesh generator.* Volume 1035. March. 1998. ISBN: 8755023681. URL: `130.226.56.153/rispubl/VEA/veapdf/ris-r-1035.pdf`.

[36] Niels N Sørensen et al. "Prediction of the Effect of Vortex Generators on Airfoil Performance". In: *J. Phys. Conf. Ser.* 524.1 (2014), page 012019. ISSN: 1742-6596. DOI: `10.1088/1742-6596/524/1/012019`. URL: `http://iopscience.iop.org/1742-6596/524/1/012019`.

[37] P. R. Spalart and V. Venkatakrishnan. “On the role and challenges of CFD in the aerospace industry”. In: *Aeronaut. J.* 120.1223 (2016), pages 209–232. ISSN: 00019240. DOI: `10.1017/aer.2015.10`.

[38] Kevin Standish and Peter Rimmington. “Computational Prediction of Airfoil Roughness Sensitivity”. In: *48th AIAA Aerosp. Sci. Meet. Incl. New Horizons Forum Aerosp. Expo.* January (2010), pages 1–12.

[39] Timothy L Sullivan. “Effect of Vortex Generators on the Power Conversion Performance and Structural Dynamic Loads of the Mod - 2 Wind Turbine Conservation and Renewable Energy”. In: *NASA Tech. Memo.* (1984).

[40] H.D. Taylor. *Increasing the efficiency of the U.A.C. 8-ft wind tunnel fan by means of vortex generators.* Technical report. Technical Report R-4012-4, 1947.

[41] Hendrik Tennekes and John Leask Lumley. *A first course in turbulence.* 1972.

[42] W. A. Timmer and R. P. J. O. M. van Rooij. “Summary of the Delft University Wind Turbine Dedicated Airfoils”. In: *J. Sol. Energy Eng.* 125.4 (2003), page 488. ISSN: 01996231. DOI: `10.1115/1.1626129`. arXiv: `AIAA-2003-0352`. URL: `http://solarenergyengineering.asmedigitalcollection.asme.org/article.aspx?articleid=1456892`.

[43] N. Troldborg et al. “A consistent method for finite volume discretization of body forces on collocated grids applied to flow through an actuator disk”. In: *Comput. Fluids* 119 (2015), pages 197–203. ISSN: 00457930. DOI: `10.1016/j.compfluid.2015.06.028`. URL: `http://www.sciencedirect.com/science/article/pii/S0045793015002194`.

[44] Niels Troldborg, Frederik Zahle, and Niels N. Sørensen. “Simulation of a MW rotor equipped with vortex generators using CFD and an actuator shape model”. In: *53rd AIAA Aerosp. Sci. Meet.* January (2015), pages 1–10. DOI: `doi:10.2514/6.2015-1035`.

[45] Niels Troldborg, Frederik Zahle, and Niels N. Sørensen. “Simulations of wind turbine rotor with vortex generators”. In: *J. Phys. Conf. Ser.* 753 (2016), page 022057. ISSN: 1742-6588. DOI: `10.1088/1742-6596/753/2/022057`. URL: `http://stacks.iop.org/1742-6596/753/i=2/a=022057?key=crossref.fb992f01b5b41b8a0370598b7d7ccdd7`.

[46] Upwind-Solutions. *Vortex Generators on S88 Turbines.* 2015. URL: `https://upwindsolutions.uberflip.com/h/i/109439534-vortex-generators-on-s88-turbines`.

[47] Henk Kaarle Versteeg and Weeratunge Malalasekera. *An introduction to computational fluid dynamics: the finite volume method.* Pearson Education, 2007.

[48] Fredrik Wallin and Lars-erik Eriksson. “A Tuning-free Body-force Vortex Generator Model”. In: January (2006).

[49] Matt Whitby. “V164-8.0 MW® breaks world record for wind energy production”. In: *MHI Vestas Offshore Wind* (2015). URL: `http://www.mhivestasoffshore.com/wp-content/uploads/2015/03/21-10-2014-Press-release.pdf`.

[50] David C Wilcox. “Reassessment of the scale-determining equation for advanced turbulence models”. In: *AIAA journal* 26.11 (1988), pages 1299–1310.

[51] W Würz et al. *Wind tunnel measurements of the FFA-W3-301 and FFA-W3-360 airfoils with vortx generators and gurney flaps.* Technical report. Technical report, Universität Stuttgart, Institut Für Aerodynamik Und Gasdynamik, IAG, 2013.

[52] RW YEO, PE WOOD, and AN HRYMAK. “A NUMERICAL STUDY OF LAMINAR 90-DEGREE BEND DUCT FLOW WITH DIFFERENT DISCRETIZATION SCHEMES”. eng. In: *Journal of Fluids Engineering-transactions of the Asme* 113.4 (1991), pages 563–568. ISSN: 1528901x, 00982202. DOI: `10.1115/1.2926515`.